CONSTRUCTION OF A SCANNING TUNNELING MICROSCOPE CAPABLE OF PRECISE STUDIES OF ADSORBATES ON SILICON SURFACES

Steven A. Horn
B.Sc. Physics, University of Lethbridge, 2004

A Thesis
Submitted to the School of Graduate Studies
of the University of Lethbridge
in Partial Fulfillment of the
Requirements for the degree

MASTER OF SCIENCE

Department of Physics
University of Lethbridge
LETHBRIDGE, ALBERTA, CANADA

CONSTRUCTION OF AN STM CAPABLE OF PRECISE STUDIES OF ADSORBATES ON SILICON SURFACES

STEVEN HORN

Approved:

	Signature	Date
_____	_____	_____
Supervisor		
_____	_____	_____
Thesis Examination Committee		
_____	_____	_____
Thesis Examination Committee		
_____	_____	_____
External Examiner		
_____	_____	_____
Chair, Thesis Examination Committee		

Dedication

I dedicate this work to my parents. The work ethic they drilled into me starting in elementary school has helped me to become academically successful. I thank them for the tutoring they gave me to start me off and their support as I continue to learn.

Abstract

An STM head based on the design of Besocke was designed and constructed to have superior vibrational and thermal stability in order to produce very high resolution images. The vibrational properties and thermal properties of the head design are quantitatively analyzed and compared to the actual performance achieved. With this new STM head, we were able to implement spectroscopic dI/dV imaging techniques (conductance imaging) to observe electronic features on surfaces. Using this conductance imaging, benzene and chlorobenzene on the Si(111)7x7 surface were studied. We also present the first solid evidence that confirms that the rest atom is involved in the bonding of benzene to this surface. We show that conductance imaging does indeed show variations in the electronic structure of the surface with adsorbates, illustrating that this technique has strong potential for assigning binding sites.

Acknowledgements

I would like to acknowledge the support of the University of Lethbridge for providing funding and work while completing my program. I am eternally grateful for the support of my committee for giving ideas, support, and listening to my progress reports. I thank my supervisor Steve Patitsas for taking me into his lab as an undergraduate and later as a graduate student. I thank him for his instruction, his ideas, support, and interesting discussions. I would also like to acknowledge the people who began this project: Brian Wynder for designing the annealing stage and the wobble stick Jaws, Tom Dyck for his work designing the prototype STM head and load-lock system, and Blair Knight for his work on the Annealing Stage. I thank Frank Klaussen for his excellent work machining many of the parts for the STM head. His work never ceases to amaze me.

I would also like to thank my supervisor for putting me in contact with the group at Lawrence Livermore National Laboratory. The three months I spent there was an incredible learning experience. I'd like to thank Trevor Willey for his exceptional mentoring while I was at Livermore. Also, I thank Trevor for his help in introducing me to so many people in this field at University of California at Davis, University of California at Berkeley, and Stanford University. I'd like to thank Tony VanBuuren and Louis Terminello for finding the funding for my visit to Livermore and their supervision while I was there.

I thank my peers in the lab Weiming Liu and Pouya Maraghechi for interesting discussions and making my experience more fun throughout this program. They would always lend me a hand if I asked and I am grateful for their help.

Table of Contents

List of Tables

List of Figures

List of Abbreviations

ADC	Analog to Digital Converter
CITS	Current Imaging Tunneling Spectroscopy
CTE	Coefficient of Thermal Expansion
DAC	Digital to Analog Converter
DAS	Dimer-Adatom-Stacking (fault)
DAQ	Data Acquisition (board/card/equipment)
DHO	Damped Harmonic Oscillator
DHOSM	Damped Harmonic Oscillator Support Mechanism
DOS	Density of States
FL	Fermi Level
FWHM	Full Width at Half Maximum
HREELS	High Resolution Electron Energy Loss Spectroscopy
HV	High Vacuum
ID	Inside Diameter
LDOS	Local Density of States
LEED	Low Energy Electron Diffraction
LN2	Liquid Nitrogen
NEXAFS	Near-Edge X-Ray Absorption Spectroscopy
OD	Outside Diameter

PID	Proportional-Integral-Derivative
RA	Rest Atom
RCA	Trademark used by Thomson SA, an electronics manufacturer
RHK	RHK Technology, a supplier of Scanning Probe Microscopy equipment
RMS	Root-Mean-Squared
SNR	Signal-to-Noise Ratio
SPM	Scanning Probe Microscopy
STM	Scanning Tunneling Microscope, or, Scanning Tunneling Microscopy
STS	Scanning Tunneling Spectroscopy
TED	Transmission Electron Diffraction
TEM	Transmission Electron Microscopy
TSP	Titanium Sublimation Pump
UHV	Ultra High Vacuum

Chapter 1
Introduction

In 1981, Gerd Binnig and Heinrich Rohrer at the IBM Zurich Research Laboratory obtained, for the first time, real-space images of the wide area atomic structure of a surface. Their results were published in 1982 [1]. Their invention of the Scanning Tunneling electron Microscope (STM) made such images possible. Prior to the invention of the STM, the Field Ion Microscope (FIM), was the only experiment capable of imaging atoms in real space [2]. The FIM was limited to imaging the atoms located on the tip of a sharp conductor. The STM added the capability of imaging atoms on a flat surface and wider area. The mechanical simplicity of the microscope is a true virtue of the design of this instrument. In 1986, the pair shared the Nobel Prize in Physics for their remarkable invention. Physicists could now study the nature of matter at a scale never before observed in real space, and chemists could observe individual molecular structures and interactions.

1.1 The Principles of STM

Scanning Tunneling Microscopy is possible only because of quantum mechanics. One of the important results of quantum mechanics is the phenomenon of tunneling [3]. In the macroscopic world, it would be strange if an object adjacent to a solid barrier would, all of a sudden, appear on the other side. However, at very small scales, this is completely possible. In all solid matter around us, electrons are found bound to a lattice of atoms. When they are bound, they are confined to move in an electronic orbital. If a sharp metal tip is placed within a few ångströms (10^{-10} m) of a conductive surface with a vacuum gap in-between, it can be modeled that the electron orbitals (as described by quantum mechanics) on the tip can overlap with those of the surface. In this case, electrons from one orbital can transfer to an orbital across the small gap. Classically, this gap is impenetrable to these

electrons, but quantum mechanically, they have crossed it. If an electric potential is applied between the two objects, electrons will "tunnel" across the vacuum barrier from one electronic orbital to another. Depending on the direction of the bias, electrons can tunnel from the valence states in the surface (occupied states) to the tip, or from the tip to the conduction states in the surface (unoccupied states) yielding a small current.

Measuring this small current is the experimental verification that tunneling is occurring. There is a distinct difference in the current from electron tunneling and the current if there was physical contact. The electrical resistance across the vacuum gap is in the gigaOhms range ($G\Omega$). The resistance from a physical conductive contact would be much smaller smaller (tens of kiloOhms or smaller), and yield a large current. When tunneling, the magnitude of this small current is dependant on the gap between the tip and the surface. As the tip approaches closer, the barrier becomes smaller and so the current will increase. Monitoring this current can be used as an indication of the proximity of the tip to the surface. By some means, the tip can be moved closer and further from the surface. To keep the barrier (space between tip and sample) constant, this current should be kept constant. As such, the tip is moved in or out to keep the tunneling current a constant level. This is referred to as the current feedback loop, and the small space it maintains is called the tunneling junction.

Using the current feedback loop as a mechanism to maintain a constant current (gap), the tip is then raster scanned along the surface in a fashion similar to how a television generates a picture. Monitoring the feedback signal that moves the tip closer or further from the sample produces an image showing a topographic map of the surface. Because the feedback signal depends on the measurement of the tunneling current and not the actual physical geometry of the surface, this image contains a richness of geometric and electronic information about the surface. The first surface that was imaged in such a way by Binnig and Rohrer was the silicon (111) 7x7 surface.

1.2 The Silicon(111) 7x7 Surface

Before continuing, there needs to be some understanding of the surface that is being observed with the STM head. The silicon surface has been a topic of thorough investigation by many techniques. This was the first surface observed at atomic resolution using STM[4]. The complexity of the 7x7 reconstruction is a representative display of the mysterious and interesting nature of the nanometer scale. The 7x7 reconstruction was observed before STM using techniques such as Low Energy Electron Diffraction (LEED)[5]. Unfortunately, LEED is not sensitive enough to provide a model of the 7x7 surface. It wasn't until STM studies [1] at atomic resolution that physicists were first able to begin modeling this surface correctly. Although STM gave unsurpassed information about this surface, it wasn't until high resolution TEM and TED that the best model for the surface was developed by Takayanagi et. al. [6, 7]. The dimer adatom stacking fault (DAS) model was developed and is currently the accepted model of the Si(111) 7x7 surface.

1.2.1 The DAS model of 7x7

Bulk silicon has the diamond structure in which the atoms are sp^3 hybridized. When the crystal is cleaved in vacuum, it leaves valence p-like orbitals pointing outward. The surface structure is defined in terms of two dimensional lattices. In much the same way that a unit cell can be defined for a three dimensional lattice, for the two dimensional lattice of a crystal, one defines a similar unit cell. The unit cell is the smallest surface that can be repeated over the entirety of the lattice.

When a crystal is cleaved, the free valance orbitals pointing outward can be described as a 1x1 lattice, that is, each orbital is its own unit cell. The size of the unit cell is 3.8 Å along the side. Following the initial cleaving, the surface will form bonds between the valance orbitals, thus reducing the total surface energy. The reconstruction that happens initially is a 2x1 reconstruction [8] as ambient thermal energy is enough for the surface to reconstruct into the 2x1 pattern. 2x1 implies that

the unit cell has the same area as two 1x1 unit cells had previously. This initial reconstruction is not the lowest energy state of this surface and there are two dangling bonds per 2x1 unit cell. The 2x1 reconstruction is metastable, meaning that it is not the lowest energy configuration of the surface. There exists an energy barrier between the 2x1 and other reconstructions. As the surface gains energy by heating, the atoms gain enough energy to re-arrange into more stable configurations.

Using thermal annealing, atoms on the surface can gain enough energy to re-arrange the bonding structure and relieve the net stress on the bonds. Once the surface is heated above the threshold energy, the surface can reconstruct into the 7x7 structure. This threshold is reached at 860 ˚C. The 7x7 reconstruction is the lowest energy reconstruction of the silicon surface. Since the 7x7 reconstruction is the lowest energy, it is the most commonly studied reconstruction due to the fact that it is less difficult to generate than other metastable reconstructions. This structure has sides that are 26.8 Å and tilted 60° to form a rhombus. The 7x7 structure of silicon has 19 dangling bonds per unit cell, a much lower density than the 2x1 reconstruction. Cleaving a crystal creates a great amount of stress on the surface bonds and the method of reconstruction after thermal annealing is complex and not obvious. These reconstructions are of great interest in surface science.

In Figure 1-1, the red (A) atoms are called the adatoms, which have dangling bonds, and the green (R) atoms are called the rest atoms, which also have dangling bonds. There are 12 adatoms and 6 rest atoms per unit cell. The circle structure in the corner of the unit cell is a hole with one dangling bond in the center (H). This atom is the corner hole atom and the 19^{th} dangling bond in the unit cell. The two triangular halves of the unit cell also appear different. This is due to a stacking fault on the third layer of atoms. The stacking fault in Figure 1-1 is on the left most side. Although there is a stacking fault, the two halves of the unit cell appear identical looking only at the dangling bonds. In occupied states STM imaging, however, it is observed that the two halves of the unit cell apparently

have a different electronic structure from this stacking fault. Images and a discussion on the stacking fault will be given in section 6.2.

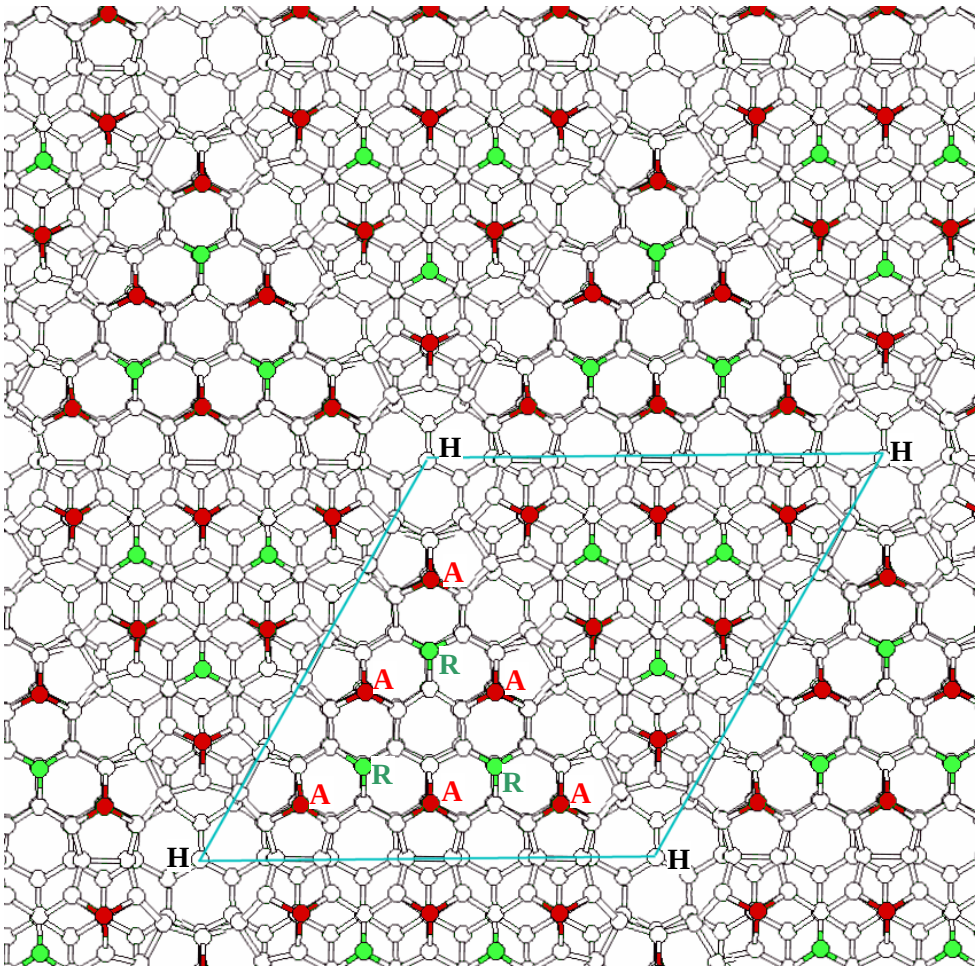

Figure 1-1 Top view render of Si(111)7x7 DAS structure, A indicates adatoms, R indicates rest atoms, and H indicates corner holes

1.3 Achievements of STM

1.3.1 Manipulation

In addition to its imaging capability, the STM is also capable of atomic manipulation. The most basic type of manipulation the STM can do is physically scratching a surface. The level of control of the STM tip is very high. It is possible to bring the STM tip close enough to a surface to touch; and then scratching can be used to create basic surface deformations that are very large (~ 200 Å across) [9]. Of course, this type of manipulation is destructive to the tip.

Another basic form of manipulation is using the STM to generate large electric fields to cause bond breaking and the restructuring of surfaces at the atomic scale. This field-induced type of manipulation is not very accurate, but clusters of atoms can be moved around [10]. This non-contact technique is less destructive to the tip.

More detailed manipulation can be achieved using the STM. Using soft lateral manipulation of adsorbed species at low temperature, individual atoms or molecules can be positioned on a surface within an accuracy of a few ångströms. One example of this is the arrangement of xenon atoms on a cold Cu(211) surface [11, 12]. Using this manipulation capability, there are many possible applications. One application is the possible use of atoms, or small clusters of atoms to record information, bit by bit, at the nano-scale [13].

1.3.2 Controlled Desorption

In addition to the capability of STM to manipulate species on a surface, it is also capable of removing atoms and molecules from a surface. This controlled desorption is done by STM induced bond breaking; causing the molecule to desorb from the surface. This capability is useful for the study of the binding energy of molecules to surfaces and is one tool that provides information about the binding structure of molecules to surfaces.

Molecular desorption has been successfully achieved for many systems. A few examples are: benzene on Si(100) [14, 15], benzene on Si(111) 7x7 [16], chlorobenzene on Si(111) 7x7 [17], and decaborane ($B_{10}H_{14}$) daughters on Si(111) 7x7 [18].

1.3.3 Nano-electronics: Molecular switches and nano-wires

The capability and technology to fabricate nanoscale and molecular scale electronic devices is one goal that STM is assisting with. If such devices could be created, specifically transistors, a new generation of computing would be born. There has been progress in the creation of conductive nano-wires that might one day become the wires that connect components together [19].

Additionally, the creation of molecular switches is becoming a reality. One example of a molecular switch is a low temperature system involving a toluene ($C_6H_5CH_3$) molecule on a cold SI(111) 7x7 surface [20]. Wolkow has also reported success in regulating the motion of an electron through an individual molecule on a silicon surface [21].

1.3.4 Vibrational Spectroscopy and Single Molecule Chemistry

The use of STM to study the electronic nature of the surface is an obvious spin-off of the imaging capability [22-24]. Another capability is to use STM to measure the vibration of the bonds of individual molecules. At low temperatures (liquid helium), bonds can be excited to vibrate by inelastic electron scattering. The subsequent vibrations can be detected by monitoring the STM signal from these molecules [25-27]. The information gained from these vibrational spectra can be used as a tool to make precise characterizations of molecular bonds. This information proves useful for the study of chemistry at this small scale. However, vibrational spectroscopy is a difficult experiment limiting its practical use.

In addition to spectroscopy, STM imaging and manipulation is capable of observing chemistry at a new scale. STM has been used to observe the chemistry of interacting molecules [28].

The distances involved in chemical reactions on surfaces can be observed in a time-lapse type experiment. This experimental data and verification provides chemists with a direct observation of the spatial scale of chemical reactions.

1.4 STM and Adsorbate Bond Characterization

STM images include more than just the geometric surface information. The ability to probe the electronic structure is of great use for studies of chemical physics. The study of binding structures of molecules to the silicon surface is one example of an application of STM. The binding of benzene (and its related molecules, such as chlorobenzene) was studied using STM. Benzene was first studied on the silicon surface by Wolkow [29] and showed a unique feature in which the benzenes on the Si(111) 7x7 surface were moving around. It was determined that the binding energy of benzene was low enough to facilitate thermal desorption, allowing benzenes to break bonds easily.

The use of STM in combination with other characterization tools is a very useful in determining the nature of the binding. By observing binding sites on the surface with STM and probing bond angles with X-Ray techniques [30, 31], it has been proposed that the benzene double bond is involved in the binding [30]. The true nature of this bond is still not completely established and has been a topic of continued study. Using a combination of geometry and electronic spectroscopy images, the benzene-Si(111) structure was probed for clues about how it's binding. Benzene adsorption observed at occupied states shows many similarities to the binding of chlorobenzene seen by another group [17, 32, 33].

Another spectroscopic technique, spectroscopic dI/dV conductance, has been outlined by Becker et. al [34] and a similar technique developed by Hamers [23]. Using this technique in conjunction with topographic imaging can yield more information about the binding of adsorbates. This spectroscopic dI/dV conductance imaging was able to single out the electronic contribution of

the rest atom dangling bonds on the Si(111) 7x7 surface. It is believed that these bonds play an important role in the binding of singular aromatic molecules, such as benzene, to this surface [35-39].

Chapter 2
General Design of the STM Head

The STM head is an apparatus that can first accept the transfer of a sample and tip and then facilitate the mechanical motion required to bring the sharp end of the tip to within one nanometer of the surface of the sample. Furthermore, electrical connections must be made to external electronics in order to produce a stable tunnel junction. This chapter includes a discussion of the key design considerations that must be dealt with in order to produce high quality STM data.

2.1 Key Design Considerations

Of the important considerations that must be made towards an STM design, here the following will be discussed: i) sample and tip transfer ii) vibration isolation and iii) thermal properties. Note that one important system, the electrical system, will not be discussed in detail in this work. This involves the measurement of the tunnel current, the feedback system used to stabilize the tunnel junction, and the image scanning system. A detailed description of this system can be found in reference [40].

2.1.1 Sample and Tip Transfer

Clean silicon samples of dimension 1 cm x 1 mm x 0.4 mm are mounted on a sample holder made of various materials capable of withstanding temperatures up to 1300 C with minimal outgassing. These materials include copper, molybdenum, tantalum electrical conductors as well as ceramic insulators. A wobble stick with homemade adjustable jaws is used to move the sample holder inside the vacuum chamber. Mechanical considerations must be made in the STM design to ease the transfer of the holder into and out of the STM head. Similar

considerations must be made for the physically smaller tip holder. Given the imprecise motion of both of these components during transfer a safety margin of about 1 mm of distance between sample and tip must be incorporated into the design i.e. after a new sample and tip have been installed they typically lie a distance of 0.5 to 1.0 mm away from each other.

The STM head must include what is commonly referred to as a "coarse approach mechanism" in order to bring the tip within tunneling range of the sample. This mechanism must be capable of making discrete and repeatable steps of no more than 1 micrometer of motion between sample and tip. The maximum amount of mechanical motion available from the type of piezoelectric actuators used in STM systems is about one micrometer and the tunneling current needs to be monitored between the coarse approach steps. The coarse approach system needs to be reliable while being capable of back and forth motion. The system used in the University of Lethbridge STM is discussed in section 2.2. The choice for this design was made because of its compatibility with the other key design considerations i.e. having good mechanical properties as far as vibrations go and having good thermal properties.

2.1.2 Vibration Isolation

STM is highly sensitive to motion. Even the quietest rooms and surfaces have vibration levels on the order of hundreds of nanometers, that appear enormous on the picometer scale observed with a scanning tunneling microscope. According to empirical knowledge, the floors of almost all buildings vibrate at amplitudes given by $\alpha f^{-2} m/\sqrt{Hz}$ where the parameter α ranges between one part in a million for rather noisy buildings to as low as one part in a billion for very quiet structures. [41]. If there is too much vibration, the carefully prepared sample and atomically sharp tip will simply oscillate into each other and both the sample and tip will be damaged. Fortunately, the amount of vibrations experienced at the tunnel junction can be

greatly reduced. Though it may be easy to turn off a nearby air conditioner, or to walk about quietly during experiments, some noise sources can not be easily shut off. Noises caused by the wind blowing against the building, nearby vehicles, elevators, air-handling equipment, etc. will present problems. While it is helpful to minimize the vibrations by finding a quiet room, the remaining vibrations need to be dealt with carefully in STM designs. Isolation schemes that have been applied both outside and inside the vacuum chamber are discussed in detail in Chapter 3. For now it is enough to realize that the STM head must be compact and rigid. This will help prevent the ambient vibration noise that does get transmitted to the head from actually affecting the tip to sample separation.

2.1.3 Thermal Gradients

When one part of the microscope has a different temperature than another part, there is a thermal gradient across the microscope. Any time variation of this gradient could result in what is commonly referred to as thermal drift. Thermal drift creates difficulties for STM imaging; specifically, some of the problems caused by thermal drift are image stretching, tunneling feedback range threshold problems (saturation of the Analog to Digital Converter), and loss of the desired ability to track specific surface features for long periods of time. Image stretching can be corrected by software, feedback issues can be avoided with continual monitoring, but certain basic surface science studies, such as diffusion studies, STM manipulations, etc., demand the ability to track certain features image after image.

There are ways to limit the problem of thermal drift. One way is to cool the entire system to very low temperatures since it well known that the coefficient of thermal expansion approaches zero at very low temperatures. For studies at room temperature, this is not a feasible solution. For a more general technique to limit thermal drift, design of the STM head must be considered.

Though detailed considerations are discussed in Chapter 4, several useful rules of thumb are mentioned here: i) make the STM head compact in size, ii) eliminate internal sources of heat, iii) use materials with low thermal expansion coefficients and/or high thermal conductivities, iv) design components with large cross-sectional areas and v) avoid thermal bottlenecks whenever possible.

2.2 The Besocke-Type STM Head

The STM head of choice was based on the design by Besocke [26, 42]. The design of this head, as illustrated in Figure 2-1, is simple and it has many features that make it advantageous over other designs (i.e. compact, thermally compensated, and controlled coarse approach). The compact design of this head reduces the influence of vibration. Additionally, this type of head is intrinsically thermally compensated because the supports of the sample and tip are the same length and material, which reduces the effects of thermal drift. The three sample supports are tubes composed of piezoelectric ceramic. A fourth, centrally positioned, piezoelectric tube is used to support the tip and is responsible for the tunnel junction control and lateral scanning conducted during STM imaging experiments. The symmetric placement of the tip support helps to limit lateral thermal drift effects. The outer three piezoelectric tubes are used exclusively for coarse approach motion.

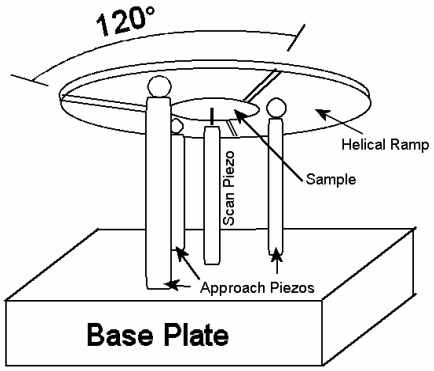

Figure 2-1 Diagram of the Besocke Type STM Head

Before a tunnel junction can be established for imaging, the tip has to be brought close enough to the surface for the feedback to function. As mentioned above, this procedure is generally referred to as the coarse approach and there are many ways that this can be accomplished. There are mechanical systems that use gears, and there are dynamic electromechanical systems using oscillating piezo elements to move the tip and sample together. For the Besocke-style system, a variation of which is used at the University of Lethbridge, piezoelectric tubes oscillate with a specific waveform in which a ring with low angle planes rotates causing a screw-like motion (see Figure 2-1). This screw-like motion results in the tip and sample coming close together, until the sample is in reach of the tip. Vertical positioning with a precision of a few tens of nanometers can be achieved.

Once the tip and sample are in the STM, the coarse approach mechanism brings the sample down to approach the tip. This requires the synchronized motion of the outer three coarse approach piezoelectric tubes. The coarse approach mechanism works on a principle of slip-stick, similar to (though with more control) what happens when a grad student turns the stereo up too loud and causes items to vibrate off the table. An asymmetric waveform is sent to each of the

piezoelectric tubes causing them to vibrate, facilitating this motion. A quick jerk-type motion causes the three coarse approach piezoelectric tubes to bend. The directions of these bending motions are all along the circumference of a circle. During this quick bending the balls affixed to the piezos all slide relative to the coarse approach ring. Ideally the ring does not move at all during this step. The slipping action and subsequent slow return (with stick) results in a net rotation of the coarse approach ring by a small amount.

One of the limitations of the Besocke design is that the ceramic piezo-tubes can lead to a thermal bottle-neck in the system i.e. thermal gradients can develop in the piezo tubes and temporal variations in these gradients can lead to thermal drift. The contact area between the balls attached to the piezotubes and the coarse approach ring can also causing thermal bottlenecking. Also, in comparison to the other components that make up the mechanical path between sample and tip, the piezoelectric tubes can very easily wind up being less rigid i.e. more vibrations may be transmitted to the tip to sample separation than would be with a system not using so many piezoelectric tubes.

In order to optimize the design of the coarse approach mechanism the physics of the piezoelectric tubes must be properly understood.

2.3 Analysis of Piezoelectric Tube Deformation

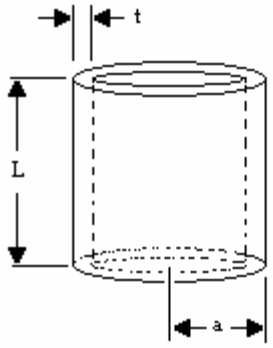

Figure 2-2 Scanner Tube Geometry

Not long after the first demonstration of STM, a tube scanner (see Figure 2-2) was introduced into STM design by Binnig and Smith in 1986 [43]. This scanner provided superior simplicity to the previously used tri-pod type scanners and provided other advantages as well, such as the capability for a more compact STM design.

Four copper electrodes are affixed across the tube as shown in Figure 2-3. When a voltage is placed between the inside electrode and one of the four quadrant electrodes, the material between those electrodes either extends or contracts depending on the polarity of the applied voltage. The shape of the tube changes in a continuous way and the magnitude of the applied voltage determines how much the piezoelectric tube stretches or bends. The direction of the stretch or bend is indicated in Table 2-1.

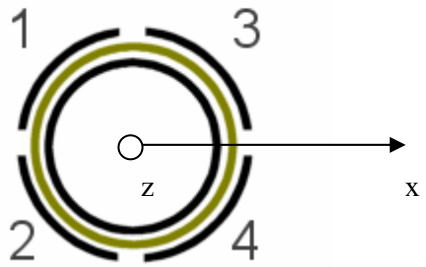

Figure 2-3 Top view of a piezoelectric tube. The inside circle is a solid copper coating serving as a common electrode and the outside (numbered) quadrants are sectioned copper electrodes.

Table 2-1 Response of piezoelectric tubes to various electrode inputs

Electrode 1	Electrode 2	Electrode 3	Electrode 4	Effect (see Figure 2-3)
+	+	+	+	Tube Lengthens
-	-	-	-	Tube Contracts
+	+	-	-	Tube Bends Right
-	-	+	+	Tube Bends Left
+	-	+	-	Tube Bends Down
-	+	-	+	Tube Bends Up

It is noted that bending of the scan tube is used to move the tip laterally across the surface i.e. to generate STM images. To understand the properties of the piezoelectric tubes for use in the coarse approach mechanism, the displacements and forces involved in the operation of a piezoelectric scan tube with electrodes positioned across the thickness of the tube must be calculated..

2.3.1 Piezoelectric Tube Motion

For a piezoelectric tube with a geometry as shown in Figure 2-2, the vertical displacement along the z axis is given in as [44]:

$$\Delta z = \frac{d_{31} \cdot L \cdot V}{t}, \qquad (2\text{-}1)$$

where V is the voltage across the electrodes (perpendicular to the tube length) and d_{31} is the piezoelectric constant for electrodes across the tube wall along the x-axis. If the voltage is opposite across facing terminals such as the third case in Table 2-2, then there is a deflection of the tube in the x direction, as illustrated in Figure 2-4.

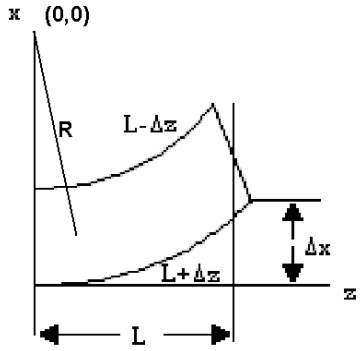

Figure 2-4 Piezoelectric tube bending along the x direction.

The motion in the x direction can be approximated assuming that the deflection, Δx, is small compared to the tube length, L, i.e. $\Delta x << L$. For a first order of approximation, a radius of curvature, R, can be used to approximate the bending of the tube as an arc on a circle. For large displacements, the tube will bend in a more complicated manner than this, but this simple and reasonable approximation can be made for small displacements. Doing so, the equation for a circle must be satisfied:

$$R^2 = z^2 + (x - R)^2. \qquad (2\text{-}2)$$

Setting $z = L$ and $x = \Delta x$ (see Figure 2-4), equation (2-2) can further be simplified to:

$$L^2 = 2R\Delta x . \qquad (2\text{-}3)$$

The bending of the tube results from extension of one side by Δz and the contraction of the other side by an equal amount. Using simple geometry, the following relation is found:

$$R = \frac{aL}{\Delta z}. \qquad (2\text{-}4)$$

where *a* is the inner radius of the tube, and substituting into (2-3) results with a displacement of

$$\Delta x = \frac{L\Delta z}{2a} \qquad (2\text{-}5)$$

and with (2-1),

$$\Delta x = \frac{d_{31}L^2V}{2at} \qquad (2\text{-}6)$$

which is the lateral displacement of the piezoelectric tube for a voltage *V*.

A more careful calculation of the displacement, taking into account the torques produced throughout the tube and integrating over the geometry of the tube, is given [45, 46] as

$$\Delta x = \frac{2\sqrt{2}d_{31}L^2V}{\pi\, a\, t}. \qquad (2\text{-}7)$$

The difference between (2-6) and (2-7) is the constant before the variables, where the careful calculation gives ~0.9, 0.5 was achieved with the radius of curvature approximation.

2.3.2 Forces Generated by the Piezoelectric Tube

The Besocke type STM uses piezoelectric forces for its approach mechanism. To design the STM, the force from a piezoelectric tube must be calculated. If there is insufficient force generated, then the sample positioning can not operate. If excess force is generated, then there may be problems with vibrational excitations. Knowing the amount of force possible will allow

the ramp incline to be set so that it is not too steep or too shallow. There are many adjustable parameters and several constraints.

As with all materials, the physical properties of the piezoelectric with specific parameters (i.e. Young's modulus, density, etc.) can be characterized. The Young's modulus is defined by the stress-strain relationship in the *z* direction (along the length of the tube):

$$\frac{F_z}{S} = Y\frac{\Delta z}{L}. \qquad (2\text{-}8)$$

S is the cross sectional area and *Y* is the Young's modulus of the material. Substituting in (2-1), an expression for the force generated by the piezoelectric element along the *z* direction is

$$F_z = \frac{SYd_{31}V}{t} \text{ (N)}. \qquad (2\text{-}9)$$

It should be noted here that equation (2-9) does not depend on the length of the tube. This means that a short tube will still be able to generate the same force as a longer one, thus reducing the size of the component. However, the maximum length of expansion (Δx) still depends on the length of the tube (*L*), a limiting factor to the extent to which the component can be shrunk.

For the coarse approach system, the forces in the lateral directions are of great importance. An explanation of how the piezoelectric tube generates these lateral forces (perpendicular to the length of the tube) is needed. The treatment given here closely follows that of the analysis of a bending rod given in Kinsler et al. [47]. Before considering the general analysis, a simple laminated bending element composed of two thin laminae is considered in Figure 2-5. In order to bend the element in the x-direction one could apply a force F_x at $z = L$, or equivalently by applying a compressive force F_1 and an expansive force F_2 on each laminate

as shown. This approach allows one to express the product of F_x and L in terms of the net moment applied to the end of the tube.

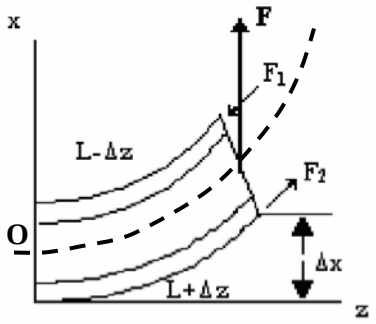

Figure 2-5 Bending forces of a piezoelectric tube

To analyze this in general, one starts by looking at a differential of this force after focusing on a thin laminate with cross-sectional area *dS*. Using the stress-strain relationship gives:

$$df = YdS\frac{\delta z}{L}. \qquad (2\text{-}10)$$

Geometrical consideration results in the following expression:

$$\frac{\delta z}{L} = \frac{r}{R}. \qquad (2\text{-}11)$$

Here, the variable, *r* is measured from the given laminate to the neutral axis and again *R* is the radius of curvature. Substituting (2-11) into (2-10) gives us the following:

$$df = YdS\frac{r}{R}. \qquad (2\text{-}12)$$

From this, the moment (about O) of the tube is calculated by summing all the forces at the end of the tube:

$$M = \int r \cdot df = \frac{Y}{R}\int r^2 dS \,. \qquad (2\text{-}13)$$

It is helpful to use the radius of gyration κ:

$$\kappa^2 = \frac{\int r^2 dS}{S} \qquad (2\text{-}14)$$

For a thin-walled tube with circular cross-section $\kappa = a/\sqrt{2}$. Along with equation (2-4) the moment can be written as:

$$M = Y\left(\frac{\Delta z}{aL}\right)\pi a^3 t \qquad (2\text{-}15)$$

Also, note that the moment can be written equivalently as

$$M = F_x \cdot L \,. \qquad (2\text{-}16)$$

Substituting into (2-13) and making use of equation (2-1) gives the following equation:

$$F_x = \frac{\pi Y d_{31} a^2}{L} V \,. \qquad (2\text{-}17)$$

This is the expression for the lateral force generated by the tube.

2.4 Coarse Approach Mechanism

As explained above, the coarse approach mechanism works on the basis of a repetitive slip-stick cycle. There are many factors that influence this operation. One is the friction force between the surface of the balls and the bottom surface of the coarse approach ring. In order to produce a slipping motion the lateral force, F_x, given in equation (2-17) must overcome this static friction force. If *m* represents one third of the mass of the coarse approach ring then a simple and approximate inequality can be written for the case of slipping:

$$F_x > \mu_s mg \qquad (2\text{-}18)$$

Approximations have to do with the sliding surfaces not being exactly horizontal and that the coarse approach motion is rotational, not linear.

There are three main variables in the electrical waveform applied to the piezoelectric tubes that determine the performance of the slip-stick mechanism: the waveform amplitude, V_0, period, T, and shape. The waveform shape used to achieve the motion is a repetitive half-parabolic type waveform. The sudden rise in voltage (rise time ~ 0.025 ms) is followed by a parabolic return. The waveform, shown in Figure 2-6, is generated digitally by a digital to analog converter (DAC), then amplified and sent to the piezoelectric tubes. The maximum output of the controller, without any saturation effects, and with a period in the range of 1 to 10 ms, is 66 V.

After the ~ 0.05 ms of time spent during the slip part of the cycle, the lateral motion of the piezo-tubes temporarily stops and the two surfaces re-stick. For the purposes of saving time it would be convenient to make the period, T, of the waveform small. Though this would decrease the amount of time required to make a given coarse approach of the tip to the sample, if the period T is too small then the acceleration during the return part of the cycle may be too great, causing undesired slippage.

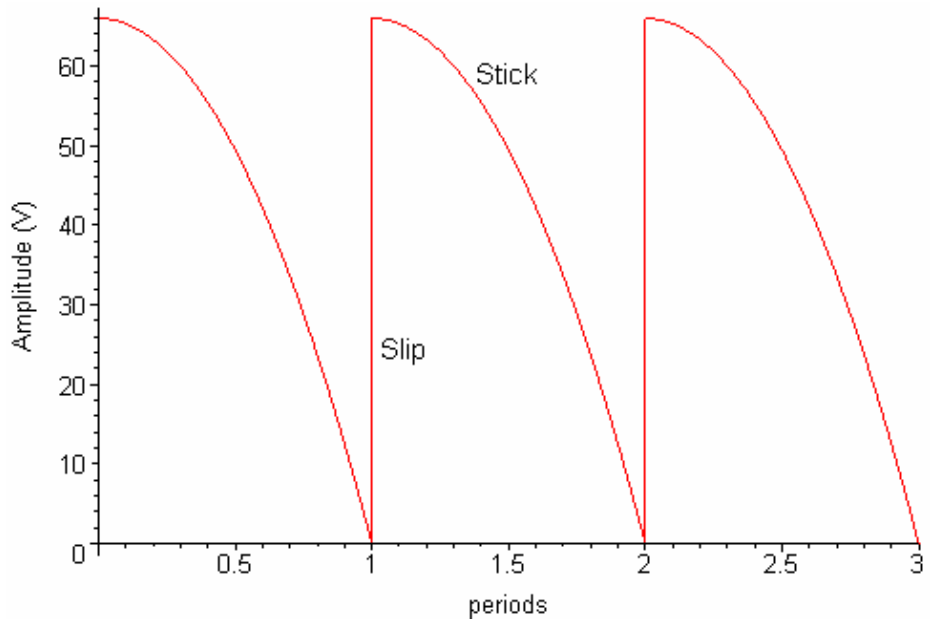

Figure 2-6 Cyclical coarse approach waveform applied to the piezoelectric tubes

Given the parabolic shape of the waveform, and the linear form of the relationship (2-7) between Δx and V, the lateral acceleration is constant in time during the stick portion of the cycle. Simple kinematic analysis, using equation (2-7) leads to an expression for the acceleration of the end of the piezo-tube during the stick portion of the cycle:

$$a_s = \frac{4\sqrt{2}d_{31}L^2V_0}{\pi atT^2} \qquad (2\text{-}19)$$

In order to avoid unwanted slippage the following inequality must hold:

$$a_s < \mu_s g\ . \qquad (2\text{-}20)$$

2.4.1 Prototype STM Head: Lessons Learned

Before the initiation of this M.Sc. project a prototype STM head had been constructed, also based on the Besocke design. Using the prototype STM system, which has piezoelectric

tubes that are 12 mm long with 1.5 mm inner diameter and wall thickness of 0.75 mm, measurements of the coarse approach travel time over a distance of roughly 3 mm were made. The parabolic waveform with amplitude $V_0 = 44$ V was used. The travel time as a function of the waveform period, T, is plotted in Figure 2-7 for the two types of rotational motion, upwards and downwards.

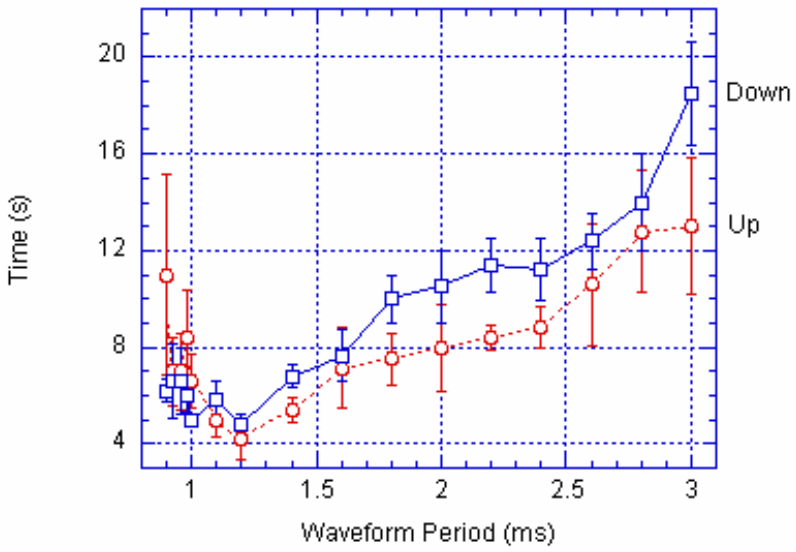

Figure 2-7 Coarse approach travel times over ~3 mm as a function of the waveform period T. Data is shown for the prototype STM head

The two curves, up and down, lie fairly close together, an indication that the direction of sticking and slipping are not too important inn this system. Clearly though the coarse approach conditions are not ideal. Evidently it is more difficult to make a slippage action while traveling uphill as there is a more difficult "angle of attack". This effect has been observed qualitatively to become more aggravated with larger angles of incline on the coarse approach plates. An earlier

prototype version with a 4 degree incline angle was observed to stall frequently in the upwards direction. The angle on this prototype was ~2.0 degrees.

Between 1.2 ms and 3.0 ms periods the two curves vary roughly linearly with T as expected from ideal stick-slip operation. As the period is decreased below 1.2 ms, it takes longer and longer to travel, presumably due to slippage during the stick portion of the cycle.

Equation (2-1) shows that for a certain voltage, the piezoelectric tube moves a set distance in the lateral direction. If the coarse approach motion is assumed to be ideal, and the coarse approach period T is specified, then the travel speed of the coarse approach mechanism can be predicted. To better illustrate the motion and to aid with the analysis, the distance traveled, Δx , per period T is plotted in Figure 2-8.

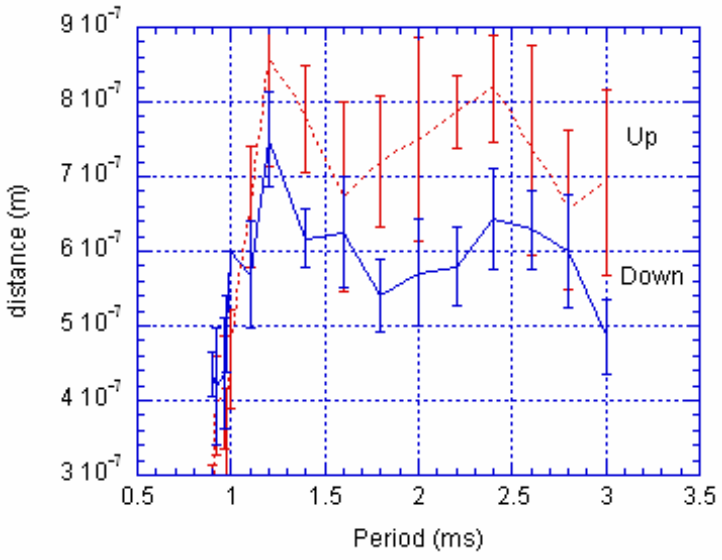

Figure 2-8 Lateral travel distance of the coarse approach mechanism as a function of the cycle period. Data is shown for the prototype STM head.

From the experimental data, the distance moved per period is rather flat for T greater than 1.2 ms. If it is assumed that the coarse approach motion is completely efficient, the piezoelectric constant d_{31} can be extracted. The average of the two travel distances (up and down) is 6.75×10^{-7} m. Using this value for Δx in equation (2-7) results a d_{31} value of 1.39×10^{-10} m $\cdot$ V^{-1}, which is about half the catalog value for the piezoelectric tubes used in the prototype. This discrepancy could be due to aging [45] in the piezoelectric tubes of the prototype STM. Also the prototype STM that these measurements were made on had one of the wires leading to a coarse piezoelectric tube broken which caused lateral drift while approaching in the vertical direction. It is most likely that the crippled piezoelectric tube is the reason that the discrepancy in the d_{31} value.

Figure 2-8 shows that for periods less than 1.2 ms, the distance traveled per period decreases. From these observations, one can estimate the acceleration value at which static friction is overcome during the stick portion of the cycle. The critical point appears to be 1.2 ms at 44 V amplitude. Using equation (2-19) this corresponds to an acceleration value for, a_s of $0.98 m/s^2$. Using equation (2-20) one can conclude a value of 0.1 for the coefficient of static friction. It is useful to know this value when determining the configuration of the waveform in the future.

Other valuable pieces of information were learned through the extensive use of this prototype head. In particular though many atomic resolution images were measured with this instrument, vibrational noise was always a significant problem and quality images could only be produced during the early morning hours when the university was relatively quiet. This will be discussed further in Chapter 3. Also thermal drift made it difficult to take consecutive scans over

the same area and spectroscopic imaging was prone to undesirable drift effects. This topic will be further discussed in Chapter 4.

2.5 Improved Design for the STM Head

In order to optimize the vibrational and thermal characteristics of the STM head it was decided that, apart from the four ceramic piezoelectric tubes, the STM head should be constructed as much as possible from one material. This choice of material was made after the following restrictions were applied: i) that the material be electrically conductive, ii) that the material have a low vapour pressure and ii) that the material be able to withstand temperatures as high as 1300 C. After that desirable properties were high thermal conductivity and low thermal expansion. After careful consideration copper and molybdenum were judged to be the best candidates. Molybdenum has a lower coefficient of thermal expansion than copper ($4.8\times10^{-6}K^{-1}$ versus $16.5\times10^{-6}K^{-1}$) and has superior refractory properties. Copper was chosen though as it has a higher thermal conductivity ($401\,W\cdot m^{-1}\cdot K^{-1}$ versus $138\,W\cdot m^{-1}\cdot K^{-1}$). It is noted that in the design of the silicon sample holder, tantalum is used for direct contact to the silicon and molybdenum parts are also used near the silicon sample. The only other components in the mechanical circuit linking the tungsten tip to the silicon sample that are not made from copper are the piezoelectric tubes, the support balls and the tube holding the tip.

As far as the choices for the piezoelectric tube dimensions go it turns out that equation (2-7) for the lateral displacement played the most important role. The reasoning was simple: to optimize stiffness and thermal conduction one should make the dimensions *a* and *t* as large as reasonably possible while making *L* small. Given the overall size scale of the STM head that is set by practical considerations dealing with the physical size of samples and tips, an outer diameter greater than about 7 mm was not feasible. A choice for the outer diameter of 6.6 mm

(0.26") was made that was consistent with this limitation and what was commercially available. The thickest possible choice for the wall thickness that allowed the inside of the tube to be coated with an electrode resulted in an inner diameter of 4.06 mm (0.16"). It is noted that the cross-sectional area of these tubes is 3.5 times greater than for the tubes in the prototype system.

Though it was tempting to make the tube length *L* very small, it was realized that if the time required to make a tip to sample approach was too long (ex. several hours) then the sample would get contaminated before the experiment could be conducted. To make a good estimate for what the optimum value of *L* should be, it was decided that 7 minutes would be the maximum allowed time to make the full up to down travel of the coarse approach mechanism i.e. almost 120 degrees of rotational motion of the coarse approach plate, and about 20 mm of lateral motion. From experience this would translate into about 30 minutes of time required to make a true approach that includes time taken to monitor the tunneling current and ensure against the possibility of the tip crashing into the surface. From the prototype results a value of 1.4 ms was used as the period *T*. These considerations mean that 300,000 cycles of stick-slip motion would need to be executed to cover the full possible motion. This gives a lower limit on the value of Δx at $6.7 \times 10^{-8}\,\mathrm{m}$. The piezoelectric material used for the tubes in the new design has a d_{31} value of -2.62 Å/V at room temperature. Use of equation (2-7) gives a minimum length *L* of 4.2 mm. This important consideration resulted in the deliberate choice of 6.35 mm (0.25") for the length of the coarse approach piezoelectric tubes. With this choice the predicted maximum lateral step (at 66 V) is $\Delta x = 1.5 \times 10^{-7}\,\mathrm{m}$. With all the key piezoelectric tube dimensions decided on, the design for the head was executed.

2.5.1 STM Head Design Details

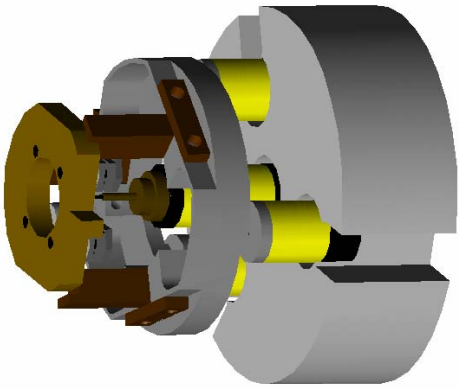

Figure 2-9 3D model of STM head

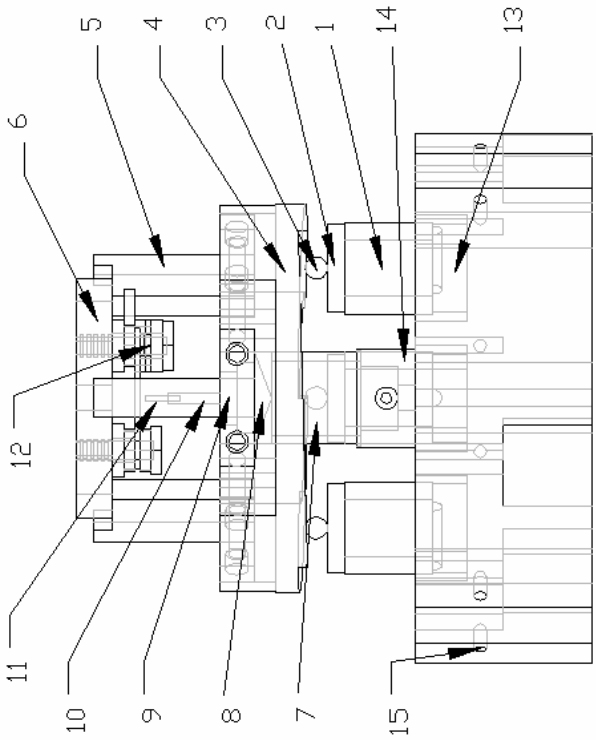

Figure 2-10 Drawing of STM head

The STM Head is shown as a 3D render in Figure 2-9 and as a 2D drawing in Figure 2-10. Each major component is numbered and dimensions are given in Table 2-2 below.

Table 2-2 Labels and dimensions for Figure 2-10

Number	Part	Material	Length / Thickness
1	Coarse Approach Piezo	Piezo (EBL #2)	6.35 mm (0.25")
2	Coarse Piezo lid	Ceramic	1.27 mm (0.05")
3	Sapphire Balls	Sapphire	1.59 mm (0.625")
4	Coarse Approach Ring	Copper	6.35 mm (0.25")
5	Sample Support	Copper	10.29 mm (0.405")
6	Sample Base	Copper	2.54 mm (0.1")
7	Scan Piezo Tube	Piezo (EBL #2)	6.35 mm (0.25")
8	Scan Tip pedestal	Ceramic	1.27 mm (0.05")
9	Tip Holder Base	Copper	2.54 mm (0.1")
10	Tip Holder Tube	Stainless Steel	3.68 mm (0.145")
11	Tip	Tungsten	1.65 mm (0.065")
12	Sample Assembly	Mo/Ceramic/Ta	6.86 mm (0.27") 19.05 mm (0.75") Diameter
13	Sample Compensator	Molybdenum	2.44 mm (0.096")
14	Tip Compensator	Copper	4.19 mm (0.165")
15	STM Base Plate	Copper	12.7 mm (0.5")

The piezoelectric tubes are made from material EBL #2 [48], which is a hard piezoelectric material and polarized radially. This material has a relatively high Curie temperature at 350 ºC and a high thermal conductivity for a ceramic. The piezoelectric property of this material is less than that of a soft material, but still high enough for STM use. The value for the Young's modulus of this piezoelectric material is 6.3×10^{10} Pa. It should be noted that the thickness of a coarse approach piezoelectric tube is different from that of the scan tube.

One of the design constraints involved the accessibility of the transfer arm (capability of tip and sample transfer, discussed in section 5.1.4) and the dimensions of the vacuum chamber

(space considerations). Much of the geometry for this scanner was designed so that it can work with previously existing tip and sample holders. In particular, the sample supports (part 5) were crucial to facilitate the transfer of the sample holder and tip in and out of the head. Additionally, the head was designed with optical access in mind. A video camera positioned outside the vacuum chamber, near an optical view port, is used to observe the tip and sample approach.

Part number 4, the coarse approach ring, is very important for the operation of the STM. The sample holder rests on this part, which in turn sits on the three sapphire balls and the coarse approach piezoelectric tubes. The bottom of the ring is polished smooth and divided into three symmetrically equivalent planes, each with the same 1.7˚ helical angle. The small angle of these planes gives the ring 0.028" or about 0.7 mm range of vertical motion when rotated through the full 120˚ available. The top side of the coarse approach ring was machined so that large portions of the piece were removed in order to reduce the mass, but with little sacrifice in strength, rigidity and thermal conduction properties. The mass load on each of the three coarse approach piezoelectric tubes is 20.5 grams i.e. 0.20 N of normal force. The maximum lateral force F_x that be applied during a coarse approach step can be calculated using equation (2-19). Again, using the maximum possible voltage of 66 V, the value for F_x is 5.9 N i.e. about 30 times larger than the normal force. Thus, with a coefficient of static friction between sapphire and copper expected be less than one, it is seen that the lateral force generated by the coarse approach piezoelectric tubes is more than adequate to induce the slip portion of the approach cycle.

The acceleration during the stick portion of the coarse approach cycle can also be predicted using equation (2-21). With V_0 = 66 V and T = 1.4 ms, one obtains a value for a_s of 0.15 m/s^2 or 0.016 g. Thus, as long as the coefficient of kinetic friction is not less than 0.016 the stick portion of the motion should proceed as expected. In case slipping does actually occur in

practice one would simply decrease V_0 or increase T accordingly until the slipping went away, with the price being paid of waiting longer for the coarse approach procedure to finalize.

2.6 Construction of the STM Head

Following the design phase, the STM head was constructed and assembled. Tests on the STM head were performed in order to quantify improvements over the prototype design. Figure 2-11 shows a photograph of the STM head.

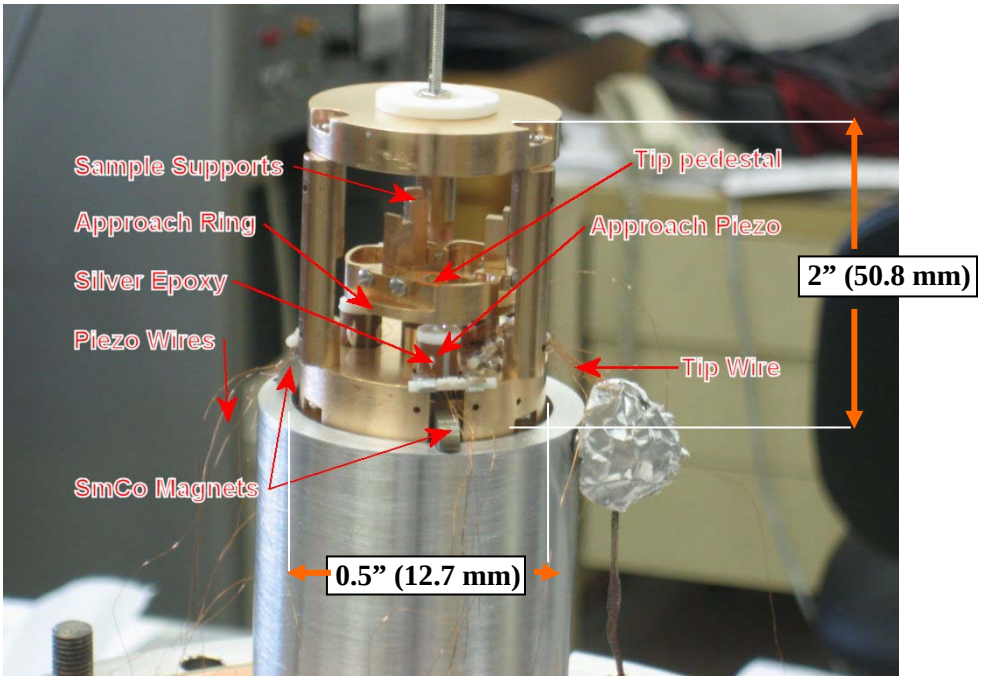

Figure 2-11 Labeled photograph of the constructed STM head shown without the stainless steel disk and resting on the pedestal

2.6.1 Wiring

The wiring for the STM was done using 40 AWG insulated copper wire from Wiretronic Inc [49]. The thin polymer insulation on the wires is hard and should not cause excessive

outgassing. The wires are small to reduce the impinging vibrations on the STM head. Also, the wires are clamped to the STM base edge and not to the piezoelectric tubes in an effort reduce the amount of vibration impinging on the piezoelectric tubes. The wires were epoxied to the piezo using the H21D silver conductive epoxy from Epo-tek [50]. There are five wires to each of the four piezoelectric tubes, one wire to ground the STM chassis, a tip signal and tip ground wire, and one sample bias wire. The tip shield wire also serves as the inside electrode for the scan piezo, making a total of 23 wires. These wires are fed into the vacuum chamber using a type-D 25 pin subminiature feedthrough which is UHV compatible. This feedthrough is available from MDC Vacuum Products Inc [51].

For the tip wire, it is important that there is sufficient shielding because the tunneling current is very small (a few hundred Pico amperes typically) and susceptible to noise. The shield wire is wrapped around the tip wire where it attaches to the STM head. This tip wire changes to coaxial shielding at the top of the pedestal (right below the label for the tip wire in Figure 2-11). The total length of the tip wire from the STM head to the coaxial wiring is approximately 5 cm (2”). The ground wire to the STM is important to prevent the buildup of charge in a floating conductor. Once the STM is raised on the springs, this wire electrically grounds the STM chassis.

2.6.2 Construction

The STM was constructed using stainless steel screws where possible, but many components could not be screwed together and needed to be joined with epoxy. Because the instrument functions in ultra high vacuum, the type of epoxy is important because the wrong kind will lead to excessive outgassing. Dexter Hysol ® Epoxi-Patch structural adhesive was used in the construction of the STM. The wires that connect to the piezoelectric tubes and the tip and sample are connected using a special silver conductive epoxy H21D made by Epoxy Technology

that has very low levels of outgassing. The epoxy is unique in the sense that it is made from completely components with a low vapor pressure. Although these epoxies are UHV compatible, care is nevertheless taken to use as little as possible.

Every component except for the piezoelectric ceramics was also gold sputter coated after polishing the metal surfaces with steel wool. The gold coated low emissivity surface lowers the thermal radiation load and may decrease thermal drift problems. Many low temperature devices use gold to help in the ability to regulate temperatures.

The entire construction process was completed in only two days, following which, the microscope was tested in atmosphere to ensure the coarse approach mechanism functioned properly. Shortly after this testing, the microscope was placed into the UHV chamber. The base pressure of the chamber was very low after the bake, indicating that there were no trapped gasses. Soon after, the microscope was producing images. The entire design, construction, and installation process was a complete success.

2.7 Coarse Approach Performance for the New Design

The coarse approach mechanism was found to work well at 44 Volts amplitude and a 1.4 ms period. At these settings, the travel speed of the coarse approach ring was measured to be 1.6×10^{-7} m per cycle. This is reasonably close to the predicted value of 1.0 x 10^{-7} m using equation (2-7). Even with a 60% discrepancy this result has to be considered a major success. That the motion of a coarse approach stick-slip system could be modeled with any accuracy was not known at the outset of this project.

Even with piezoelectric tubes that are rather short, wide and thick-walled, the coarse approach mechanism still functions very well and quite close to predicted rates of motion. One limitation with this system is that the lateral range of the scan tube is less than it is in most other

STM systems. Here, the lateral range with ±130V applied to the scan tube is ~150 nm. This makes it difficult to scan over large scale features. Given that the primary purpose of the instrument is to study adsorbates on the atomic scale, this limitation is not severe. Typically scans are taken over areas of about 10 nm across or even less.

With all of the parameters and properties of the piezoelectric tubes chosen, one can, for example, calculate the maximum vertical motion from equation (2-1). With the full 130 V available from the RHK controller a Δz value of ~170 nm can be obtained. This is essentially the "reach" of the feedback control while tunneling, so the coarse approach mechanism must bring the tip to within this range of the sample. With 1.6×10^{-7} m of lateral motion, the vertical motion at 1.7° is 3.0×10^{-9} m i.e. the system has 3 nm of vertical coarse positioning precision, 56 times less than the available reach. This makes it quite easy to position the tip within tunneling range of the sample since the feedback control takes over once the tip is within the reach of 170 nm.

The construction of a workable coarse approach system has allowed STM experiments on Si(111)7x7 to be conducted. In the following two chapters the levels of vibrational and thermal drift in these experiments are discussed in detail.

Chapter 3
Vibration Isolation

3.1 Transmission of Vibrations and Isolation from Vibrations

In order to isolate the STM experiments from vibrations, a good understanding of how vibrations are transmitted to the microscope is needed. Following that, steps can be taken to limit the transmission of these vibrations. In addition to eliminating the transmission of vibrations, the vibrations should be dampened to eliminate ringing. Finally, there cannot be any mechanical "antennas" which resonate at undesirable frequencies causing added noise. The techniques used for vibration isolation have been studied and explained by many others [52]. For our experiment, the most practical and efficient types of isolation were selected and implemented. To begin, the theory of vibration isolation is discussed.

3.1.1 Transmission of Vibrations Through Solids

For vibrations to be transmitted to the STM head, they must travel through solids. There are two types of vibrations that can cause problems for STM: transverse and longitudinal waves. Transverse waves such as those that travel down a string, and longitudinal waves like sound waves can cause noise problems if there is a lack of rigidity in the construction in the STM head. Longitudinal waves are compression waves that become a problem when components have a geometry in which these waves excite resonances in structural components causing ringing.

As vibrations are transmitted, there is energy transmitted as waves in the form of physical motion. When transmission of waves is discussed, it is the physical motion caused by this

transmission that is the problem considered. As a longitudinal or transverse wave passes through a material, each point along the way moves slightly. The problems that need to be analyzed are the amplitude of this motion and the frequency of this motion. The problem due to vibrations can be minimized by a combination of minimizing the amplitude of motion and eliminating the frequencies of motion that the instrumentation is most sensitive to, in addition to the careful design of the STM head.

The speed of transmission of vibrations generally depends on the materials they travel through. Denser materials will transmit vibrations faster than softer materials. Unfortunately, slowing down speed of transmission does not eliminate them. The energy from the waves is still transmitted. For waves traveling through a solid, the system behaves as a spring. Depending on the situation, the solid can be viewed as a system of infinitesimally small springs and masses connected together. The motion of the wave in the solid material is governed by Hooke's law.

$$f = -k \cdot d \qquad (3\text{-}1)$$

Where k is the spring constant, and d is the displacement. For a solid material, the spring constant depends on the material properties, and the displacement is dependent on time and position in the material. Considering a solid rod, if a piece of material normally at position *x* is displaced an amount ξ, then the stress in that material is given by the stress-strain relationship, and Hooke's law can be re-written [47] as

$$f = -SY \frac{\partial \xi}{\partial x}. \qquad (3\text{-}2)$$

Where *S* is the cross section and *Y* is the Young's modulus. Using this relationship for the forces within the material, the equation of motion is that of a wave with a speed

$$c = \sqrt{\frac{Y}{\rho}}\,. \qquad (3\text{-}3)$$

Where ρ is the density of the material.

Controlling the speed of vibration transmission will not help to alter the transmission of the waves. Fortunately, there is a strong dependence on the frequency of the waves transmitted and the amplitude of the transmission. Waves of different frequencies will have different transmissibilities through a material.

By analyzing solid components as springs, a resonant frequency for that material can be found. For longitudinal vibrations, the resonant frequency will depend on the properties of the material. The frequency of oscillation will depend on the boundary conditions of the bar. The equation of motion of the bar is [47]

$$\frac{\partial^2 \xi}{dx^2} - \frac{1}{c^2}\frac{\partial^2 \xi}{\partial t^2} = 0\,. \qquad (3\text{-}4)$$

The solution to this wave equation is

$$\xi = Ae^{i(\omega t - k x)} + Be^{i(\omega t + k x)}\,. \qquad (3\text{-}5)$$

In this case, $k = \omega/c$ and is the wave number. The solution is a superposition of left traveling and right traveling harmonic waves.

When an end of the bar is free to move, the boundary condition at that end is $\frac{\partial \xi}{\partial x} = 0$. When the bar is clamped, the boundary condition is $\xi = 0$. The solutions to the harmonics for each set of boundary conditions are given below.

Table 3-1 Longitudinal harmonics of an oscillating bar

Free-Free Bar	$\omega_n = n\pi \frac{c}{L}$
Fixed-Fixed Bar	$\omega_n = n\pi \frac{c}{L}$
Free-Fixed	$\omega_n = \frac{(2n-1)\pi}{2} \frac{c}{L}$

For transverse waves, the harmonic frequencies can be calculated in a similar fashion. The equation of motion for a transverse wave in a bar is [47]

$$\frac{\partial^2 y}{\partial t^2} + \kappa^2 c^2 \frac{\partial^4 y}{\partial x^4} = 0 \qquad (3\text{-}6)$$

The speed of transmission is dependent on the frequency as well and the cross sectional geometry of the material.

$$v = \sqrt{\omega \cdot c \cdot \kappa} \qquad (3\text{-}7)$$

Here, κ is a radius of gyration, which arises due to a bending moment. The boundary condition for a clamped end is $y = 0$ and $\frac{\partial y}{\partial x} = 0$. For a free end, $\frac{\partial^2 y}{\partial x^2} = 0$ and $\frac{\partial^3 y}{\partial x^3} = 0$. The solution for the frequencies of oscillation with these boundary conditions is transcendental. The functions describing the solutions are given below

Table 3-2 Transverse harmonics of an oscillating bar

Free-Free Bar	$\tan\left(\frac{\omega L}{2v}\right) = \pm\tanh\left(\frac{\omega L}{2v}\right)$
Fixed-Fixed Bar	$\tan\left(\frac{\omega L}{2v}\right) = \pm\tanh\left(\frac{\omega L}{2v}\right)$
Free-Fixed Bar	$\cot\left(\frac{\omega L}{2v}\right) = \pm\tanh\left(\frac{\omega L}{2v}\right)$

These equations are important for the calculation of the resonant frequencies of the STM components, most notably the piezoelectric tubes in the STM head. The easiest way to solve these equations for ω is numerically.

3.1.2 The Damped Harmonic Oscillator

The transmission of vibration across a spring is most easily analyzed by looking at the dynamics of a forced, damped harmonic oscillator.

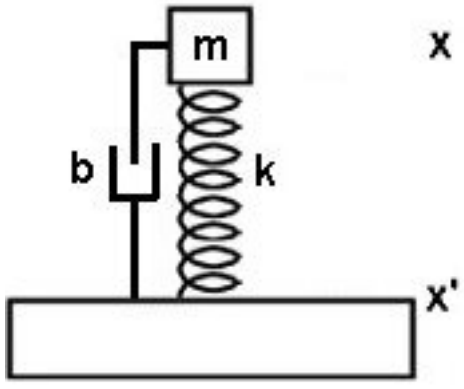

Figure 3-1 Fixed-free loaded spring

Here, *b* is the dampening coefficient and *k* is the spring constant. *x* and *X'* are the position of the mass and the base respectively. The equation of motion for this system is

$$m\ddot{x} + b(\dot{x} - \dot{x}') + k(x - x') = 0 \qquad (3\text{-}8)$$

This solution to this equation is simply the harmonic solution

$$x(t) = Ae^{i\left(\sqrt{\omega^2 - \left(b/2m\right)^2}\right)t} \qquad (3\text{-}9)$$

When the base oscillates harmonically at a frequency ω. *A* is the amplitude of oscillation. To better understand this system qualitatively, two substitutions can be made. The resonant frequency for the spring is

$$\omega_0 = \sqrt{\frac{k}{m}} \text{ (Hz)}, \qquad (3\text{-}10)$$

and a variable γ is defined as

$$\gamma = \frac{b}{m} \text{ (Hz)}. \qquad (3\text{-}11)$$

γ has the same units as ω, it directly relates to the dampening of the spring. If τ is the time required for an oscillation to decrease by $1/e$, then $\gamma = 1/\tau$. Another way to represent the damping is with the quality factor or *Q* value [53].

$$Q = \frac{\omega_0}{\gamma} \text{ (dimensionless)} \qquad (3\text{-}12)$$

The *Q* value is dimensionless, and related to the number of oscillations that are made before the spring is dampened out (higher *Q* value, the more oscillations). The transfer function is the ratio of

vibrations from the base with respect to the oscillation of the load. Another term for the transfer function is transmissibility. The transfer function is frequency dependent. That is,

$$T(\omega) = \left| \frac{A}{A'} \right| \text{ (dimensionless)} \qquad (3\text{-}13)$$

After substituting the results from (3-10) and (3-11) into (3-13), the transfer function [52] is

$$T_L(\omega) = \left| \frac{\omega_0^2 + i\gamma\omega}{\omega_0^2 - \omega^2 + i\gamma\omega} \right| \qquad (3\text{-}14)$$

This transfer function represents a type of low pass filter. Equation (3-14) can be re-written as:

$$T_L(\omega) = \sqrt{\frac{1 + \dfrac{\omega^2}{\omega_0^2 Q^2}}{\left(1 - \dfrac{\omega^2}{\omega_0^2}\right)^2 + \dfrac{\omega^2}{\omega_0^2 Q^2}}}. \qquad (3\text{-}15)$$

The transfer function is plotted below in Figure 3-2 for two values of *Q*. There is a sharp peak at $\omega = \omega_0$ where the transfer function is greater than one. This means that for low frequencies, the amplitude of vibrations is actually amplified. However, the transfer function quickly drops off, which means that vibrations do not transfer across the spring. As long as the resonant frequency is as low as possible, the net effect will be the reduction of vibration amplitudes at high frequencies. The lower frequencies can be dealt with in other ways, such as the transfer function of the STM head itself.

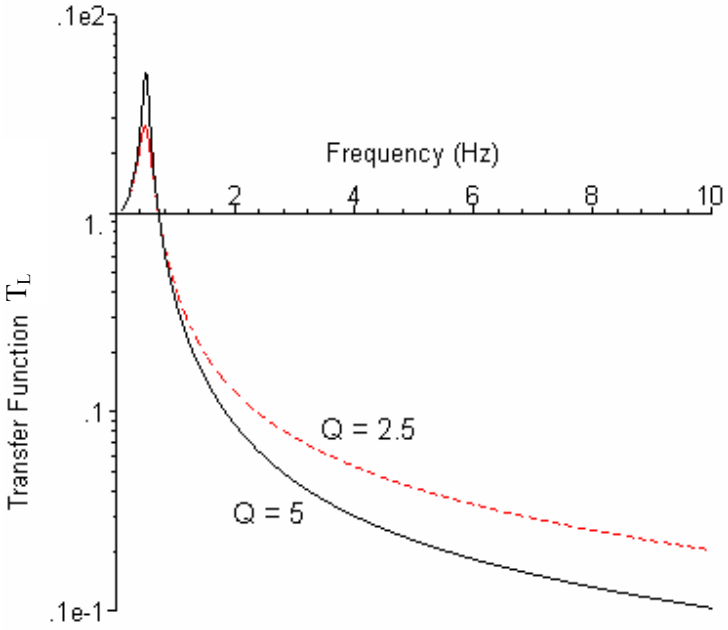

Figure 3-2 The effect of dampening on the transfer function of a spring

The next real problem is the quality factor of the resonance in the figure above. A high quality factor means that if the resonance is stimulated, it will oscillate many times before being damped out. The way to reduce the quality factor is to increase the dampening coefficient. But this means that the transfer function will also change. When the dampening is increased, the size of the resonance peak decreases, but the efficiency of the isolation at higher frequencies is reduced. A balance must be found between reducing the quality factor and efficiency of isolation. At frequencies less than the resonant frequency, the transfer function becomes linear. Too much dampening will reduce the isolation at the frequencies of interest (1-8 kHz), and too little will result in unacceptable and persistent resonances. Depending on the application, the dampening can be tuned to achieve the desired situation.

3.1.3 Vibration Isolation Steps Used for the STM

Before considering the vibration isolation of the microscope, the vibration sources should be considered. Ideally, the STM experiment should be placed in the quietest place possible. Unfortunately, at the University of Lethbridge, this choice is limited to where laboratory space is available. The STM lab is located on the seventh floor and the environment is unsheltered from noise. The shape of the building is a wind barrier and in the city of Lethbridge, wind is very common. Even though the UHV chamber is placed as close as possible to the building's support structure in an effort to avoid extra structural vibrations in the laboratory, all these factors make for a very noisy environment.

To isolate the experiment from the ambient vibrations in the room, several stages of vibration isolation are used. High pass and low pass filters are used to isolate the system from external vibrations. Firstly, the construction of the microscope is rigid to isolate from low frequency resonant vibrations in the microscope. Of course, a rigid construction does not eliminate vibrations, but helps prevent the transmission or amplification of them. The rigid construction, in addition to the small size of the STM head greatly eliminates low frequency vibrations within the microscope head itself. A low frequency noise will result in the entire apparatus moving at the same rate, which does not cause the tunnel junction separation to change. The vibrations that cause variations in the tunnel junction that are of major concern.

Secondly, the microscope is suspended by three soft (low spring constant k) springs inside the vacuum to help prevent high frequency vibrations from transferring to the microscope. The transfer function of these springs falls off at higher frequencies and is large at its low resonance. The low resonant frequency means that the low frequency vibrations that do reach the STM head are of little concern to the operation of the microscope because the rigid design protects the tunneling functionality against low frequency vibrations. At this point, the springs have blocked the high

frequency vibrations and the rigid design has blocked the low frequency vibrations from influencing the experiment.

In addition to these measures to prevent vibrations from reaching the tunnel junction, Six SmCo magnets provide eddy current dampening to the motion of the springs. The magnets are arranged in such a way as to dampen vibrations along all three axes, plus the rotational axis. Although the dampening does reduce the efficiency of the spring's ability to block high frequency vibrations, the benefit of draining energy from the low frequency motion of the springs means that there is less risk of causing the microscope to oscillate uncontrollably.

Third, the entire vacuum chamber is placed on a Minus-K biscuit isolation table model 500BM-1. This table with a resonant frequency of ~0.5 Hz also helps to isolate high frequency vibrations from the microscope. The fourth stage of isolation is a sand box on which the biscuit sits. The soft sand helps to absorb vibrations [54].

The STM is constructed so that the first harmonic longitudinal and transverse frequencies are very high. Because of the extensive vibration isolation between the STM head and the environment is efficient at blocking out high frequencies; these frequencies will be greatly attenuated in the STM head. The construction with high vibrational resonances in the microscope head works in conjunction with the external vibration isolation to eliminate the effect of low frequency vibrations at the tunneling junction.

3.2 Vibrational Analysis of the STM Head

There are many stages of vibration isolation leading up to the microscope head. Even so, any undesired resonant frequencies in the head will amplify any vibrations that might make it through to the STM head. There are four main considerations that need to be made for vibration problems.

First, the base plate has to be designed such that any plate modes will not cause vibration problems in imaging. The fundamental plate mode is the most devastating plate mode affecting the operation of the STM. The center of the plate will move up and down relative to the circumference. This is undesirable because the sample is mounted from the circumference and the tip from the center. If this vibration is too large, then it will be impossible to hold a steady tunneling junction, as the tip and sample will be moving harmonically 180 degrees out of phase.

Second, longitudinal vibrations in the components must be minimized. These are vibrations that travel down the length of the material oscillating parallel to the direction of motion. These vibrations are generally at higher frequencies and are of minimal concern. The resonant frequencies of individual components are somewhat of a concern here, but the resonant frequencies can be made large by simply keeping the components short.

Third, lateral vibrations must be considered. These are the vibrations that oscillate perpendicular to the direction of wave motion. These vibrations depend on the rigidity of the material. Softer materials will have larger lateral vibrations than harder materials. Also, they depend on the thickness of the material. Think of the ability to make a thin wire oscillate like a wave compared to a steel rod. Maximizing the thickness of components will help to minimize the problems caused by lateral vibrations. Also, the thickness of the piezo tubes is important here as they are the softest component and most likely to cause problems. Having thicker walled and large radius piezo tubes minimizes the likelihood of low frequency resonances.

Fourth, there must be dampening to the vibrations. In the event that the microscope is stimulated, those vibrations should be quickly damped. If there is a stimulated resonant frequency with a high quality factor, it will ring several times before decaying adding to the problem.

3.2.1 Vibration of the Base Plate

The STM base plate is the component that connects the tip and the sample vibrationally. This is why it is very important to consider the vibrational characteristics of this plate. The sample is essentially connected to the circumference of this plate and the tip to the center. If the base plate was soft, it is easy to see how it could behave like a flexible diaphragm causing vibrations between the tip and sample. For this reason, it is important that the base plate is as rigid as possible. This is accomplished by making it very thick. The plate is almost as thick as its radius, which means that it is very difficult to bend.

The analysis of a vibrating plate has been well analyzed by others [47]. For our needs, the base plate is treated as a circular plate which is free on the edges. The solution of the wave equation gives motions in several normal modes. It is important to know the mode with the lowest natural frequency and to ensure that this frequency is sufficiently high. This ensures that the base plate is rigid enough. The frequency of the fundamental mode is

$$f_1 = 0.47 \frac{d}{a^2} \sqrt{\frac{Y}{\rho\left(1-\sigma^2\right)}}, \qquad (3\text{-}16)$$

where Y is the Young's modulus, d is the thickness of the plate, a is radius, ρ is the density (g/m^3), σ is the Poisson's ratio (dimensionless). Poisson's ratio is a measure of a tendency of a material to deform during a deformation in a direction perpendicular to stretching or compression. In the case of the base plate for this design, the material is copper.

Table 3-3 Dimensions and values for calculating the STM base plate vibrations

Item	Value
d	12.7 mm (0.5”)
a	38.1 mm (1.5”)
Y	122 GPa
ρ	8900 $Kg \cdot m^{-3}$
σ	0.35

Using the values in Table 3-3, the fundamental oscillation frequency of the STM base plate (assuming a solid plate) is 65 kHz. This very high value suggests that this type of resonance will not be a problem for the STM. Of course, this analysis is over simplified. In actuality, the base plate for the STM is not a perfect disk. There are small volumes of material removed changing the mass and making the oscillations more complex. This may cause the actual fundamental plate mode to be slightly lower than calculated here.

3.2.2 Vibration of the Tip

The vibration of the tip, shown in Figure 3-3, is analyzed from the bottom of the base plate to the end of the tip. The small size of the tip and holder is good news from the perspective of vibration isolation. There is very little mass on the tip structure which means the tip structure will be lightly loaded.

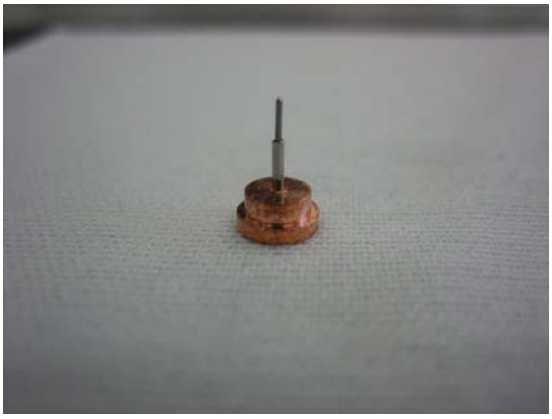

Figure 3-3 STM tip and tip holder

The size of the tip and holder from top to bottom is 7.62 mm (0.3") tall. The bottom plate has a diameter of 5.08 mm (0.2"). The weakest point in the tip structure from a vibrational point of view is the piezo scan tube. To analyze the fundamental mode of the scan tube, it will be treated as a free-mass loaded bar. In the limit of zero (infinite) mass-loading, it will be a free-free (clamped) bar described by the equations of Table 3-1 and Table 3-2. This is not an exact value but a good approximation. From analysis in the method of reference [47] the fundamental longitudinal frequency can be found using the formulas:

$$\cot(kL) = \frac{M_{load}}{M_{bar}} kL \qquad (3\text{-}17)$$

$$f_1 = k\sqrt{\frac{Y}{\rho}}\,. \qquad (3\text{-}18)$$

For the piezoelectric scan tube, Y is 610 GPa, the density is 7650 $Kg \cdot m^{-3}$. The dimensions of the piezoelectric tube are shown in Table 3-4.

Table 3-4 Piezoelectric tube dimensions

Part	Dimension	Value
Scan tube	Length	6.35 mm (0.25”)
Scan tube	OD	6.6 mm (0.26”)
Scan tube	ID	5.33 mm (0.21”)
Approach tube	Length	6.35 mm (0.25”)
Approach tube	OD	6.6 mm (0.26”)
Approach tube	ID	4.06 mm (0.16”)

The mass of the tip is 0.00178 Kg. The value of k is found numerically from (3-17). From these values, the fundamental frequency is calculated to be 58.5 kHz. This is sufficiently high to eliminate problems from vibrations in the STM Head. Here, it can be seen that to increase the resonant frequency, the mass of the load can be reduced or the mass of the bar can be increased. Additionally, the length of the piezo tube can be reduced, but this will come at the expense of the piezo tube functionality for STM.

3.2.3 Vibration of the Sample

The sample will vibrate from the bottom of the base plate to the sample holder platforms. The most suspicious component here is the sample holding supports. They are the smallest component. An additional concern is the coarse approach piezoelectric tubes. Using the same methods as was used to calculate the resonant frequencies of the tip, the resonant frequency of the sample coarse approach tubes can be calculated. For this calculation, the mass of the load is 20.5g. There are three piezo tubes so this load is distributed.

The coarse approach tubes which support the sample have a different geometry than the scan tube, as shown in Table 3-4. This increases the mass of the tube and the rigidity. From the geometry and material of the piezoelectric tubes, the resonance frequency is calculated to be 26.8 kHz. This is

a bit less than the tip because of the additional weight, but sufficiently high for the operation of the STM.

The vibration of the sample supports can be calculated by a similar method. The support is approximated to be a tube, even though it is really a square rod. The mass of the sample and holder is approximately 0.5 g. The supports are made of copper and are 0.762 cm (0.3") long and there are three supports holding up the sample. The fundamental longitudinal frequency is ~42 kHz. This is larger than that of the piezoelectric tube because the mass on the sample supports is much less than the mass on the coarse approach piezoelectric tubes. The sample supports are not required to hold up the coarse approach ring.

3.2.4 Simple Model of Vibrations at Tunneling Junction

In addition to all the considerations for the individual vibrations down the tip and sample paths, the resonant frequency of both the tip and sample should be similar. If it is assumed that both the tip and sample receive vibrational stimuli from the same source, then it can also be assumed that vibrations down the tip path and sample path start out with the same phase. If this is true, then matching the natural frequencies of the two will cause the junction to vibrate up and down at the same rate and the net deviation in the junction caused by the vibrations will be minimized.

The part of the STM head above the base plate can be modeled as a system of two springs and two masses connected to a common plate. One spring represents the mechanical path leading to the sample with mass m_s, and the other spring represents the mechanical path leading to the tip with mass m_t. In this simple model, the resonant frequency of the parts is ignored and each path is treated as an effective spring having a resonant frequency equal to the frequency of the lowest fundamental mode for that path. Figure 3-4 illustrates this model.

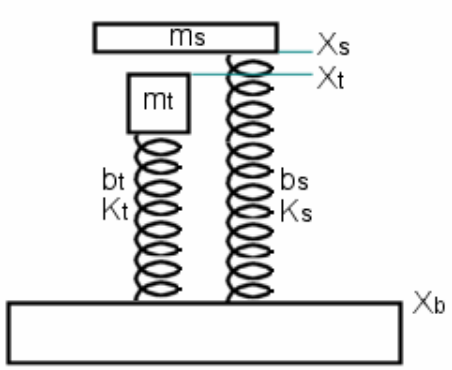

Figure 3-4 Illustration of the tip and sample as a system of springs

In Figure 3-4, *k* and *b* are the spring constants and dampening coefficients and *x* denotes the position of components. Here, the reasonable assumption is made that any vibrations traveling to the tip and sample are going to be treated like a forced oscillation of the base. Therefore, the motion of X_b will be the impulse to the system. From here, the equations of motion for the tip and sample can be easily written.

$$m_s\ddot{x}_s + b_s\left(\dot{x}_s - \dot{x}_b\right) + k_s\left(x_s - x_b\right) = 0 \qquad (3\text{-}19)$$

$$m_t\ddot{x}_t + b_t\left(\dot{x}_t - \dot{x}_b\right) + k_t\left(x_t - x_b\right) = 0 \qquad (3\text{-}20)$$

The base will oscillate with a frequency of ω_b and amplitude of x_b. The solutions to the equation of motion are:

$$\frac{x_s}{x_b} = \frac{\left(\frac{i\omega_b\omega_s}{Q_s} + \omega_s^2\right)}{\left(-\omega_b^2 + \frac{i\omega_b\omega_s}{Q_s} + \omega_s^2\right)}, \text{ and} \qquad (3\text{-}21)$$

$$\frac{x_t}{x_b} = \frac{\left(\frac{i\omega_b\omega_t}{Q_t} + \omega_t^2\right)}{\left(-\omega_b^2 + \frac{i\omega_b\omega_t}{Q_t} + \omega_t^2\right)}. \qquad (3\text{-}22)$$

These equations describe a high pass filter. Vibrations will not be transmitted effectively when ω_b is less than ω_s and ω_t. Low frequency oscillations from the base will be attenuated. This shows why it is important to make the STM head to be as rigid as possible. From here, the final substitution is made and the ratio of the tip and sample vibrations can be found.

$$\frac{x_s}{x_t} = \frac{\left(1 + \frac{i\omega_b}{\omega_s Q_s}\right)\left(1 - \frac{\omega_b^2}{\omega_t^2} + \frac{i\omega_b}{\omega_t Q_t}\right)}{\left(1 + \frac{i\omega_b}{\omega_t Q_t}\right)\left(1 - \frac{\omega_b^2}{\omega_s^2} + \frac{i\omega_b}{\omega_s Q_s}\right)} \qquad (3\text{-}23)$$

or, more importantly, the amplitude of the oscillations at the tunnel junction for a certain amplitude of perturbation $\frac{x_s - x_t}{x_b}$ can be calculated. This value is the transfer function of the STM head. As discussed before, the resonant frequency of ω_s and ω_t is large. In this limit, the higher order terms of ω_b can be removed and the result is very simple at low frequencies:

$$T_H = \frac{x_s - x_t}{x_b} \approx \omega_b^2\left(\frac{1}{\omega_s^2} - \frac{1}{\omega_t^2}\right). \qquad (3\text{-}24)$$

Note that the dependence on the quality factor falls out for the low frequency approximation.

In order to plot the full transfer function, the quality factors would need to be known. While it is difficult to calculate the quality factor for the sample and tip accurately, it is feasible to obtain a reasonable estimate for this value, as follows. The quality factor can be measured from a Fourier

transform of the resonance $Q = \omega_0 / FWHM$. *FWHM* is the Full Width at Half Maximum. The larger the quality factor, the larger the resonant peak will be at each tip and sample resonant frequency. For this plot, a quality factor of 20000 will be used for both the sample and the tip. The quality factor of this type of ringing was determined from peaks measured in FFT data presented later. Using ω_s = 26.8 kHz and ω_t = 58.5 kHz, the transfer function is plotted in Figure 3-5.

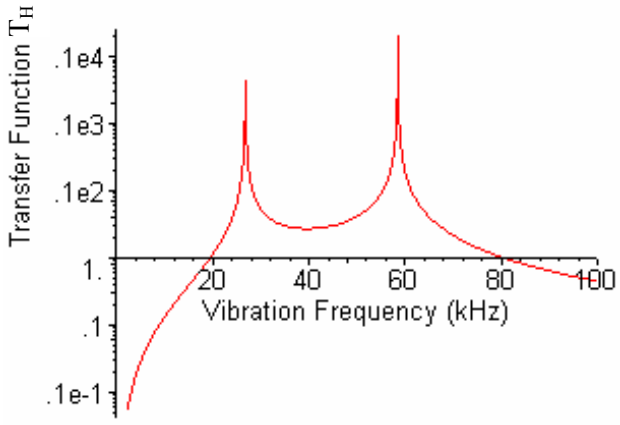

Figure 3-5 Transfer function of the STM head

It is important to note that the transfer function approaches zero at low frequencies. Also, the larger the resonant frequencies are, the lower the transfer function at low frequencies. For this reason, it is fruitful to design a system that forces these resonant frequencies to be as high as possible, virtually eliminating the low frequency transfer function.

3.2.5 Transfer Function of the Vibration Isolation

The transfer function can be calculated for all the vibration isolation steps used. There are three main steps in the vibration isolation: i) the biscuit, which can be treated like a DHO ii) the DHOSM, and iii) the STM head itself. The transfer function for the STM head was already discussed

in section 3.2.4. For the other two, the resonant frequency and the quality factor must be known. The resonant frequency can be found by measuring the period of the oscillation when the spring is perturbed. For the biscuit, the resonant frequency is approximately 0.48 Hz. The resonant frequency for the DHOSM is about 1 Hz.

The quality factor can be estimated by observing the number of oscillations the spring makes when perturbed. The amplitude of oscillation will fall by a factor of e in approximately Q/π periods [53]. From observations of the transient response of the biscuit when perturbed, which is about 4 oscillations, the quality factor is estimated to be approximately 5. From the data available from the Minus-k website [55], the quality factor can be extracted to be approximately Q=5. For the DHOSM, the quality factor is approximately 3. This is shown in Figure 3-6.

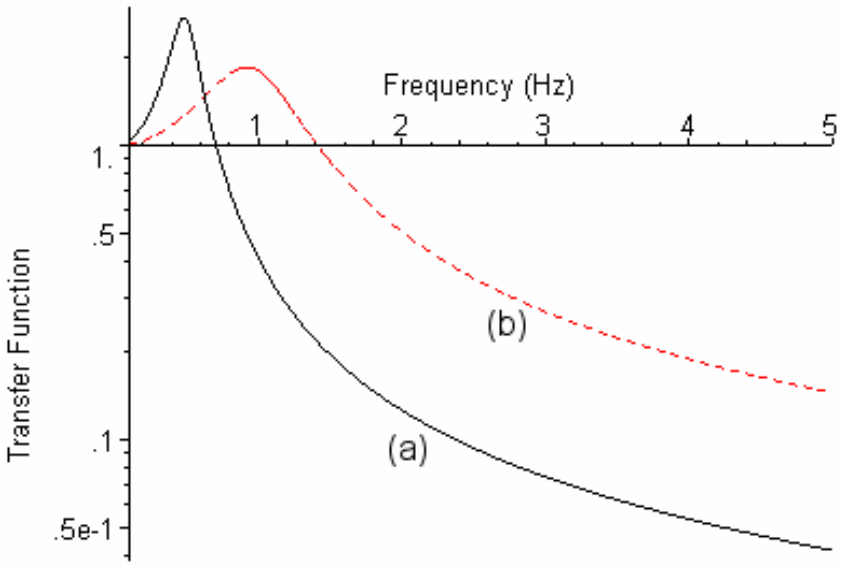

Figure 3-6 Transfer functions of the (a) biscuit and (b) DHOSM

The total transfer function for vibrations from the environment to the STM is:

$$T = T_{Head} \cdot T_{DHOSM} \cdot T_{Biscuit}, \qquad (3\text{-}25)$$

where T_{Head} is given by (3-24), and T_{DHOSM} and $T_{Biscuit}$ are given by (3-15).

The total transfer function is plotted in Figure 3-7. The peaks labeled a and b correspond to the peaks in Figure 3-6, and peaks c and d correspond to those in figure Figure 3-5. The peak heights, however, are greatly reduced due to the two sets mutually canceling transmissions through each other. That is, the high resonances reduce transmission through low frequencies, and vice-versa.

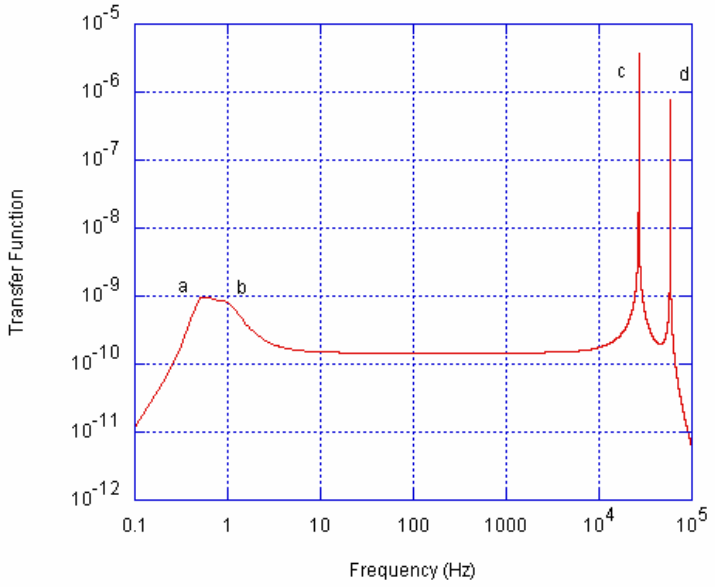

Figure 3-7 Total transfer function of all vibrational isolation stages a) biscuit resonance b) DHOSM resonance c) sample resonance d) tip resonance

This analysis of overall transfer function is admittedly oversimplified. Internal resonances in the biscuit and the springs will lead to a transfer function higher than predicted. Even so, the effects of each isolation stage are visible and the general statement is made that two things need to be done to

isolate from vibrations. The low pass filter frequencies (DHO) need to be pushed as low as possible and the high pass filter frequency (rigidity) as high as possible.

In the range of frequencies important for STM, the amplitude of vibrations is greatly reduced. The important range for operation is the frequencies near the feedback bandwidth and the higher frequencies which are needed to do spectroscopic imaging (~5 kHz). Frequencies below about 0.1 Hz are filtered out by the imaging software. This extreme isolation is important for the operation of the STM.

3.3 Resonant Frequencies of the Head

To quantify the vibrational characteristics of the STM head, vibrational spectra are collected. This can be done many ways. One way this data can be collected is using mechanical stimuli and measuring the response. Alternatively, the noise spectrum can be measured in the STM tunneling current. Any vibrations from mechanical oscillations in the STM head will be seen as noise in the current signal.

3.3.1 Mechanical Vibrational Spectrum

The resonant frequencies of the prototype microscope were measured using the scan tube to stimulate vibrations and a SR830 lock-in amplifier to simultaneously measure vibrations. The vibrations were measured from 2 kHz to 100 kHz. The amplitude of the signal is arbitrary. The spectrum is acquired using a single piezoelectric electrode. The piezoelectric material will induce a current that is proportional to the amount of vibration it experiences. A sine wave is swept through the frequency range and through a resistor. The voltage drop across the resistor corresponds to the current in the circuit and measuring this drop using the lock-in amplifier will indicate the amount of motion of the piezoelectric tube. When a resonance is reached, there will be more motion and a larger signal. The result of this measurement is shown in Figure 3-8.

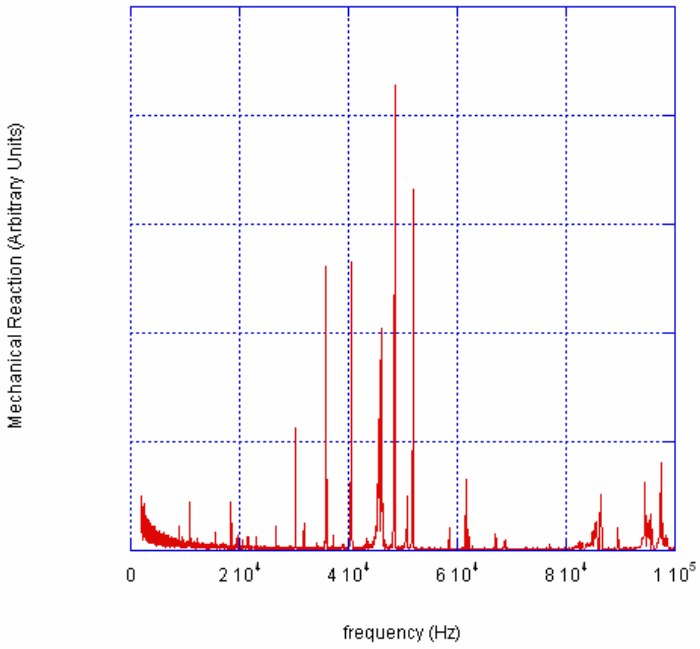

Figure 3-8 Measured vibrational spectrum of the prototype STM head

There are many low frequency resonances in the 10 kHz to 20 kHz range, possibly some lower. These are due to the fact that the microscope is not as rigid as it could be. The magnitudes of the individual peaks is important, however, difficult to quantify with this technique. Instead, the relative magnitudes of the frequencies gives important information on the mechanical properties of the STM head. The same experiment was repeated on the new STM head.

Many of the resonant frequencies are now gone and the spectrum is much cleaner in Figure 3-9. Most of the major resonances are now located above 50 kHz. There are a few resonances near 20 kHz which is attributed to the lateral vibrations of the microscope frame. The high values of these resonant frequencies mean that there will not be any problems from resonant vibrations in the STM imaging. Frequencies above 100 kHz were not measured, as they will have little effect on the experiment. This same measurement was then made using an alternate technique.

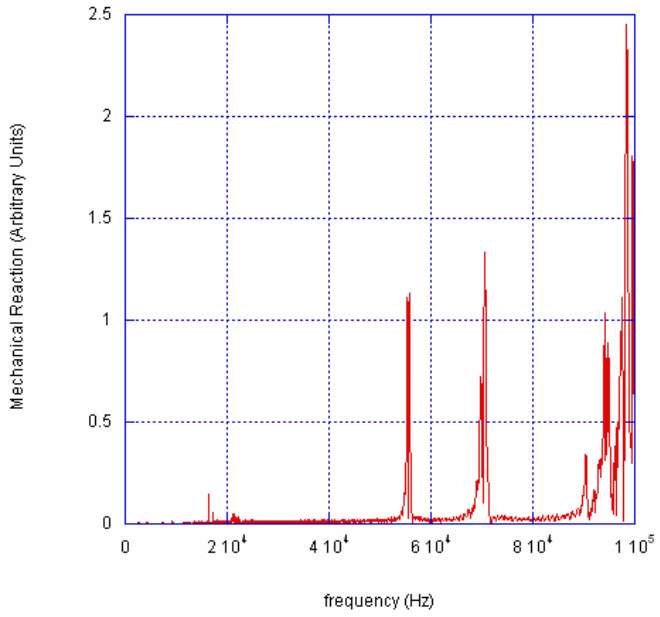

Figure 3-9 Measured vibrational spectrum of the improved STM head

3.3.2 Ambient Vibrational Spectrum

Using the ADC in the imaging computer, which digitizes the voltage signal from the tunneling current pre-amp into 12-bit data, an FFT of the tunneling current can be taken using a carefully prepared tip and sample. The pre-amp has a cut-off frequency of 5 kHz, and is a low pass filter. Frequencies above 5 kHz will therefore be attenuated. The FFT is calculated digitally using the RHK control software [56]. Any noise from vibrations can be observed as peaks in the FFT spectrum. The frequencies at which the peaks occur are indicative of the noise level in the STM head and not the properties of the tip-sample junction. Although the magnitudes of these peaks have a more complex relationship with the tunneling junction, the peak height is still related to the magnitude of the mechanical resonance. This FFT is essentially a measurement of the tunneling

power spectrum, which is influenced by mechanical vibrations. These FFT measurements were taken by Pouya Maraghechi on the prototype and the new STM head and a comparison can be made, as shown in Figure 3-10.

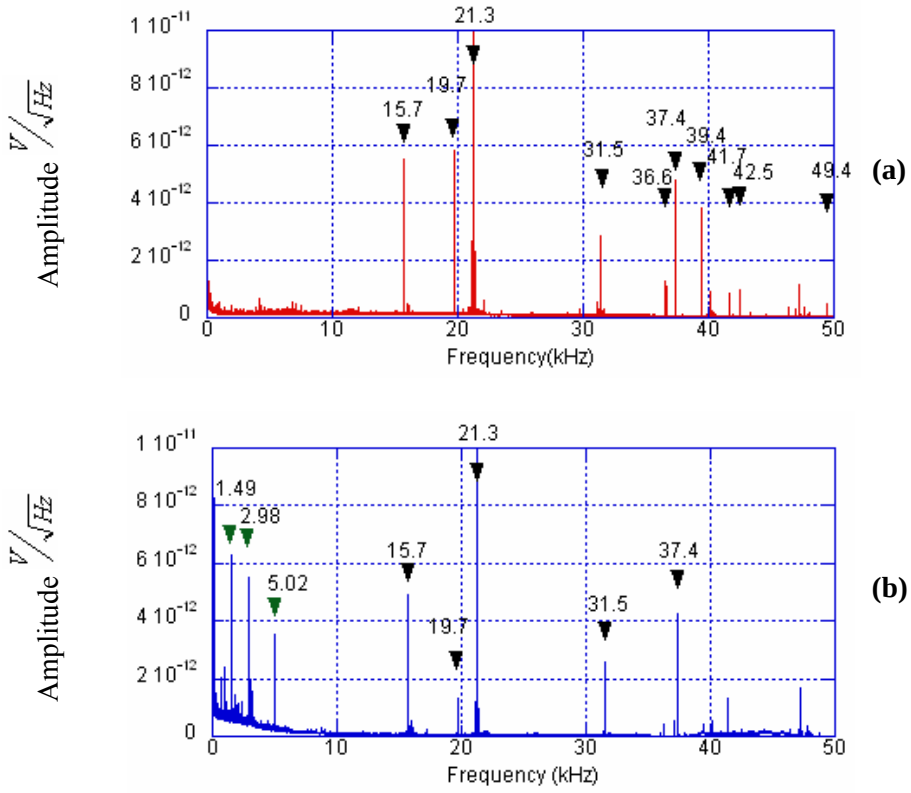

Figure 3-10 A Noise Spectrum (FFT) of the improved (a) and prototype (b) improved STM head. This includes a pre-amp gain of 10^8 V/A.

The low frequency resonances, which were a problem in the prototype STM head, are not present in the new design. There are new high frequency resonances observed at 36.6, 41.7, 42.5, and 49.4 kHz. The source of the non-shifting resonances at 15.7, 19.7, 21.3, 31.5, and 37.4 kHz is not exactly known. Possible sources are the ion gauge or other components in the UHV chamber. Figure 3-11 shows a closer zoom of the change in the resonances where it is important for STM operation.

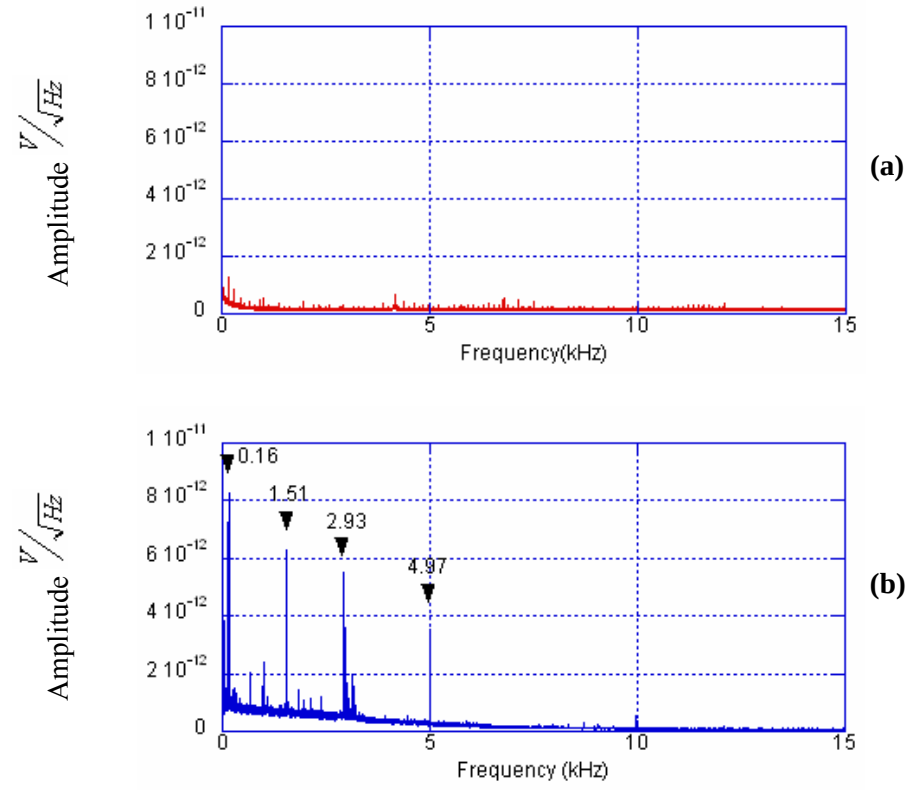

Figure 3-11 Tunneling current FFT comparison for 0 to 15 kHz for the improved (a), and prototype (b) STM heads

It is clear from Figure 3-11 that resonances in the frequency range of the feedback bandwidth have been successfully eliminated. The resonances at 0.16, 1.51, 2.93, and 4.97 kHz are gone from the new FFT spectrum. The FFT spectrum undeniably shows the improvement of the STM head over the prototype. This improvement can be seen in the images produced.

3.4 Comparison in Topography Images

The most obvious comparison to make is the visible difference in the quality of images achieved with the STM heads. An example of an STM image from the prototype STM head is shown

in Figure 3-12. There is no image processing done to the following images, the images are raw experimental data.

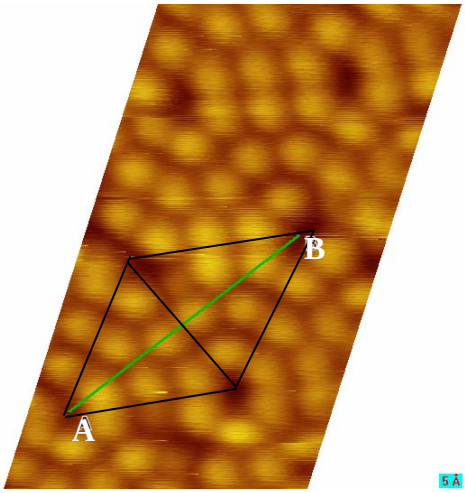

Figure 3-12 Raw topographic STM image at +1.5 V sample bias taken with prototype STM head

This is the cleanest image acquired with the prototype STM head. The cross-section AB is shown in Figure 3-13.

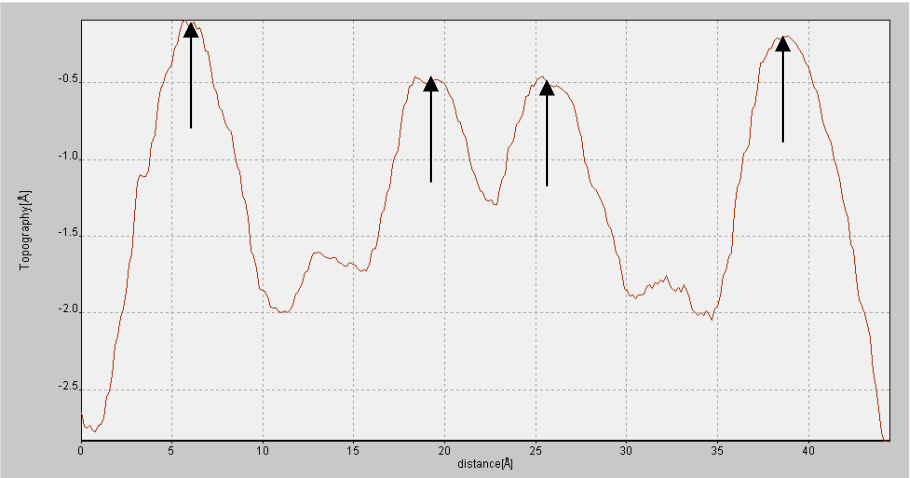

Figure 3-13 Cross-section of the topographic image from Figure 3-12

Note that, the average height will read zero ångströms due to the software subtraction in the STM controller. The four prominent peaks marked with arrows in Figure 3-13 are due to the adatoms indicated in Figure 3-12. The two larger peaks correspond to the corner adatoms and the two smaller peaks in the center correspond to the center adatoms. Between the corner adatom peaks and the center adatom peaks are two small peaks which correspond to the shoulders of the neighboring center adatoms. In practice, the quality of the STM tip is directly related to the shape of these smaller peaks. The higher the resolution achievable with a tip, the sharper these peaks will appear. However, the quality of the tip does not affect the high spatial frequency ripple that appears in the plot, which is due to electrical and vibrational noise in the STM apparatus.

To get an approximate level of noise in this image, a fourth order polynomial fit is made over a small top section of an adatom. A fourth order polynomial fit is used in this case as a common tool that can be consistently applied to any image as a metric for comparison. The polynomial was chosen to be fourth order so that the fit would follow the detail in the adatom shape, a peak which is concave downwards, but not the high frequency noise on the peak. If the order of polynomial is too high, then

the noise will influence the fit, leading to an artificially lower level of measured noise. If the order of polynomial is too low, then the shape of the peak will not be correctly fit. After experimenting with a second order fit, the shape of the fit did not closely follow the overall peak shape. Subsequently, a fourth order polynomial fit was found to adequately meet the criteria of fitting the shape of the peak, and not the noise in the peak. The difference between the fit and the data is taken, from which the RMS value of the noise in the image is extracted. The RMS noise in image Figure 3-12 is calculated to be about 7 pm.

The quality of the STM images of the new head is shown below in Figure 3-14. The noise in the image is visible, but does not distract from the overall image resolution. The noise in Figure 3-14 is mainly vibration noise. To get a better view of the noise level in the image, a cross-section labeled AB in Figure 3-14 is made and plotted in Figure 3-15.

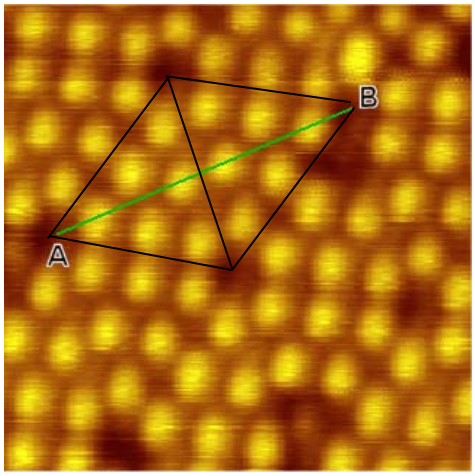

Figure 3-14 Raw topographic STM image at +1.5 V sample bias and 100 pA current. A cross-section AB is shown.

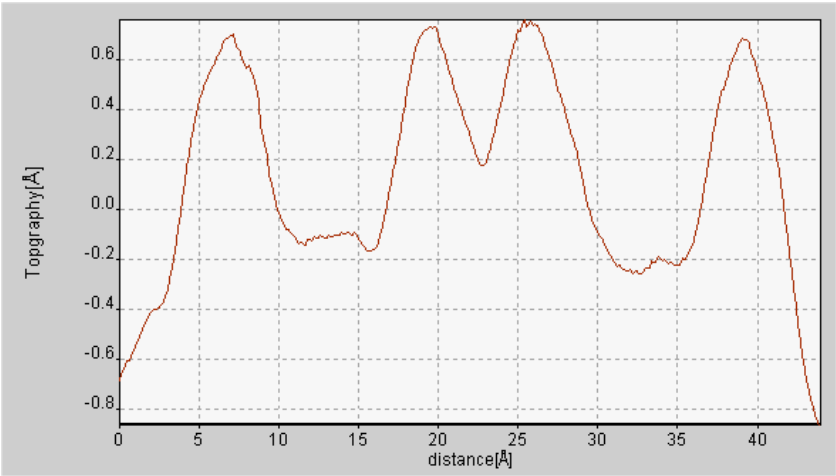

Figure 3-15 Cross-section of the topographic STM image from Figure 3-14

The noise in Figure 3-15 is representative of the levels of the noise that are generally present in STM images with the new head. The RMS noise is calculated to be 0.78 pm. This means that the STM head can image with 10 times less noise in the image compared to the prototype head. This is a major improvement.

3.5 Summary

The considerations for designing an STM head with superior vibrational properties were discussed. The resonant frequency of the DHO should be designed to be as low as possible, and the resonant frequency of the head should be as high as possible. The increase in performance from making these changes was analyzed by observing differences in the noise spectrum and the images of the new head.

Several peaks in the range of 1 to 10 kHz were successfully eliminated in the new design. The resonant frequencies in the head were successfully pushed to higher values, reducing the effect of

vibrations in the imaging. The vibrational noise in the images was measured to have fallen by a factor of 10 as compared to the prototype system.

Chapter 4
Thermal Drift Compensation

4.1 The Importance of Thermal Drift Compensation

The ambient temperature of the room that the STM is kept in is not well maintained, and there are fluctuations of several degrees during the day. As the STM temperature varies in time, the thermal expansion of its components will lead to drift in the relative positions of the sample's surface and the end of the tip. This thermal drift is categorized into vertical drift (in the distance between tip and sample) and the kind of drift that involves a meandering of the tip parallel to the sample surface i.e. lateral drift.

Lateral drift is a problem if one wants to observe the same distinct feature on the surface repeatedly. The scanning area of the microscope is often very small, and one does not want the point of interest to drift out of range. To minimize the thermal drift in the lateral direction, one should adopt a design of an STM head that is highly symmetric. The STM head used here contains components with high cylindrical symmetry and when the cylindrical symmetry is not available then three-fold (tripod) symmetry exists. This symmetry means that a uniform increase in temperature of the entire STM head will not lead to lateral drift. This is true regardless of the construction materials, as long as the tunnel junction is kept on the symmetry axis. Also, any thermal gradient along the symmetry axis will not result in lateral drift as long as all components, such as the scan tube, are centered and mounted square.

Vertical drift is typically well-compensated for through the use of the feedback system already in place to maintain a constant tunneling current. As long the total vertical drift does not

exceed the maximum range of the scan tube (several hundred nanometers) then it does not result in severe problems during regular operation. However for specialized techniques that require intermittent switching off of the feedback loop, such as tunneling point spectroscopy, then even small levels of vertical drift need to be dealt with. Also, vertical drift can couple into lateral motion whenever the tunnel junction happens to be located off the symmetry axis, or if the piezo tubes are not mounted perfectly square. In any case it is always a good idea to try to limit the amount of vertical drift by including thermal drift compensation into the design of the STM head. In fact, in this work, the level of overall thermal drift will be quantified only by looking at lateral drift.

If the entire STM head was made of just one material then a uniform increase in temperature of the entire STM head will not lead to any measurable vertical drift. Unfortunately the STM needs to constructed of various materials, each with different expansion rates. For example it is very likely that the sample support structure will expand at a different rate than the tip support structure, unless drift compensation is specifically designed into the system. If the compensation is properly modeled than vertical drift can be almost eliminated, at least for thermal gradients along the symmetry axis of the head, and at one particular temperature. The design of this compensation is the main focus of this chapter.

4.1.1 Tip Expansion Relative to Base

To start the calculations for the thermal compensation, let's look at the expansion of the STM tip. The common point to both the tip and sample is the STM base plate. The expansion of the tip is the contributed expansions of the scan tube, tip pedestal, tip holder base, tip holder tube, and the tip.

The thermal expansion of each component obeys the relation for linear thermal expansion

$$\frac{\Delta L}{\Delta T} = \alpha_0(T) \cdot L_0 \qquad (4\text{-}1)$$

Where α_0 is the coefficient for linear thermal expansion which is a function of temperature. The scan piezoelectric tube sits on the thermally compensating material, and the tip pedestal is atop the piezoelectric tube. These components are all epoxied together so the tip support behaves like a "fixed-free" type structure. The stainless steel tube is held in the tip holder base by friction. For small thermal gradients, one can assume for calculations that the stainless tube is fixed tight at the upper most part of the tip holder base. The tungsten tip is held in the stainless tube by friction as well. The tube is slightly oversized and the tungsten tip is bent so it fits tight in the tube. The strongest point of contact is the upper most point on the stainless tube, shown in Figure 4-1.

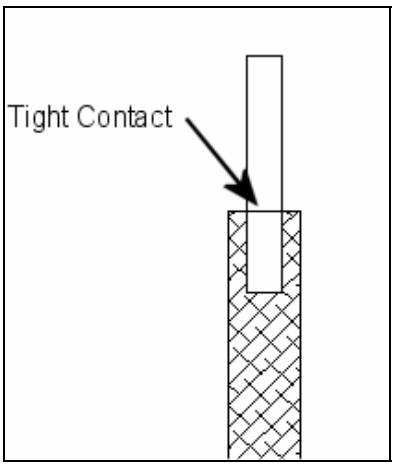

Figure 4-1 Tip mounting contact point

When two different materials are connected in these ways, and one end is held fixed while the other is free to expand, the total rate of expansion at the free end is found by simply adding up the two rates of expansion.

$$\alpha_{total} = \alpha_1 + \alpha_2 + \cdots + \alpha_n \ \left(\mathrm{K}^{-1}\right) \qquad (4\text{-}2)$$

For the tip structure, to find the rate of expansion of the end of the tip, the expansion rates of each of the components are simply added up. The sum of the expansion rates for the tip is 5.84×10^{-6}/K.

4.1.2 Sample Holder Expansion

Calculating the expansion of the sample holder, shown in Figure 4-2, is more challenging because of its more complicated construction. The sample holder itself is not symmetric laterally or vertically. Additionally, the two halves of the sample holder are different to accommodate the ohmic heating capabilities.

The important part of this calculation is to calculate the rate of expansion between the top of the sample holder base and the bottom of the sample. This is a little bit complicated because the sample is clamped between tantalum and ceramic supports. The mechanical properties of the clamping must be considered because as thermal expansion occurs, the clamping will be compressed depending on the material's Young's Modulus.

Considering the mechanical properties, there will be a few more calculations for the expansion of the sample holder. The series of parts 16-22 (sample assembly) will expand at a certain rate. The parts 17,18,19,21, and 22 are sandwiched between the sample holder base (part 6) and the molybdenum nut (part 20). See Figure 4-3 for a closer view of the sample clamping.

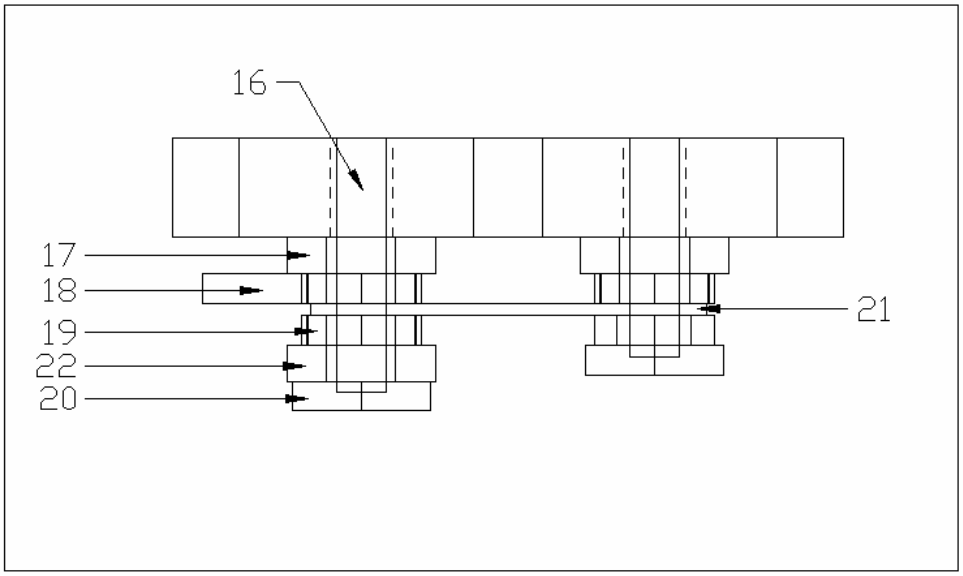

Figure 4-2 Sample holder side view

Table 4-1 Labels for Figure 4-2

Number	Part	Material	Length / Thickness
16	0-80 Threaded Rod	Molybdenum	5.08 mm (0.20”)
17	Hat Washer	Ceramic	0.914 mm (0.036”)
18	Conductive Tab for Heating	Tantalum	0.762 mm (0.03”)
19	Conductive Tab for Clamping	Tantalum	0.762 mm (0.03”)
20	Hexagonal 0-80 Nut	Molybdenum	1.27 mm (0.05”)
21	Sample	Silicon	~0.33 mm (0.013”)
22	Hat Washer	Ceramic	0.914 mm (0.036”)

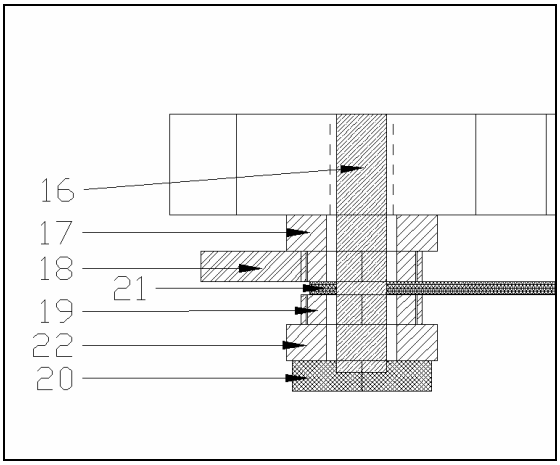

Figure 4-3 Sample clamping on the left side of the sample holder

Tension in the rod (part 16) holds back the expansion and is stretched while the parts 17, 18, 19, 21, 22 expand and push against the nut (part 20) stretching the rod (part 16). In order to describe the physics of this, the elastic properties of the materials must also be known.

Table 4-2 Young's modulus of the materials used in the sample holder construction

Number	Material	Young's Modulus
16	Molybdenum	329 GPa
17	Ceramic	373 GPa
18	Tantalum	186 GPa
19	Tantalum	186 GPa
20	Molybdenum	329 GPa
21	Silicon	47 GPa
22	Ceramic	373 GPa

To find the different rates of expansion for the molybdenum rod (part 16) and the assembly (part 12), one takes a thickness weighted average of the coefficients of thermal expansions for the assembly to arrive at an effective coefficient of thermal expansion.

$$\begin{aligned}\alpha_{assembly} &= \alpha_{17}\cdot\left(\frac{L_{17}}{L_T}\right)+\alpha_{18}\cdot\left(\frac{L_{18}}{L_T}\right)+\alpha_{21}\cdot\left(\frac{L_{21}}{L_T}\right)+\alpha_{19}\cdot\left(\frac{L_{19}}{L_T}\right)+\alpha_{22}\cdot\left(\frac{L_{22}}{L_T}\right)\\ &= 7.5\cdot\frac{0.036}{0.145}+6.3\cdot\frac{0.03}{0.145}+2.6\cdot\frac{0.013}{0.145}+6.3\cdot\frac{0.03}{0.145}+7.5\cdot\frac{0.036}{0.145}\end{aligned} \qquad (4\text{-}3)$$

The resulting effective coefficient of thermal expansion is: 6.56×10^{-6}/K. The rate of expansion of the rod is 4.8×10^{-6}/K. These different rates of expansion will cause stress in the sample holder as thermal gradients are applied. The actual motion of the sample can be calculated. One way is to think of the compressibility of the materials as a spring constant. The motion will be somewhat absorbed in the compression of the assembly and tension on the rod. A simple way to illustrate this is given in Figure 4-4.

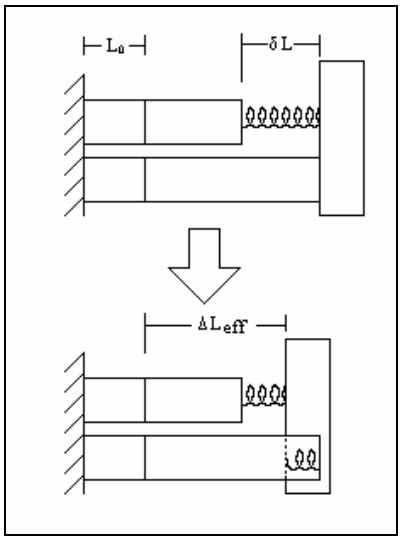

Figure 4-4 Illustrating the effect of varied thermal expansion coefficients

The initial length of the two rods is L_0 and they are both secured against a surface on the left side. The two rods then expand to be lengths different by δL. Since the two rods are connected on the end, one of them will have to stretch from tension (upper rod) and the other will compress (lower rod). The spring constant is obtained from Young's modulus.

$$k = \frac{Y \cdot S}{L} \left(N/m \right) \qquad (4\text{-}4)$$

Where Y is Young's modulus and S is the cross sectional area. The forces are given by:

$$F = k \cdot dL \qquad (4\text{-}5)$$

The cross sectional areas of contact for the parts are shown in Table 2-8.

Table 4-3 Sample holder assembly cross sections

Number	Material	Cross section (sq. in)	Other information
16	Molybdenum	0.002	1.27 mm (0.05") Diameter
17	Ceramic	0.0138	3.81 mm (0.15") OD, 1.778 mm (0.07") ID
18	Tantalum	0.014	
19	Tantalum	0.01	
21	Silicon	0.0063	2.286 mm (0.09") by 1.778 mm (0.07") contact
22	Ceramic	0.0138	3.81 mm (0.15") OD, 1.778 mm (0.07") ID

The spring constant from (4-4) of the molybdenum rod is 1.15×10^8 N/m. Finding the spring constant for the sample assembly is done by continuing with the spring analogy. The assembly can be thought of as a network of springs connected in series. The summation rule for the spring constant is:

$$\frac{1}{k_{assembly}} = \frac{1}{k_{17}} + \frac{1}{k_{18}} + \frac{1}{k_{19}} + \frac{1}{k_{21}} + \frac{1}{k_{22}}, \qquad (4\text{-}6)$$

and the result is 3.14×10^8 N/m for the spring constant of the assembly.

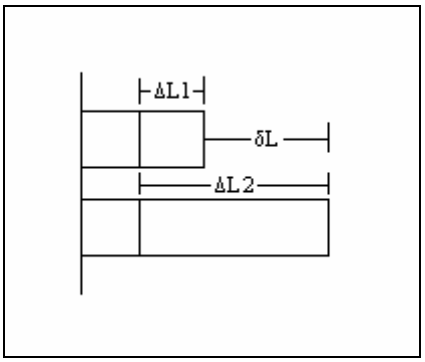

Figure 4-5 Expansion of thermal compensators

where $\Delta L_1 = \alpha_{16} \cdot L_0$, $\Delta L_2 = \alpha_{assembly} \cdot L_0$, and $\delta L = \Delta L_2 - \Delta L_1 = \left(\alpha_{assembly} - \alpha_{16}\right) \cdot L_0$.

When the net force is zero, the two materials are stretched and compressed a certain amount dL causing a force as shown in Figure 4-5.

$$\begin{aligned} \Delta L_{eff} &= \Delta L_1 + dL &&= \alpha_{16} \cdot L_0 + dL \\ \Delta L_{eff} &= \Delta L_2 - dL &&= \alpha_{assembly} \cdot L_0 - dL \end{aligned} \qquad (4\text{-}7)$$

Equating the forces gives the expression:

$$k_{16} \cdot \left(\Delta L_{eff} - \alpha_{16} \cdot L_0\right) = -k_{assembly} \cdot \left(\Delta L_{eff} - \alpha_{assembly} \cdot L_0\right); \qquad (4\text{-}8)$$

and if

$$\Delta L_{eff} = \alpha_{eff} \cdot L_0, \qquad (4\text{-}9)$$

then the effective coefficient of expansion can be solved for which is:

$$\alpha_{eff} = \frac{k_{16} \cdot \alpha_{16} + k_{assembly} \cdot \alpha_{assembly}}{k_{16} + k_{assembly}}. \qquad (4\text{-}10)$$

Performing the calculation gives an effective coefficient of expansion of 6.09×10^{-6}/K. Next, the coefficient of constraint is defined as:

$$\beta = \frac{\alpha_{eff}}{\alpha_{assembly}}, \qquad (4\text{-}11)$$

which is equal to 0.93. Now, the same calculations have to be performed on the other side of the sample holder because it is not symmetrical.

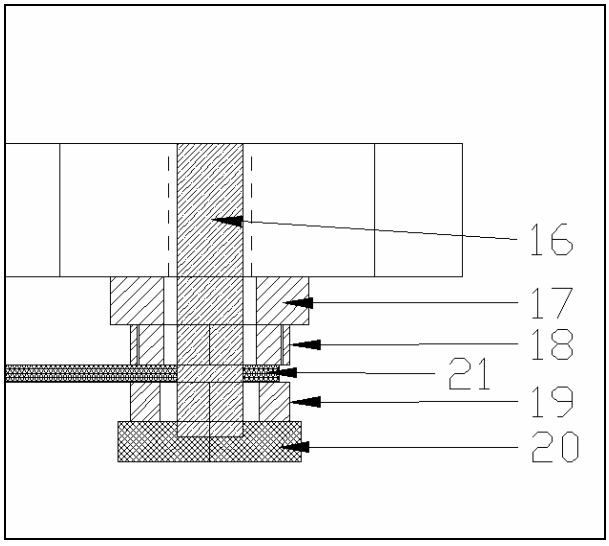

Figure 4-6 Diagram of right side of sample holder

For this side of the sample holder, the effective coefficient of expansion is 5.89×10^{-6}/K, slightly less than the side with the extra hat washer (part 22). The coefficient of constraint is 0.94. To get a good approximation of the coefficient of thermal expansion of the assembly, an average of the rates of expansion of the two sides will be sufficient. The rate of expansion of the assembly is 5.99×10^{-6}/K, The rate of expansion of the bottom of the sample can be found using the coefficient

of constraint. The average coefficient of constraint is 0.935. The effective coefficient of thermal expansion for parts 17, 18, and 21 is 6.24×10^{-6} /K. It is, however constrained by the molybdenum rod and the rate of expansion is 0.935 times that value. The rate of expansion of the bottom of the sample is 5.83×10^{-6} /K.

4.1.3 Expansion of the Sample Relative to Base

As was done for the tip, the rate of expansion of the bottom of the sample with respect to the STM base can be calculated. The parts that contribute to the sample expanding away from the tip are: the coarse approach piezo (part 1), coarse piezo lid (part 2), sapphire balls (part 3), coarse approach ring (part 4) and the sample supports (part 5). The sample holder clamping (part 12) actually causes the sample to expand towards the tip. Note that the position of the coarse approach will be slightly different for each experiment. To determine the effective thickness of the coarse approach ring (part 4) it assumed that the coarse approach is half way through its full range. That is, the ring is 0.3556 mm (0.014") thinner.

$$\frac{\Delta L}{\Delta T} = (\alpha_1 \cdot L_1) + (\alpha_2 \cdot L_2) + (\alpha_3 \cdot L_3) + (\alpha_4 \cdot L_4) + (\alpha_5 \cdot L_5) - (\alpha_{12} \cdot L_{12}) \qquad (4\text{-}12)$$

resulting in a rate of expansion of 10.27×10^{-6} /K. This is much larger than the expansion of the tip and now, the two rates must be made the same by the addition of one material of a specific geometry to compensate.

4.1.4 Compensating Material

Now that the rates of expansion of the tip and sample (5.84×10^{-6} /K and 10.27×10^{-6} /K respectively) are known, the two must be made the same, or at least, one must minimize the difference. Note that the exact thermal expansion coefficient for the piezoelectric tubes is not known.

This is not a problem because there is 0.25” (6.35 mm) of piezo material underneath both the sample and tip. This means that the thermal expansion contribution from the piezoelectric material is the same for both the sample and tip. Simply put: the difference from the piezoelectric tubes for the sample and tip is zero and there is no contribution to thermal drift.

To find the amount of material needed to properly compensate expansion, one must note that in the design, the bottom of the scan tube sits 0.2” (5.08 mm) above the bottom of the coarse approach piezoelectric tubes. First off, it is noted that the material under the scan tube is 0.2” (5.08 mm) longer than the material under the approach tubes. This is demonstrated in Figure 4-7.

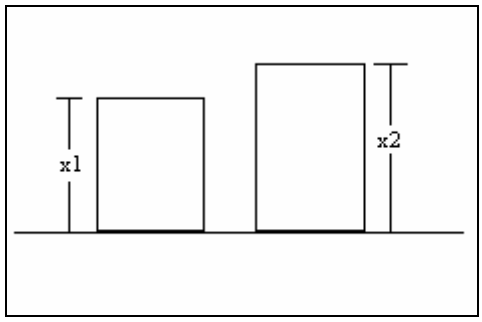

Figure 4-7 Tip and sample expansion compensators

Also, the tip is needed to expand more, and the sample to expand less. The most commonly available material with a large coefficient of thermal expansion is copper with 16.5×10^{-6}/K. The most commonly available material with a small coefficient of thermal expansion is molybdenum with 4.8×10^{-6}/K. Molybdenum was chosen as the material for an extra component that was placed under the sample and copper under the tip. To calculate the amounts needed, the two expansions are equated:

$$x_2 = x_1 + 0.2"(5.08\,\text{mm})$$

$$rate_{sample} - rate_{tip} = \alpha_{Cu} \cdot x_2 - \alpha_{Mo} \cdot x_1 = \alpha_{Al} \cdot \left(x_1 + 2.0"\,(5.08\,\text{mm})\right) - \alpha_{Mo} \cdot x_1$$

$$4.43"\,(112.5\,\text{mm}) = 16.5"\,(419.1\,\text{mm}) \cdot \left(x_1 + 0.2"\,(5.08\,\text{mm})\right) - 4.8"\,(121.9\,\text{mm}) \cdot x_1$$

solving for x_1, it is found that $x_1 = 0.096$" (2.44 mm).

In conclusion, to thermally compensate the sample and tip, 0.096" (2.44 mm) of molybdenum is needed under the approach tubes and 0.2" (5.08 mm) of copper under the scan tube. The addition of these materials will minimize the vertical drift between the sample and tip gap.

4.2 Thermal Drift Results

The improvement in thermal drift is difficult to quantify precisely as the amount of thermal drift varies from session to session. Nevertheless, by waiting about an hour or two after the initial coarse approach, the system has a tendency to settle down to a characteristic drift rate, and these are the drift rates compared here.

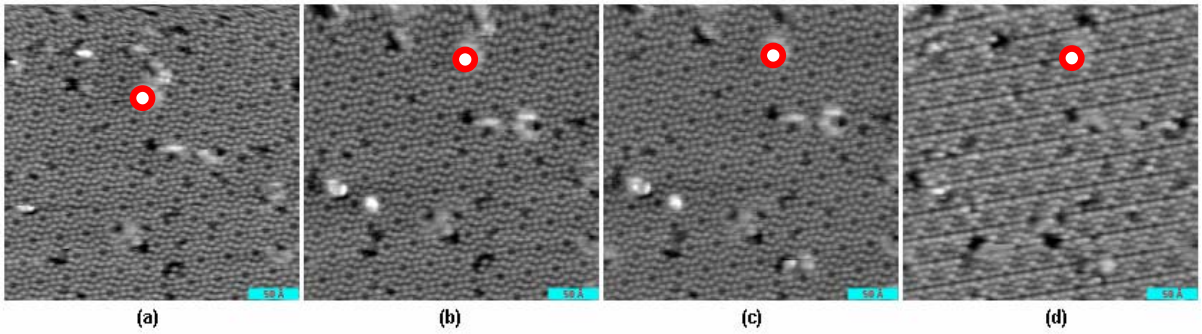

Figure 4-8 Consecutive scans of the same surface area (a) to (c) at +2.0V, and (d) at -0.7V Between consecutive images 8.5 minutes of time elapsed.

Figure 4-8 (a) was the first scan in this area and there is a lot of piezo drift present in the form of creep, which is not a thermal effect. These images were not shifted and the amount of thermal drift is visible. Between (b), (c), and (d), the amount of thermal drift is on average 0.5 Å/minute. This is a

very low amount of drift which demonstrates what the STM head is capable of at room temperature. The prototype STM head had a thermal drift of approximately 20 Å/minute. The thermal drift properties of the STM head is a factor of ~ 40 better than the prototype head.

4.3 Comparison in Spectroscopic Images

Spectroscopic imaging will be discussed in detail in Chapter 6. This section will demonstrate the effect of vibrations on these images. In order to produce nice clean spectroscopic STM images, the noise in the signal must be small. The nature of spectroscopic imaging makes the technique sensitive to noise as will be discussed later. Here, a comparison is made between typical spectroscopic images with the prototype STM head and the new STM head. For the spectroscopic measurements to be considered valid, the forward and back scans should generally look the same (features should be identifiable in both the forward and back scan). This helps to solidify the data against strange tip effects or drift effects. To take high resolution spectroscopic images, the scan speed has to be somewhat lower than for topographic images. If there is too much thermal drift, then the images will become distorted and cause problems for the spectroscopic imaging, especially if consecutive scans are required of the same area.

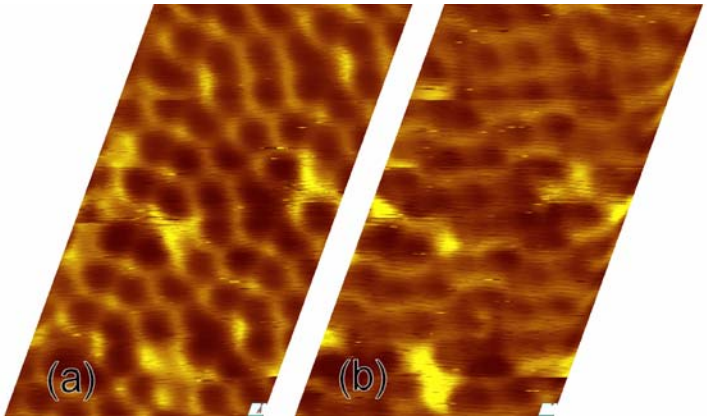

Figure 4-9 Front and back scan of a dI/dV image with the prototype STM head taken at +1.5V (a) front scan (b) back scan

In Figure 4-9, the front and back scans look similar, but there are obvious differences. Figure 4-9 is an example of two spectroscopic images that look very different due to the thermal drift in the STM head.

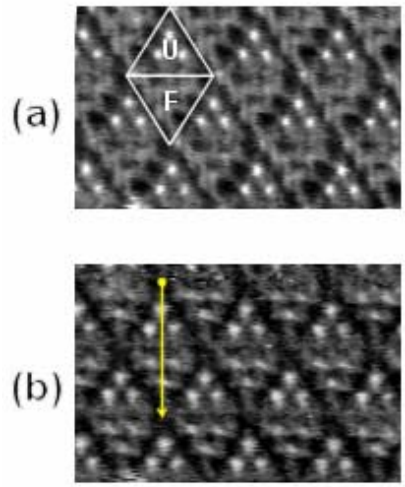

Figure 4-10 Front and back scan of a dI/dV image with the new STM head taken at -0.8V (a) front scan (b) back scan

For the new STM head, the similarity between the front and back scans, as shown in Figure 4-10, is much better. Although it's not a perfect match, it is still good: bright and dark features can be correlated between the two scans, the geometry in the two scans is the same, and the resolution of the two images is of the same magnitude.

4.4 Summary

The thermal expansion of the STM head was analyzed. By matching the rate of thermal expansion of the sample and tip at the tunneling junction, the effects of thermal drift were reduced. The lateral thermal drift performance at room temperature was measured to be as low as 0.5 Å/minute, a very impressive value at room temperature. This capability is very useful for

experiments requiring repeated scanning of distinct features on a surface. The reduced amount of thermal drift also results in improved spectroscopic imaging, shown by a strong correlation in the features of front and back scanned images.

Chapter 5
The UHV STM System

This chapter will first describe the equipment used at the surface physics lab at the University of Lethbridge related to the STM experiments. The STM apparatus is shown in Figure 5-1. For STM experiments on semiconductor surfaces, the oxide layers must be removed from both the surface and the tip. In both cases, these layers of oxide are removed through heating in UHV. This presents a challenge for the tip because the atomically sharp nature must be preserved. For the sample, the surface must be left atomically flat, ordered, and relatively free of defects. The technique used to prepare and clean tips and samples for STM will be discussed.

5.1 Equipment

The microscope is placed in an Ultra High Vacuum (UHV) chamber with a base pressure better than 3×10^{-11} torr. A 300 L/s[1] Varian Ionization Pump model VacIon Plus 300 and two Titanium Sublimation Pumps (TSPs) are used to achieve UHV. STM tips and samples are transferred into the chamber through a load-lock which is at high vacuum. A 60 L/s Varian turbo molecular pump model V 70D (MacroTorr) is used for the load-lock stage. This pump is not capable of UHV; however it reduces the pressure enough so that transfer of a sample, tip, or other component will not severely contaminate the main chamber. There are several stages of vibration isolation throughout the apparatus. Notably, the entire UHV chamber is placed on a vibration isolation table which is on a sandbox. Then, the microscope is suspended by springs which have a low resonant frequency in UHV and damped magnetically along three axes plus rotation with six rare earth SmCo magnets.

5.1.1 Vacuum and UHV Chamber

The STM is placed in UHV to prevent the oxidization of the samples and to ensure a clean surface to study. The microscope is operated in vacuum with a base chamber pressure measured with a nude ion gauge to be between 3×10^{-11} torr and 6×10^{-11} torr. The pressure in the chamber changes slightly day to day because it depends on many things such as the ambient temperature of the room and cleanliness of the chamber. The pressure is the lowest right after a bake. These changes in temperature are the cause of a more important problem in STM experiments. The small pressure changes are trivial, but the change in temperature causes thermal expansion of the materials resulting in imaging problems such as thermal drift.

The vacuum is obtained in stages. First, as much air as possible is evacuated using the Varian turbo molecular pump backed by a mechanical roughing pump. This brings our chamber pressure into the 1×10^{-7} torr region which is still too high for STM imaging. At this point however, the atmosphere in the chamber is no longer in the turbulent flow regime, but is now in the molecular flow regime. The individual atoms and molecules in the gas no longer interact strongly with each other. Once the pressure is at this stage, the ion pump is turned on and the chamber is sealed from the turbo pump. Titanium sorbant in the ion pump is used to react with the remaining gases, which causes them to stick inside of the ion pump. The ion pump actively pumps the gas into the sorbant causing this process to happen very efficiently.

---

[1] L/s is liters per second. This refers to the volume of gas (nitrogen) that would be pumped at atmospheric pressure. It should be noted that the pump can only operate at low pressures.

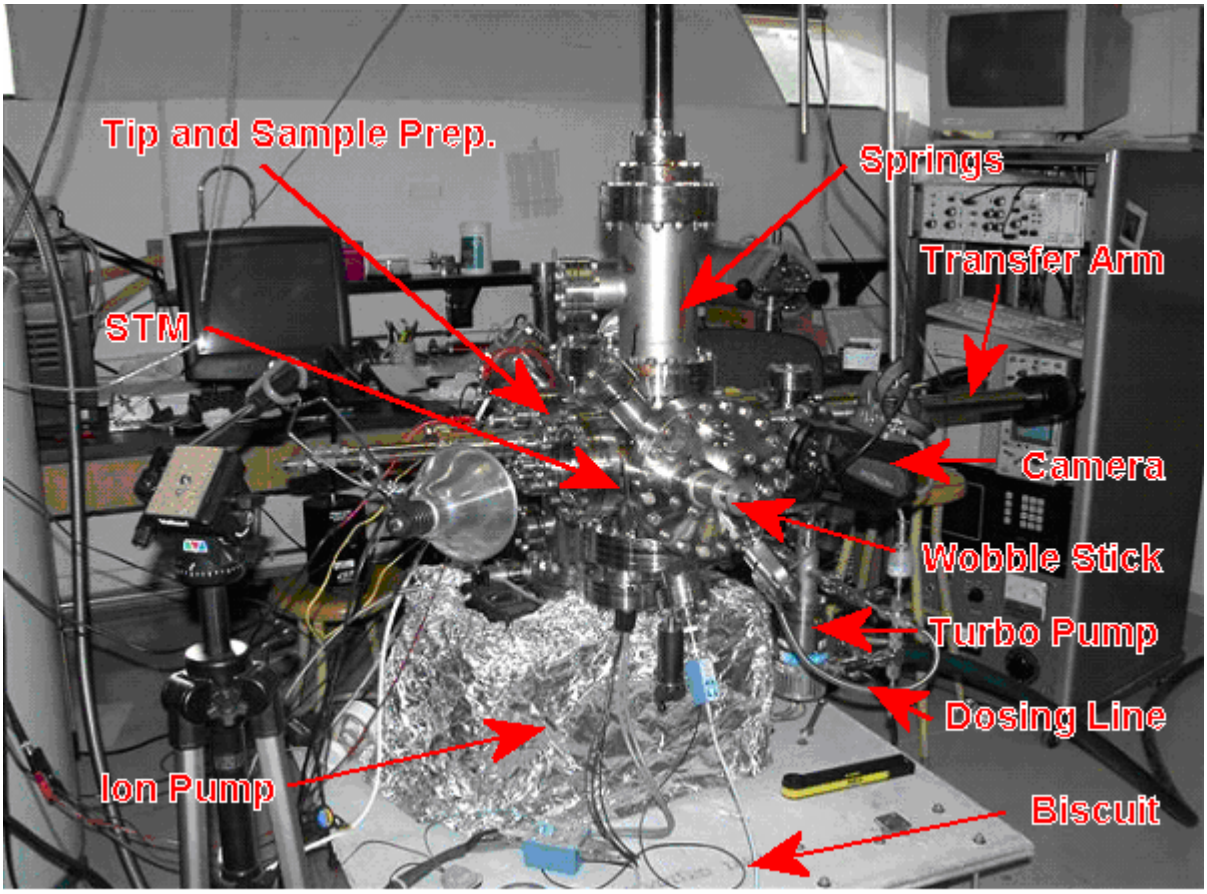

Figure 5-1 The UHV STM system at the University of Lethbridge in 2004

The concept of these ion sorption pumps is quite remarkable in the fact that nothing actually leaves the vacuum chamber, but is instead changed from a gas state to a solid state. The ion pump is aided by a titanium sublimation pump which coats a large surface of the inside chamber with a thin film of titanium. This highly reactive surface then acts as a getter removing additional molecules from the gas phase. The major benefit of a TSP is the enhanced ability to pump hydrogen, a very light and abundant gas at low pressures. The combination of a TSP and an ion pump makes a very effective team in which the ion pump can remove the non-reactive noble gases well and the getterable (gases that chemically react) gases are pumped in the TSP.

With this pumping, the pressure is brought down further to the 1×10^{-9} torr regime. At this point, if the pump is left running, one will have to wait a very long time for the pressure to fall any further. This is because there are many molecules adsorbed to the inner walls of the chamber that is still constantly outgassing. The gases released from the chamber wall consist of approximately 90% water [57]. Other major gases include nitrogen, propane, methane, and oxygen [58]. It is important to note that all of the pumps used are completely free of grease or oil. These heavy compounds would outgas and their heavy weight makes them difficult to remove. Using pumps without these lubricants means that the chamber does not become contaminated. In fact, the inside of the stainless steel chamber is always very clean. It is degreased chemically to remove any heavy contaminants before being used for vacuum. To get the pressure even lower yet, the entire chamber is heated to approximately 150˚C for one to two days to boil off anything that outgases off the walls. The bake-out temperature is limited by the curie temperature of the piezoelectric tubes. After this treatment, the chamber will cool down and reach a very low base pressure that is sometimes too low to be measured by our nude ionization gauge.

Nude ionization gauges use electrons to ionize atoms and molecules in the vacuum. The ionized molecules are inside an electric field and are drawn to an electrode generating a current. As the charges decelerate, X-Rays are generated. In addition to the current generated by the impinging ionized molecules, there is a current generated by these X-Rays striking the electrode. The ionization gauge lower limit is when the current caused by the generated X-Rays is of the same order as the current caused by ionized atoms/molecules. This limit is about $3x10^{-11}$ torr [57].

5.1.2 Sample and Tip Preparation Stage

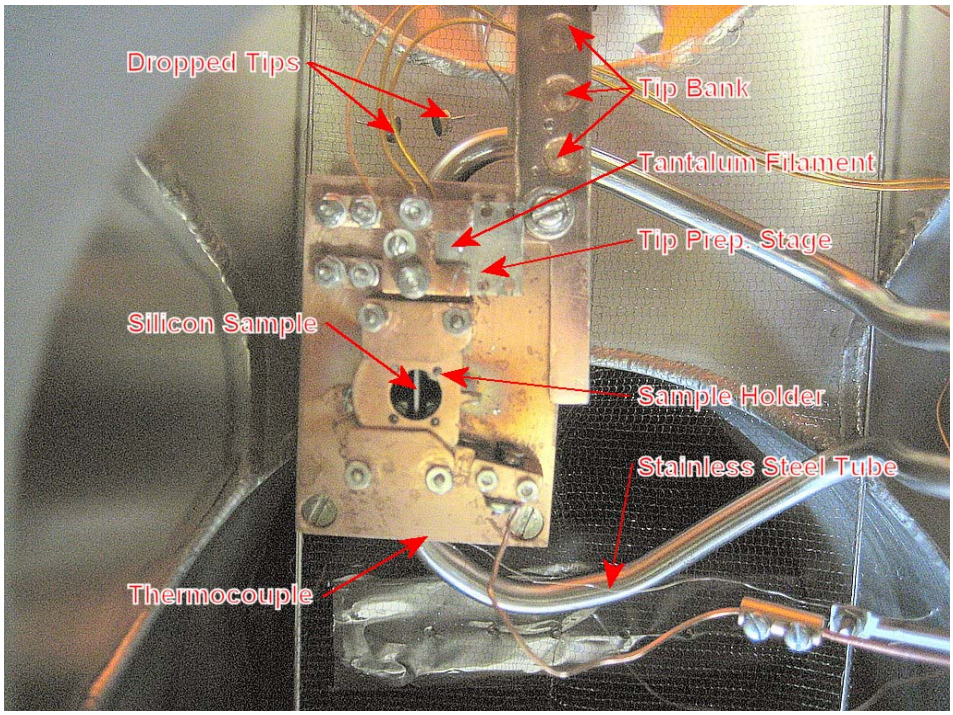

Figure 5-2 Photograph of sample and tip preparation stage

Before a surface can be studied by STM, it must be cleaned and prepared. Although some of this process happens outside the vacuum chamber, not all of it can be done outside. When investigating silicon surfaces with STM, the oxides and contaminants must be removed. This cleaning process takes place inside the vacuum using a sample and tip preparation stage shown in Figure 5-2. This stage is located in the main chamber beside the microscope and is used before the sample is inserted into the microscope. The entire process is described in detail in sections 5.2 and 5.3.

The preparation stage consists of two main parts, a tip and sample component. The sample component is mainly a slot for a sample holder and it provides electrical connections to the sample

holder so that current can be passed through the sample for ohmic heating. The sample is connected to an Agilent 6654A power supply. The sample temperature is monitored using a Micron M90H pyrometer [59]. The tip portion positions the tip below a thin tantalum filament. Tantalum is used because it is more malleable than tungsten, our first choice. Tungsten filaments become brittle after successive heating and break if anything touches them. This is not true of tantalum which will simply bend and can later be reshaped. The wobble-stick transfer arm can damage the filament if the operator is not careful. The filament is used for the tip cleaning and characterization process which is described in detail in section 5.2.1.

5.1.3 The STM Controller

The STM system uses the RHK Technologies SPM1000 controller revision 8 [56]. This commercial controller uses a 12-bit ADC installed in a computer running windows 2000, in combination with their SPM32 software. The use of commercial control hardware greatly reduces the amount of time spent debugging, and the RHK system is still flexible enough to modify for specific experiments.

5.1.4 The Microscope Transfer Mechanism

The microscope receives a tip holder and sample holder. The tip and sample holder are transferred using a wobble-stick mechanism shown in Figure 5-3. The tip holder is shown in Figure 5-5 and the sample holder in Figure 5-6. Transfer and placement of the components inside the vacuum requires agility and practice, but is straight forward. The major advantage to a wobble-stick transfer system is the versatility and control. The design is very simple, consisting of clamping jaws to grasp the tip and sample holders. This makes debugging very simple for this system (i.e. repositioning the sample holder). Unfortunately, this added mobility places more responsibility on

the operator to prevent damage to the system. Also, there is an increased chance of dropping tips and samples from operator error.

The wobble stick consists of clamping jaws on a retractable bellows with a pivoted movement. The motion of the wobble stick is similar to locked oars in a rowboat. The clamping jaw on the end of the transfer arm allows the operator to move objects inside the UHV.

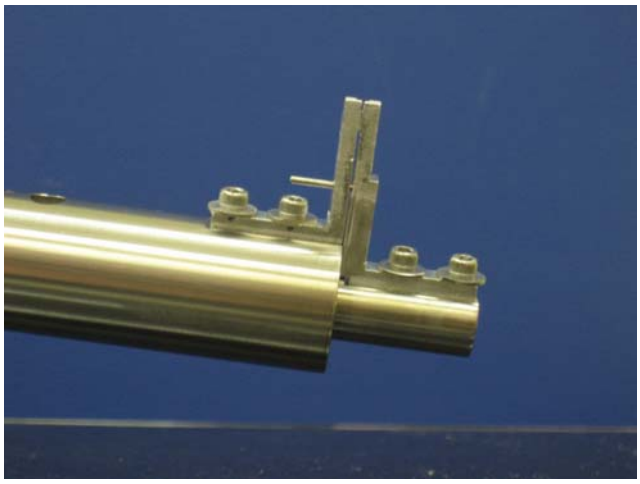

Figure 5-3 Photograph of wobble stick jaws

5.1.5 Gas Dosing Line

Besides studying clean surfaces, STM can be used to study adsorbates on surfaces, specifically to study chemistry on very small scales. To deposit a small coverage of molecules onto the surface, some additional equipment is required. The task of depositing specific adsorbates on the clean surface can be done many ways depending on the substance with which one wishes to dose. As long as the vapor pressure of the substance is significantly higher than our vacuum pressure, then one can simply deposit the material in the gas phase into the chamber and onto the reactive surface. When the sticking coefficient to the surface is defined to be greater than zero, this method works fine.

If the substance has a relatively low vapor pressure (high melting point), then it needs to be heated to cause it to evaporate onto the surface (i.e. gold). This heating effectively increases the vapor pressure of the material. Atomic species not found naturally can also be deposited using a hot filament to dissociate molecular species such as hydrogen [60].

For the studies in this thesis, small organic compounds with a high vapor pressure were deposited onto silicon. To accomplish this, a gas dosing system was used. Figure 5-4 shows a diagram of this system.

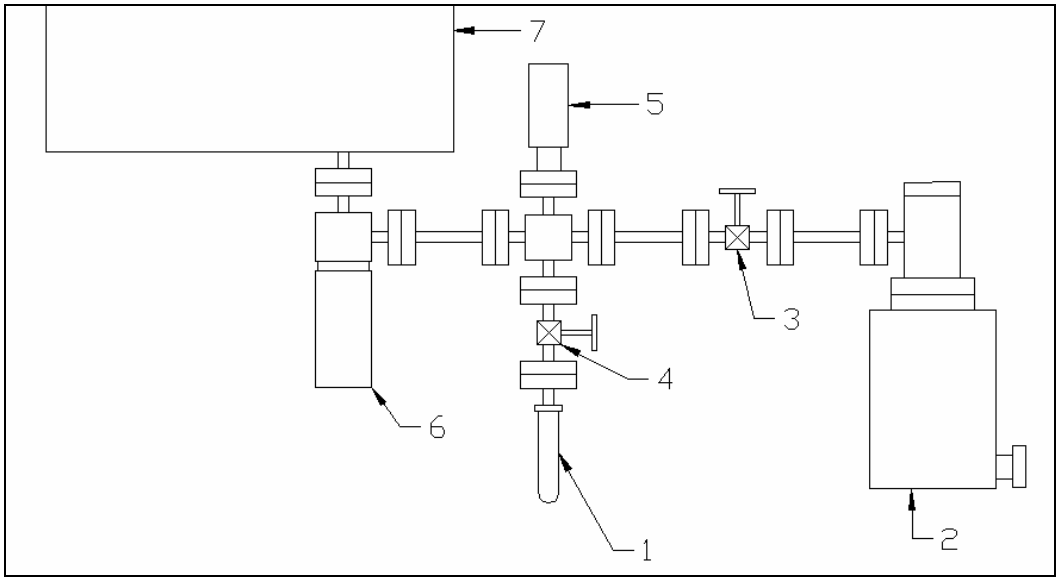

Figure 5-4 Gas dosing line

Once the dosant is loaded into the reservoir, it must be cleaned before being released into the vacuum chamber. Ultra-high purity products are purchased but there still remains some atmosphere and other minor contaminants in the reservoir and dose line that must be removed. First, the loading valve is left closed while the cleaning valve is open during pump-down. This pumps out the atmosphere in the gas line. At this point, a heat gun is used to bake water off the inside walls of the

gas line and remove other adsorbed contaminants faster. Next, the liquid sample can be cleaned. The technique used to remove these contaminants is the freeze-pump-thaw process. Assuming the liquid that will be dosed will freeze, the glass liquid reservoir is submersed in LN_2 and contents become a solid. The loading valve is then slowly opened and the atmosphere pumped out. Some N_2 in the reservoir will liquefy and not be pumped out. To remove it, the LN_2 bath is removed while the loading valve is left open. As the liquid slowly heats up, the top will evaporate off. Before too much dosant is lost, the loading valve is closed. A liquid-vapor equilibrium is established, and gasses such as N_2 and O_2 will boil away before the benzene. This procedure is repeated 2-3 times.

Table 5-1 List of components for Figure 5-4

Number	Part	Notes
1	Glass vial for liquid reservoir	Attached using ultra-torr fitting
2	Turbo pump	Used for both gas line and load-lock
3	Cleaning valve	Opened only to pump out gas line
4	Loading valve	Opened to release gas into line
5	Convectron gauge	Used to ensure vacuum in line
6	Precision leak valve	Leaks gas into chamber
7	Vacuum chamber	Leak valve aims gas at sample surface

An alternative to the freeze-pump-thaw is cleaning by dilution. The gas line is pumped out and the cleaning valve closed. Then the loading valve is opened and soon closed while gas has filled the dose line mixing with any contaminants. The gas line is then pumped out and the procedure repeated. Because the supply of dosant is much larger than the contaminants, the partial pressure of the contaminants will reduce with each repetition. Of course, the effectiveness depends on the nature of the contaminants (i.e. if the liquid is saturated with a gas).

Dosing the surface is a controlled procedure. The flux of molecules on the surface is easily calculated knowing the molecule and the pressure of that molecule. Using thermal statistics [61, 62], the flux on a surface is

$$\phi = \frac{1}{4}\frac{P}{kT}\bar{v} \quad \left(\text{molecules}/m^2 s\right). \qquad (5\text{-}1)$$

Here, P is the pressure and $\bar{v}$ is the mean velocity of the molecules. It is important to note that this formula accounts for the mass of the molecules in $\bar{v}$. From this rate of exposure, the coverage of the surface is simply given by measuring the time of exposure.

$$Coverage = \frac{\phi \cdot t \cdot S}{\eta} \text{ (dimensionless)}. \qquad (5\text{-}2)$$

S is the sticking coefficient of the surface to the incident molecules. It is a measure of the probability that a molecule hitting the surface will adsorb. η is the density of binding sites on the surface. The sticking coefficient depends on both the substance-surface interface (i.e. binding energies) and the temperature of the surface.

The dose delivered onto a sample is measured in the units of Langmuirs. One Langmuir is $10^{-6} torr \cdot s$. Giving the exposure in Langmuirs eliminates the calculation of dosing time and pressure and makes varying dosings easy to compare.

5.2 Preparing Tips and Samples for UHV

For a controlled study of the silicon surface, it is important that one minimizes or eliminates as many unknown elements as possible. For example, contaminants and disordered surface regions make the understanding of surfaces very difficult or impossible. To facilitate the study of this surface one must be able to consistently produce a clean and well structured surface. Only after this, can the

study of adsorbates and surface structure begin. The entire sample/tip process must be consistently reproduced. The STM relies on the constant ability to perform experiments. To use it as an observation tool, the microscope components should not influence the experiment.

5.2.1 Preparing STM Tips

STM tips are prepared from 0.381 mm (0.015") diameter tungsten wire by electrochemical etching. To form the tip, the wire was shielded with Teflon tubing except for a small slit which is exposed to the etching solution. This is where the etching will occur. The wire is then submerged in 5 M NaOH solution and a +6.25 V potential is applied to the wire. A stainless steel post submerged in the solution nearby serves as a cathode for the wire. The tungsten wire reacts to form tungsten oxide and slowly, the wire is etched thinner, whittling away until it is left supported by a very small piece. Eventually the wire breaks off and the end falls to the bottom of the beaker. It is important that there are not too many vibrations during this part as vibrations may cause the tip to break off too soon and leave a dull tip.

After the etching process, the tips are thoroughly cleaned with reverse osmosis filtered water and mounted in tip holders like in Figure 5-5 and are ready for insertion into the vacuum chamber. The sharp tungsten tips still have an oxide layer on them that will have to be removed before use for STM.

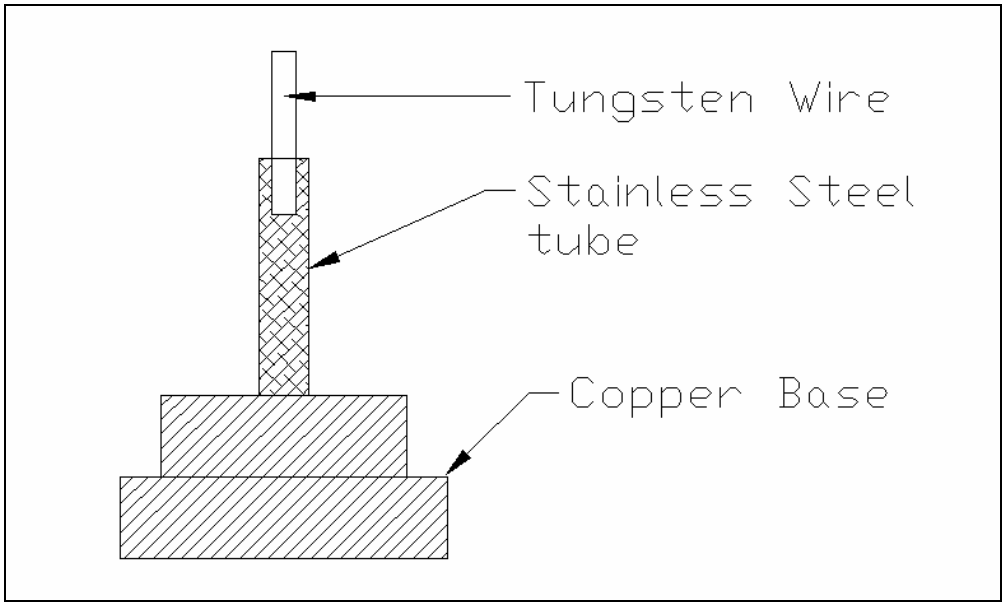

Figure 5-5 The tip holder

The tip is placed in the preparation stage and the oxide layer is removed by heating the tip by electron bombardment. The tip is held about a millimeter away from the hot filament. A large potential of about 400 V is placed between the tip and the filament with the tip being positive. Current is passed through the filament causing it to heat up and glow white hot. More importantly, electrons are thermionically ejected from the filament and because of the large potential, are directed to the tip. Because the tip is so sharp, the electric field directs the electrons to the end of the tip. The bombardment causes the tip to heat up and the oxide layer is blown off into the vacuum.

Unfortunately, during this electron bombardment process, the tip may become slightly duller because of "cold flow" processes or even melting the tungsten. To investigate the suitability of a tip for STM it is characterized by field emission before use. A similar set up is used for field emission as the electron bombardment. Now, a potential is placed across the tip and filament with the tip being negative. If the tip is sharp enough, eventually the strong field lines at the end of the tip will result in

electrons being ejected from the tip and traveling to the filament. This small current is measured to indicate field emission. The barriers to this field emission are non-conductive oxides and a dull tip. The oxides are non-conductive and serve as an insulating layer on top of the tip. If the tip is too dull, the electric field is not strong enough to cause Fowler-Nordheim tunneling. To characterize the tip, the voltage is ramped slowly while the current is monitored. The onset of field emission is recorded and then monitored. A stable current suggests that the tip is clean. A low onset of field emission suggests that the tip is sharp. Once a tip has been characterized as being suitable for STM, it is immediately transferred to the STM head for use.

5.2.2 Preparing Clean Silicon Samples for UHV

Wafers of 3" (76.2 mm diameter) 356-406 um thick 1-1-1 n-type antimony doped 0.02 – 0.05 Ω silicon were purchased from Montco Silicon Technologies and cut to small strips measuring 1.5 mm × 12 mm. The wafers purchased are mechanically polished on one side and rough on the other. Although the wafers are relatively clean out of the box, there is still an oxide layer and other minor contaminants that need to be removed. Also, they are handled in unclean air that has hydrocarbons and other contaminants.

To remove carbon contaminants, the sample pieces are cleaned using a simplified RCA process [63]. The samples are bathed in a 1:1:4 solution of hydrogen peroxide, ammonium hydroxide, and ultra pure water respectively. A water bath is heated to 75˚C before the samples in the RCA solution are submersed. For 10 minutes, swirling every 2-3, the samples are held in the solution. Following this, the solution is diluted with ultra pure water 10 times while keeping the samples submersed to keep carbon contaminants in the air off the surface. The samples are stored in water before use.

After the RCA cleaning process, a sample is mounted on a sample holder like the one shown in Figure 5-6 and is then placed into the UHV chamber to protect the sample from further contamination from the atmosphere. At this point, most of the contaminants are removed but there is still an oxide layer on the samples. Also, there is water still adsorbed that must be removed. First, the water is removed by heating the sample to 630˚C overnight. This effectively boils off any water that might be stuck on the sample. Also, the hot sample heats up the sample holder and surrounding parts and doing so removes many of the contaminants it picked up in air. The sample is left to cool down to room temperature after this initial process.

To remove the oxide layer, the sample is heated to near the melting point. Silicon melts near 1410˚C. The samples are heated to 1235˚C while keeping the pressure in the chamber low. At this temperature, silicon evaporates off the sample surface and the oxides on the surface are simultaneously removed with the evaporating material. The oxides are now in vapor form and easily pumped out of the vacuum chamber, or deposited on the nearby walls. The oxides will remain solid on the chamber wall and will not re-contaminate the sample. Once 1235˚C can be held for 10 seconds with the pressure in the range of $2x10^{-10}$ torr, then the sample is slowly cooled down at 1˚C per second. The 7x7 reconstruction happens at around 860˚C and the slow cooling helps minimize defects. The process of preparing a good Si(111) 7x7 surface is explained in more detail in Section 5.3.

Figure 5-6 shows an exploded view of the sample holder itself. The sample holder base is constructed of copper and has an approximate diameter of 0.75 inches. The components have low vapor pressures and conduct heat well. The sample holder also has electrical insulators that enable current to pass through the sample for the preparation process. A small tab on one side is used to transfer the sample holder using the wobble-stick transfer mechanism in our chamber.

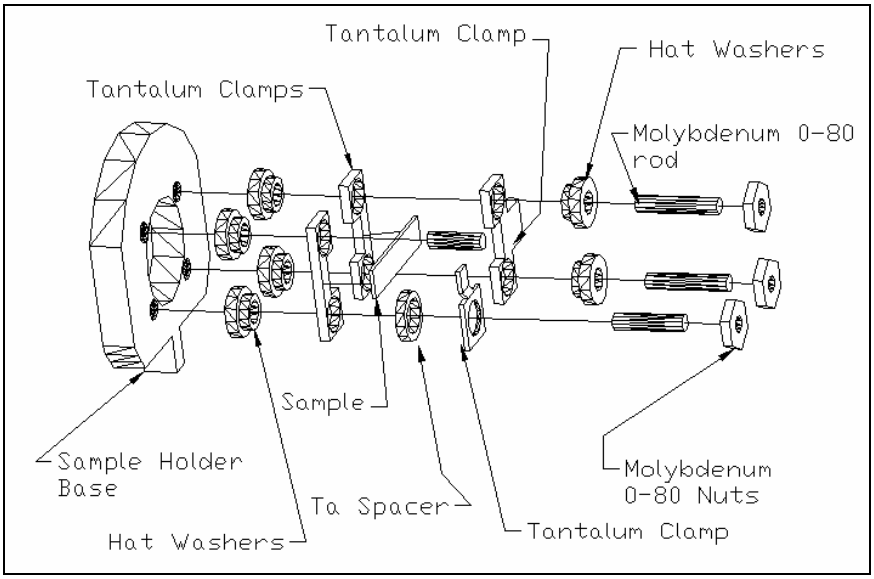

Figure 5-6 The sample holder

5.3 Preparing Si(111) 7x7

Once the tips and samples are loaded into UHV, the next step is to anneal the Si(111) surface with the goal of creating large terraces of clean 7x7 reconstruction with few defects. The silicon surface is complicated enough without the additional need to understand the physics near defects and contaminants. For efficient experimentation on this surface, the production of the 7x7 surface must be easily repeatable. There are many points to note when preparing the surface. This section discusses only how to prepare the 7x7 surface. The details on the reconstruction itself were discussed in Chapter 1.

If the Si(111) surface is cleaved in vacuum, the energy of the surface is very high. This is because there is a large density of dangling unoccupied bonds protruding into the vacuum. The surface is unstable and has a high surface energy. One way to reduce surface energy is to close together the dangling bonds.

As the surface is heated, at around 300 ˚C and 400 ˚C the surface reconstructs into a 5x5, 9x9, 11x11 and 7x7 reconstruction [64, 65]. As the surface continues to be heated, beyond 860 ˚C the surface loses its 7x7 order and becomes 1x1 [65]. When silicon is heated above 860 ˚C and then cooled, the surface re-assembles into a 7x7 structure, the most stable. The speed of cooling through the 860 °C regime is very important because cooling too fast can lead to quenching of the surface and many defects and mis-reconstructions. The speed of reconstruction above 860 °C is very fast to 7x7 and slowly cooling below 860 °C produces large 7x7 surfaces.

The Si(111) 7x7 surface is terminated by dangling bonds which makes it highly reactive. To keep the surface from reacting with undesired contaminants, the pressure must remain very low in the chamber. This presents difficulties because as the temperature of the sample is raised, the surrounding areas and the sample itself will outgas and this raises the pressure of the chamber. Therefore, the pressure must be monitored during the heating process and ensure that it remains low. Generally, it is found that samples that are prepared with the lowest chamber pressures over time are the cleanest.

To prepare the 7x7 surface, great care is needed in the temperature ramping and control. The process is time dependent and to get the best samples of clean uniform 7x7, a specific recipe is followed. To reliably reproduce sample surfaces, the entire process is automated by a computer program. This program is connected by hardware to the ionization gauge controller to constantly read the chamber pressure. It is connected to a digital optical pyrometer to read the temperature of the sample. The computer program then controls the heating through control of a power supply connected to the sample.

The annealing control software, shown in Figure 5-7, implements a Proportional-Integral-Derivative (PID) temperature controlled algorithm and a process recipe enabling samples to be

prepared autonomously at the press of a button. The PID control is the most complicated and most important component of this program.

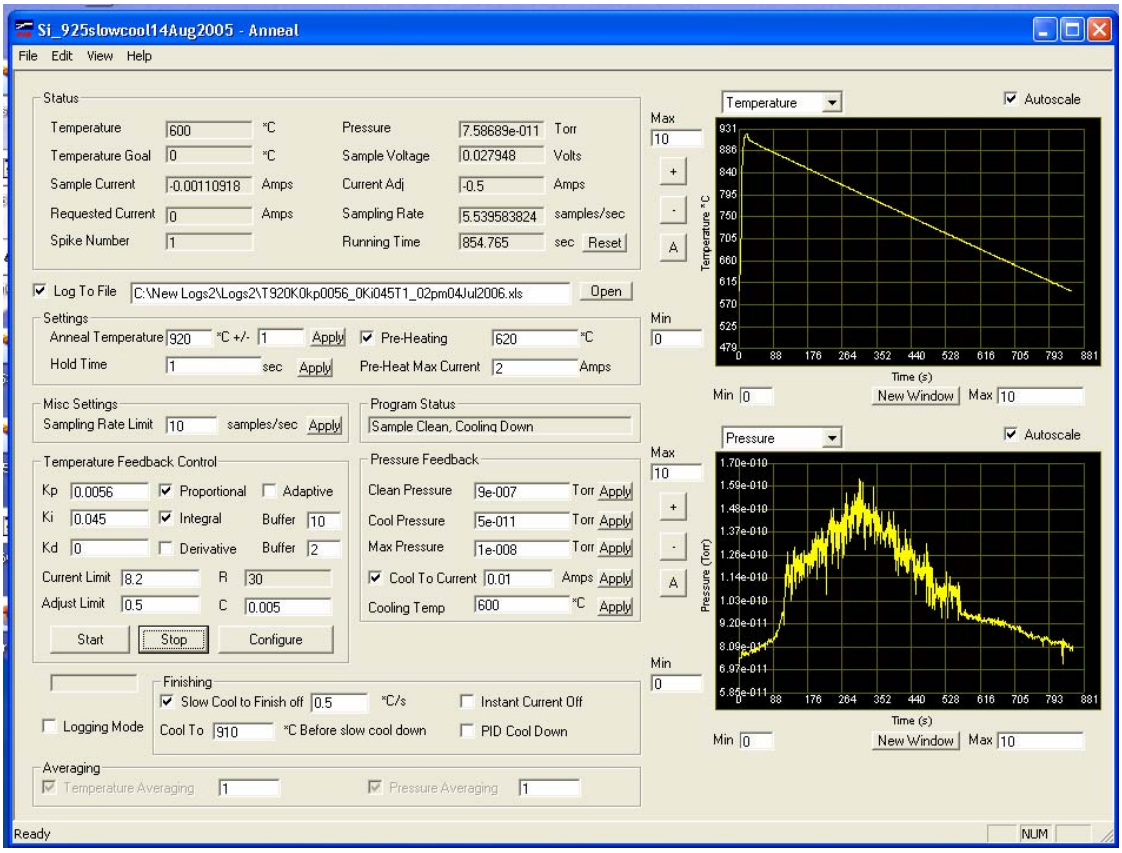

Figure 5-7 Screenshot of annealing program

The program was written in visual C++ by myself and interfaces to an Agilent 4551 power supply through a GPIB interface. The pyrometer is recorded through an RS-232 connection and the pressure is recorded through a Keithley KPCI-3108 DAQ card. Figure 5-7 shows the program after a slow cool down resulting in a 7x7 surface.

5.3.1 PID Temperature Control

Temperature control is achieved using PID feedback. Because silicon is a semiconductor, its resistance changes greatly with temperature. This makes controlling the temperature with ohmic heating very difficult. A constant current through the sample will not produce a constant temperature. To maintain a certain temperature, feedback is required. The temperature is constantly monitored using the optical pyrometer and adjustments are made to the current to maintain the set temperature.

The set point is defined as the temperature at which one wants the sample to be at and the error as the difference between the present temperature and the set point. The algorithm used to calculate the power input for the feedback is

$$P_{in}(t) = K_p \cdot e(t) + K_i \int_{-\infty}^{t} e(t)dt + K_d \cdot \frac{de(t)}{dt}. \qquad (5\text{-}3)$$

The *K* values are constants and control the amount of proportional, integral and derivative feedback used. It is interesting to note that this algorithm will work without any proportional or derivative feedback, but integral feedback is always required to work properly. The feedback constants are tuned to the system so that the feedback is critically damped. For the sample annealing program, only proportional and integral feedback is used.

Before really considering PID control, one must make considerations about the dynamical behavior of the system. By discussing the system in terms of energy, the rate of change of energy of the system is written as:

$$\frac{dW}{dt} = P_{in} - P_{out}, \qquad (5\text{-}4)$$

where *W* is the total energy in the system and *P* is power. In such a way, energy entering and leaving the system can be considered. Looking at the right side of the equation, energy can leave the system

in three ways: i) thermal conduction through physical contact, ii) thermal radiation, and iii) thermal convection.

Note that if one considers the case of a vacuum, then #3 can be neglected. Looking at the left side of the equation, the total energy of the system must be able to be related to the temperature. In general this is:

$$W = \int C_p dT , \qquad (5\text{-}5)$$

where C_p is the heat capacity of the system (extensive). C_p is not constant with temperature, but because the range of control needed is small, a constant C_p can be assumed. Therefore, a more practical version is given as:

$$W = c_p \cdot V \cdot T \qquad (5\text{-}6)$$

where now c_p is the specific heat capacity per volume (intensive). More generally, an effective capacitance $C = c_p V$ [66] is defined such that:

$$W = C \cdot T \qquad (5\text{-}7)$$

The rate of energy flow in J/s due to conduction is directly proportional to the amount of contact area (A) between surfaces and inversely proportional to an effective distance (L_{eff}) through which conduction occurs. One can assume that the temperature of the system is uniform inside the system and that the temperature outside the system (T_0) is always constant such that the thermal gradient over the area of contact is the same everywhere. The rate of energy transfer through conduction is written as:

$$P_{tc} = \frac{\kappa \cdot A \cdot (T - T_0)}{L_{eff}} , \qquad (5\text{-}8)$$

where κ is the constant of conductivity with units of W/mK.

The power transfer due to thermal radiation (or absorption) can be obtained through Stefan's law and is written as:

$$P_r = \varepsilon \cdot S \cdot \sigma \cdot \left(T^4 - T_0^4\right), \qquad (5\text{-}9)$$

where ε is the emissivity, *S* is the surface area, σ is the Stefan-Boltzmann constant $5.67x10^{-8}\ \frac{W}{m^2K^4}$ and T_0 is the ambient temperature.

By defining an effective resistance to heat flow, *R*, the power traveling through the system can be given as:

$$P_{out} = \frac{T - T_0}{R}, \text{ where } R \text{ has units : } \frac{Kelvin \cdot s}{J} \quad . \qquad (5\text{-}10)$$

The heat lost through thermal radiation is much less than the heat transfer through conduction and so, the resistance to heat flow is approximated to be due to resistance in contact for thermal conduction. It is easily observed by comparing the equations (5-10) and (5-8) that the effective resistance is given by:

$$R = \frac{L_{eff}}{\kappa \cdot A}. \qquad (5\text{-}11)$$

Combining these equations with equation (5-3), a linear first order differential equation is obtained that serves as a model of the behavior of the system:

$$\frac{dT}{dt} = \frac{P_{in}}{C} - \frac{T - T_0}{R \cdot C} \qquad (5\text{-}12)$$

If one considers the input power as a constant, one can perform a simple analysis of this equation to describe the behavior of the system to a constant P_{in}. This will give the transient response of the system without any PID control. Knowing the transient response is important to understand how the system will respond to a changing input. The calculation can be found in Appendix B.

$$T(t) = R \cdot P_{in} + T_0 + \left(T(0) - R \cdot P_{in} - T_0\right) \cdot e^{\frac{-t}{RC}} \qquad (5\text{-}13)$$

Observing the limit as $t \to \infty$, the temperature will settle at $T_0 + R \cdot P_{in}$. This tells us how the temperature of the system will change with a change in input power. This is very important to know if one wants to control the temperature.

Assume one wants to obtain a temperature of T_s (temperature set point). In order to do so, P_{in} must be varied so that the system temperature will change and eventually approach the state that $T = T_s$. The path to approach this condition depends on the various parameters in the PID equation given in (5-3). A value describing the system is defined:

$$Q^2 = \frac{-\kappa_i \cdot \left(1 - \kappa_d\right)}{\left(1 - \kappa_p\right)^2}, \qquad (5\text{-}14)$$

and the following constants are used in (5-14)

$$\begin{aligned} \kappa_p &= K_p \cdot R \\ \kappa_i &= K_i \cdot R^2 \cdot C \\ \kappa_d &= \frac{K_d}{C} \end{aligned} \qquad (5\text{-}15)$$

Where $\kappa_p, \kappa_i, \kappa_d$ are dimensionless. Q is a positive number called the quality factor. This quality factor is similar to the quality factor discussed in in the sense that it is related to the number of times the temperature "rings" around the set-point. There are three interesting cases for the value of the quality factor: $Q > 1/2, Q = \frac{1}{2}, Q < 1/2$. Each condition pertains to the roots being respectively real (either negative or one positive one negative), unique, or imaginary.

The values of $c_+ \,\&\, c_-$ are

$$c_+ = \frac{\tau \cdot (T_{s1} - T_{s0}) \cdot \{1 + \tau \cdot s_+\}}{s_+ - s_-}$$
$$c_- = \frac{\tau \cdot (T_{s1} - T_{s0}) \cdot \{1 + \tau \cdot s_-\}}{s_+ - s_-} \qquad (5\text{-}16)$$

Taking the inverse transform results with

$$e(t) = c_+ \cdot e^{s_+ \cdot t} - c_- \cdot e^{s_- \cdot t} \qquad (5\text{-}17)$$

This general result has many interesting details buried within. There are many conditions that pertain to stable and unstable solutions. The most basic observation is the real part of the roots. If the real part is greater than zero, that means that as time increases, the error grows exponentially and there will eventually be instability as $t \to \infty$. Also interesting are the constants. If one considers the case of only one real root, then the denominator becomes zero and there is a singularity in the solution. Since this is not what happens in actual experiments, one must consider the limit of the constants to obtain realistic results for the error. Considering again no integral feedback, there is only one root. The algorithm still changes the temperature, but the system will not settle at the desired set point. The following are examples of possible stable solutions using a unit value for *R*, *C*, and $R \cdot C$ and a step from 0 to 100.

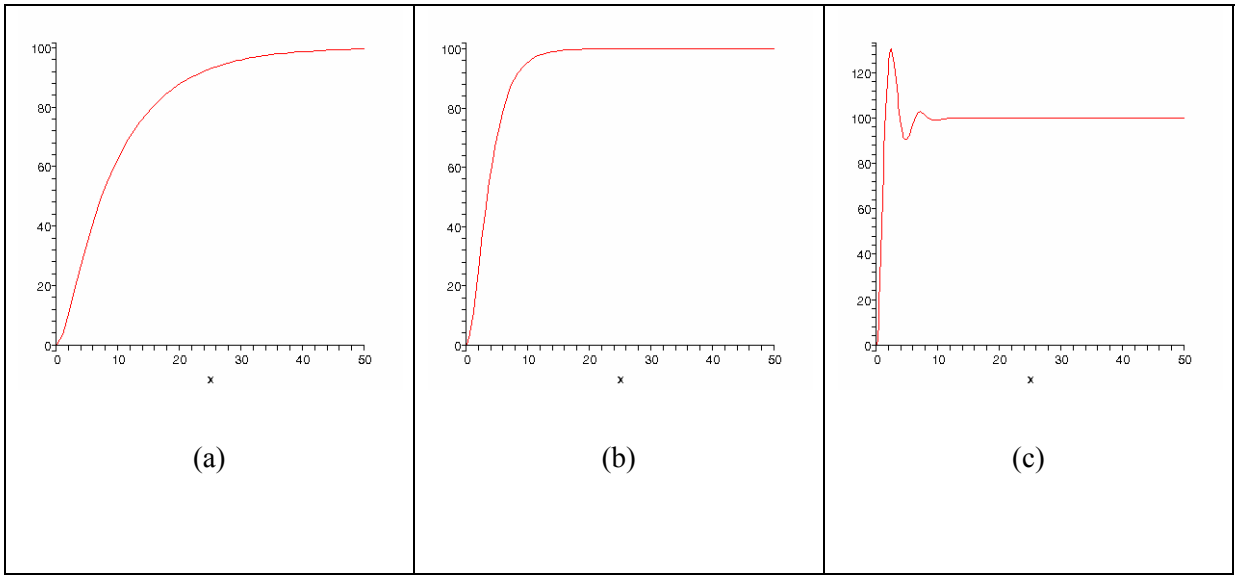

Figure 5-8 The different PID feedback conditions. (a) overdamped (b) critically damped (c) underdamped

For Figure 5-8 (a) above, Q=0.32, $\kappa_p = 0, \kappa_i = -0.1, \kappa_d = 0$. For Figure 5-8 (b), Q=0.5, $\kappa_p = 0, \kappa_i = -0.25, \kappa_d = 0$. For Figure 5-8 (c), Q=1.41, $\kappa_p = 0, \kappa_i = -2.0, \kappa_d = 0$.

When controlling the temperature of the sample during annealing, the system has to be tuned to be critically damped. The temperature is brought very close to the melting temperature of silicon, and so there cannot be any overshoot in the temperature past the set point. Even a small overshoot may result in a melted sample. On the other hand, one doesn't want the temperature rise to take too long. A long rise will cause excessive outgassing and contaminate the sample.

The fact that the resistivity of the sample changes with respect to temperature (silicon, which is a semiconductor and not an ohmic conductor) means that the system responds non-linearly. PID feedback is most effective only for linear systems. The good news is that a set of feedback parameters near the set point results in quite good control of the silicon temperature. The problem is

that the parameters need to be adjusted for every sample annealed. Also, if the set point changes, the parameters have to change.

The performance of the PID algorithm for annealing can be seen by a close view of the temperature approach to the set point.

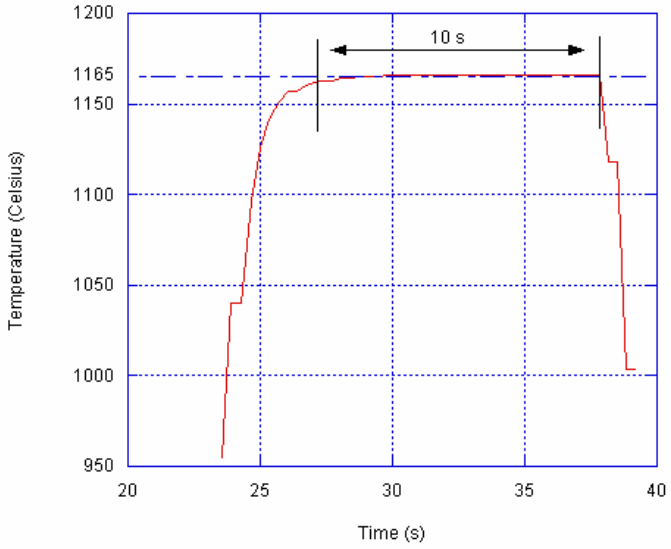

Figure 5-9 PID approach to set temperature during silicon annealing

For Figure 5-9, the sample is heated to 1165ºC for a period of 10 s. Once at the set temperature, the algorithm maintains keeps the sample at that temperature within 1 or 2 degrees Celsius, a value limited by the resolution of the pyrometer.

Chapter 6
Spectroscopic Imaging of Si(111) 7x7

6.1 Spectroscopic Imaging

Although topographic imaging is very useful, it does have its limitations. Having the ability with STM to observe a surface at and below the nanoscale in real space is an incredible feat. Unfortunately, this observation is sometimes made difficult to understand due to the nature of STM itself. Standard topographic imaging with STM provides real-space geometric information through a convolution of electronic information. Topographic imaging uses the integrated Local Density of States (LDOS) over a range of one or two eV in semiconductors. The LDOS is the localized number of quantum states near a specific energy. The goal is to gain information about the LDOS in semiconductors over a much smaller energy window.

When the STM is tunneling, electrons tunnel across the vacuum barrier from the sample to the tip. This is illustrated in Figure 6-1. The left side of the figure represents the sample, and the right side the tip. The gap in the middle is the vacuum. The Fermi level (FL) of the tip is shifted down, representing a bias between the sample and tip. The sample is a semiconductor, and has a band gap represented by the empty space in the middle of the left side. The band gap of silicon is about 1.1 eV. The reconstructed surface of silicon is a conductor, and the energy of electrons on the surface resides inside the bulk band gap. The adatoms are represented by two sharp closely spaced Gaussian peaks. The rest atoms are represented by a wider Gaussian peak approximately 0.8 eV below the FL of the bulk silicon [67].

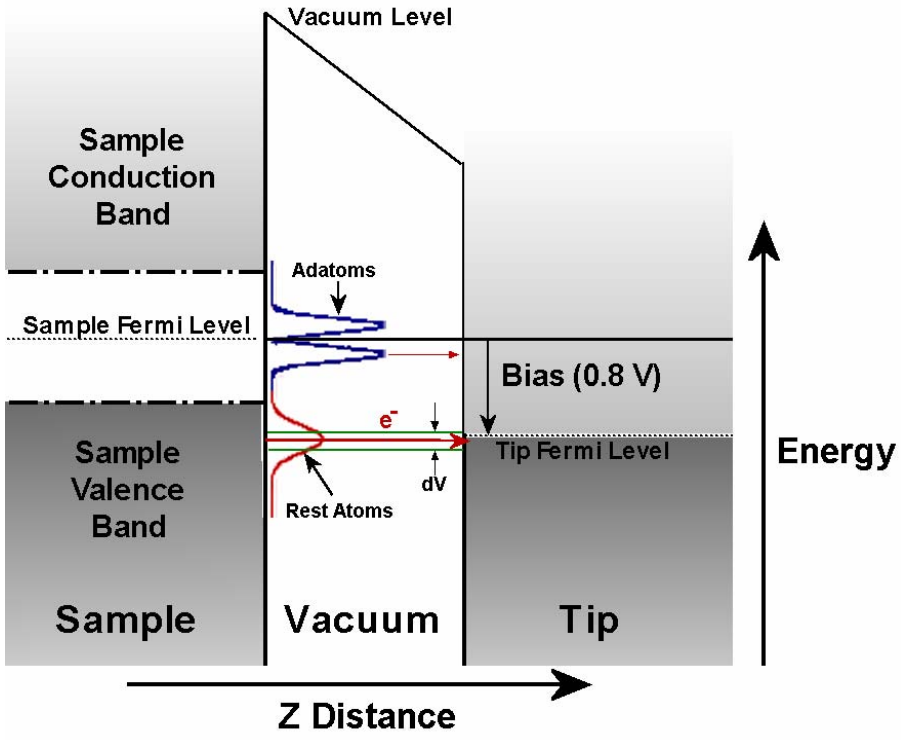

Figure 6-1 Diagram of electron tunneling from sample occupied states to the tip. Tunneling electrons are represented by arrows pointing right.

In Figure 6-1, electrons from these surface states tunnel across the vacuum barrier and into the tip, as represented by arrows pointing to the right. In this case one would say that one is imaging occupied states of the sample. The tip FL is offset by the applied bias to coincide with the energy of the RA state. The total tunneling current will be made up of electrons tunneling from states that are from many energies between the sample FL and the tip FL. The total tunneling current will consist of electrons from the adatom states, Rest Atom (RA) states, and other states with similar energies.

6.1.1 Tunneling Current

The total tunneling current is due to the sum of transitions from all states in the tip and sample. The tunneling current at a specific bias *V* can be approximated as [22, 68]

$$I \alpha \int_0^{eV} dE \rho_T(E_F - E + eV)\rho_S(E_F - E)T(E, eV) \qquad (6\text{-}1)$$

when $|eV| < \varphi$, the work function of the surface. $T(E, eV)$ is a function describing the transmission probability of an electron between the tip and surface. This function, called the tunneling matrix, depends on the tunneling bias and the energy of the electron. ρ_T and ρ_S are the density of states of the tip and sample. Interpreting equation (6-1) shows that the tunneling current is a convolution of both the tip and sample states. In most STM experiments, the item of study is the sample and the tip should not interfere with the function of a microscope, however, the electronic structure of the tip will always somewhat influence STM. In order to avoid confusing features from the tip and sample, a metallic tip is used with ideally a featureless DOS where at the sample surface states energies. Also, for spectroscopy, the direction of tunneling will influence which states dominate the data. Whether electrons tunnel from the tip to the sample (unoccupied states), or from sample to tip (occupied states), will determine the degree of influence of the tip DOS [68]. The unoccupied states images are easiest to interpret. The influence of the tip in Scanning Tunneling Spectroscopy (STS) spectra has been studied by other groups [69]. It is believed that the tip states influence spectroscopic data irregardless of the tunneling distance but the influence on topography from the tip DOS changes greatly.

The transmission probability comes from the solution to the quantum mechanics tunneling problem. The probability of transmission through a vacuum decays exponentially with distance. Additionally, the barrier height and tunneling bias influence the probability of transmission. It must

also be noted that the electrons are tunneling from bound states on the surface and one additional influence is the perpendicular momentum of the electron before it tunnels. The transmission coefficient can be written as

$$T(E,V) = e^{-2\kappa s}. \qquad (6\text{-}2)$$

The contributions from the bias, barrier, and electron momentum are combined in the inverse decay length κ [22] is the separation between the sample and tip.

$$\kappa = \sqrt{\frac{2m\bar{\phi}}{\hbar^2} + k_{\|}^2} \qquad (6\text{-}3)$$

$\bar{\phi} = (\phi_s + \phi_t/2) + E - 1/2\,eV$ is the average barrier height between the tip and sample, which also depends on the electron energy and the bias.

It is important to note that the tunneling current is the sum of the contributions of electrons from all surface states from the Fermi energy up to the bias. This means that all states contribute electrons to the tunneling current as a function of the density of states. It is impossible to determine which state a specific electron came from in the tunneling current, but the approximate energy of the electron can be determined which can map out the states which contribute the most electrons at a specific energy. There is no way, however, to filter out electrons so that they only tunnel from specific states.

6.1.2 First Derivative of the Tunneling Current

If the first order derivative of the tunneling current with respect to the bias voltage is taken, an equation is obtained that describes the variation of the tunneling current to bias at a specific energy. To simplify calculations, the tip DOS can be assumed to be an s-type orbital [70], then the tunneling current can be approximated by the expression

$$I \alpha \int_0^{eV} \rho_s(E) T(E,V) dE \,. \qquad (6\text{-}4)$$

And then, the derivative is

$$dI/dV \alpha \rho_s(eV) \cdot (e\,T(eV,V)) + e\int_0^{eV} \rho_s(E) \frac{\partial}{\partial(eV)} [T(E,V)] dE \qquad (6\text{-}5)$$

The first term of this equation contains the sample DOS at the tunneling bias V multiplied by the barrier effects. The second term is the background contribution from the other sample states. In effect, equation (6-5) filters the electronic contribution to the tunneling current and will have general features proportional to ρ_S. For this equation, because of the large influence of the tunneling barrier, the derivative will largely depend on the tunneling separation and the bias. This is a problem for taking spectra at different separations and varying biases. To somewhat eliminate the effects of the tunneling barrier, this equation can be normalized by I/V.

$$\frac{dI/dV}{I/V} = \frac{\rho_s(eV) + \int_0^{eV} \frac{\rho_s(E)}{T(eV,V)} \frac{\partial}{\partial(eV)} [T(E,V)] dE}{\frac{1}{eV}\int_0^{eV} \rho_s(E) \frac{T(E,V)}{T(eV,V)} dE} \qquad (6\text{-}6)$$

The transmission coefficient is exponential in nature and the ratios will generally cancel any dependence on the tip-sample separation and the tunneling bias. Generally, since the second term in the numerator and the denominator are both integrals, they will be slowly varying functions compared to $\rho_s(eV)$. Sharp features in the $\rho_s(eV)$ function will be prominent in the spectrum.

Experimentally, these spectra can be taken directly by turning off the feedback and stopping the scanning while varying *V* and recording the current. From the measured current, a derivative will

give dI/dV . At this point, the tunnel junction is still convolved in the data. This type of spectroscopy is useful for observing the LDOS at a specific point on the surface. Unfortunately, if thermal drift is large, then it is quite difficult to be certain of where the measurement was made. Also, making the measurement may cause changes to the surface due to the high electric fields and tunneling electrons [10, 18, 20, 71-73]. Repeat measurements and statistics increases confidence in the data and single molecule chemistry can be observed [74].

6.1.3 Acquiring Spectroscopic images

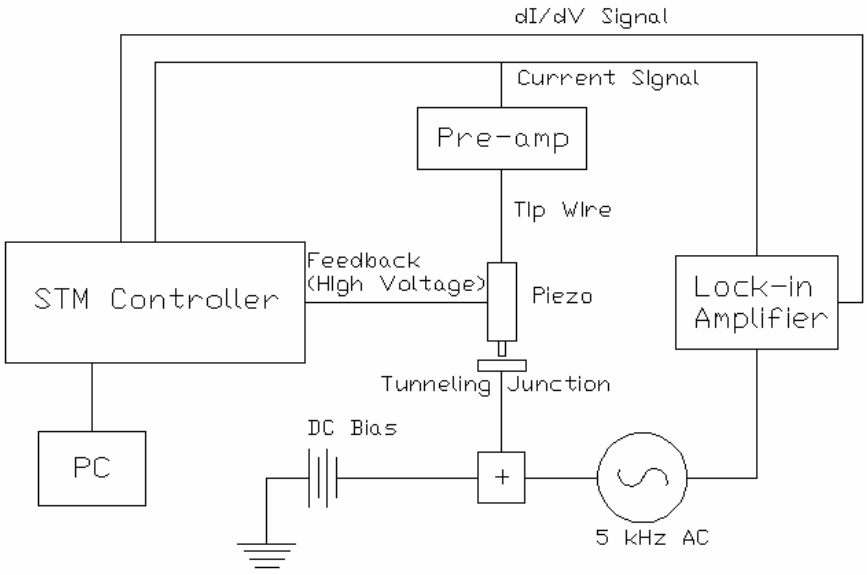

Figure 6-2 Schematic of STM conductance imaging set-up

When acquiring point spectra, it was important to consider the effects of the tunneling barrier on the data. For a different type of experiment, the sample DOS can be measured near a fixed bias and the tip scanned along the surface. For this experiment, the article of interest is the real-space distribution of a DOS feature. The experiment was first described by Becker et al. [34]. The

spectroscopic images are acquired concurrent to topographic imaging. A small amplitude sinusoidal ripple is superimposed onto the normal tunneling bias (see Figure 6-2). The frequency of this ripple is important and it must be out of the range of the feedback bandwidth which is around 1 to 2 kHz. Frequencies of 4 kHz to 7 kHz are acceptable and are chosen to maximize the Signal to Noise Ratio (SNR). The amplitude of this ripple is small. It is in the order of 0.1 V and so does not greatly influence the imaging of the semiconductor surface. See the small interval dV near the tip FL in Figure 6-1.

The small ripple will cause phase rotated increases in the tunneling current which correspond to the DOS feature near the tunneling bias. The current signal is analyzed by a lock-in amplifier. The signal corresponding to the DOS that one wants has been rotated by the feedback circuit by some angle depending on the feedback constants. Also, there is a signal 90 degrees out of phase caused by the tunneling capacitance and the AC signal applied. The lock-in phasor has to be locked onto the DOS signal and filter out the other frequencies from the tunneling signal. This is done by temporarily disabling the feedback circuit and pulling the tip back to the point where there is no more current. The lock-in phasor is then offset to zero removing any influence from the capacitance. The tip wire is near the scan piezo so there is also a small amount of capacitance pickup of the feedback in the current signal. This causes a small rotation of the phasor when the feedback is turned on. Luckily, this rotation is small, and can be offset by measuring the rotation while tunneling with the feedback on and momentarily off.

The output from the lock-in is then connected to the STM instrumentation and is mapped concurrently with the acquiring image. When the DOS feature is large underneath the tip, the image will show a brighter spot. When it is small the image will show a darker spot. The spectroscopic image corresponds to the surface conductance at a specific bias and this technique is often called conductance imaging.

The result is a map of the DOS at a certain energy. This is useful especially for the purpose of mapping out real-space distribution of the electronic structure of the surface. The measured DOS window is not narrow enough to filter out individual states, but it is as close as one can get using this technique. The advantage to this spectroscopic imaging technique is that there is no need to normalize the image as with point spectroscopy. Also, the speed of imaging remains the same as with topographic imaging. This means that any thermal drift will have no great effect. Unfortunately, because of the nature of STM, the tip-sample distance will vary during the scan because the feedback will always have a small amount of error. This means that there will be some geometric information convolved with the spectroscopic image.

A similar technique by Hamers et. al. [23, 24] called current imaging tunneling spectroscopy (CITS) measures the LDOS in real-space concurrent to topographic imaging. At each pixel in the spectroscopic image, a short point-spectrum is taken at a few pre-defined biases. If two points are measured (a and b), the procedure is as follows. The feedback is turned on during the scanning and topographic data is recorded. Then, the feedback is turned off, and the bias changes measuring potential a, there is a delay to eliminate any capacitive effects and dI/dV is measured. The bias changes to potential b, there is a delay, and dI/dV is measured. This happens for the set number of measurements, then the feedback is turned back on, the tip moved, and the entire process repeats from the beginning.

The benefit to this technique over the previous one is that the tip-sample separation will be approximately the same for each point. Unfortunately, the time to acquire a CITS image is much longer than with conductance imaging. Also, capacitance effects require a delay before each measurement, adding further to the complexity.

The 5 kHz AC ripple is needed to provide the *dV* for spectroscopic imaging. The amplitude of the AC signal is in the order of 0.1V root-mean-square (RMS) or less. The STM controller converts the output of the lock-in amplifier to a digital signal so that it can be displayed concurrently with the topographic image.

To acquire spectroscopic images, the settings on the lock-in amplifier are important. The typical scan speed of the STM while acquiring spectroscopic images is 500 ms/line. The images are taken at 512x512 pixels resolution which means that each pixel takes approximately 1 ms of scanning time to acquire. The time constant on the lock-in is set to 3ms. The digital lock-in amplifier mimics the behaviour of an analog amplifier by introducing a digital RC filter. The time constant is the *RC* time constant used to filter the signal. Therefore, the bandwidth of the lock-in will be inversely proportional to this time constant. This slightly larger setting helps to eliminate noise from the spectroscopic image.

6.2 Bias Dependence in Topography Images: Electronic Effects

STM images of Si(111) 7x7 were acquired at room temperature. The tips and samples were prepared as described in Chapter 5.

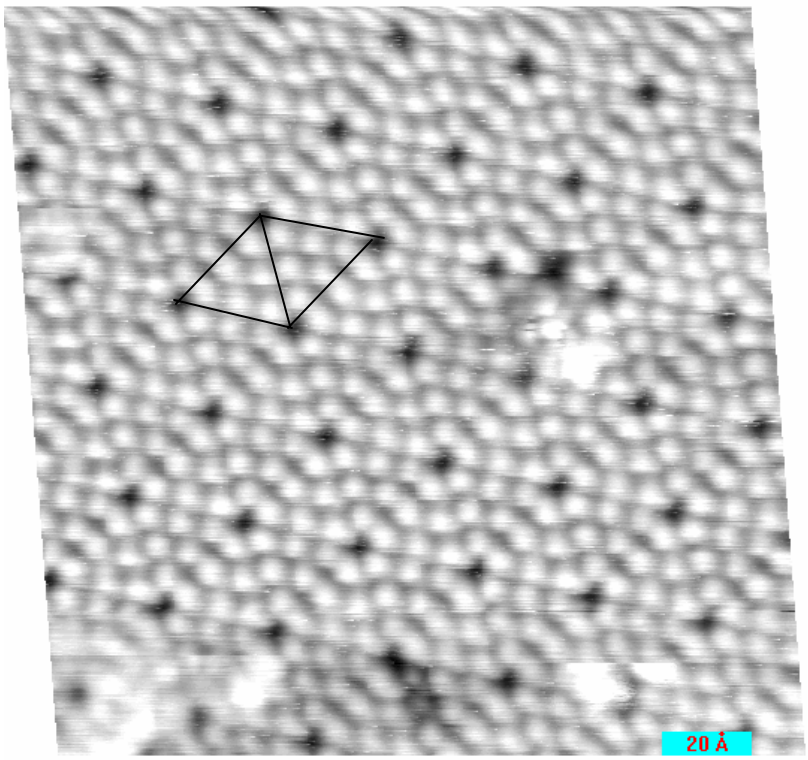

Figure 6-3 Unoccupied states +1.5V topographic STM image of Si(111)7x7 surface

The image in Figure 6-3 was acquired with a freshly prepared tip and the large white "blobs" are unknown contaminants that are deposited by the tip. What often happens when imaging this surface is that fresh tips will drop small amounts of material onto the surface. This process of dropping "blobs" tends to stop after an hour or so of scanning as the tip gets very clean. This is an unoccupied states image of the surface and the DAS structure is visible only by the adatoms and corner holes. There is no apparent effect of the stacking-fault in this image.

STM topography uses the tunnel current resulting from the integrated LDOS over the energy range defined by the two Fermi levels. The rest atom contribution to topographic imaging is much weaker than the adatom contribution for two reasons: i) the RA's are physically lower than the

adatoms, and ii) the tunneling barrier for electrons tunneling from the RA LDOS peak at -0.8V is higher than that for electrons tunneling from adatoms.

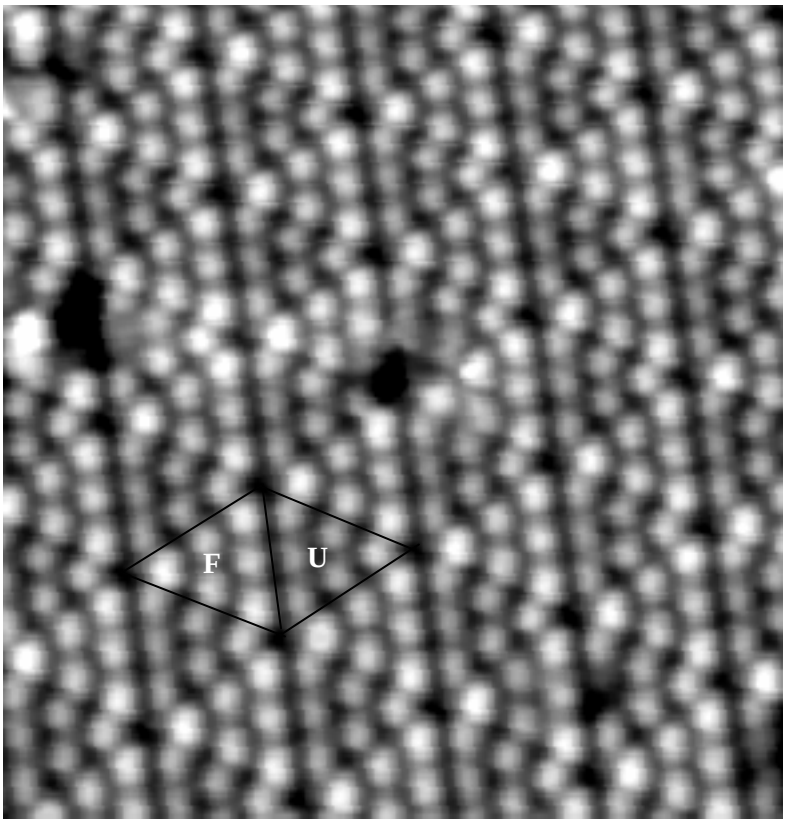

Figure 6-4 Occupied States -0.8V Topographic STM Image of Si(111) 7x7 surface

Figure 6-4 is an image of an area on the surface that was imaged several times. The dark defects correspond to missing silicon atoms on the surface. The effect of the stacking fault in the DAS structure is very apparent in the occupied states images. The faulted half of the image, labeled F, is imaged brighter (higher) than the unfaulted half, labeled U. In the reconstruction of the 7x7 surface, the faulted atoms are approximately 0.04 Å higher [75, 76]. In occupied states topographic imaging, this small physical height difference and the electronic difference enhance each other resulting in a strong contrast between the faulted and unfaulted halves of the unit cell. In unoccupied

states imaging, the two halves appear the same. In this case, the physical height difference is canceled off by the electronic structure. This is a good example of how the electronic-geometric convolution in STM can be confusing.

The dangling bonds from the rest atoms are not very visible in the topographic images, but they are more visible in the occupied states image than the unoccupied states image. The charge density in the adatoms saturates the image making the adatoms the predominant feature. Nevertheless, in Figure 6-4, one can see fairly clearly that the central position of each half of the unit cell (i.e. the center of each equilateral triangle) does not contain a rest atom.

There are many interesting phenomena in the occupied states image. The varied appearance of the adatoms is caused by charge transfer (CT) processes [77, 78]. Some of the obvious observations made from the occupied states images are: i) the faulted half of the unit cell is brighter than the unfaulted half, ii) the corner adatoms are brighter than the center adatoms, and iii) the rest atoms are barely discernable in-between the adatoms in occupied states imaging. The bias dependence clearly demonstrates that the LDOS function varies from adatom to adatom. In order to more directly measure the LDOS function, it would be desirable to use a technique that only accesses the tunneling current in a narrow energy window.

6.3 Spectroscopic Imaging of the Si(111) 7x7 Surface

Using topographic imaging, the rest atoms were difficult to observe. However, spectroscopic imaging at a specific bias corresponding to the energy of the rest-atom orbitals reveals them very sharply.

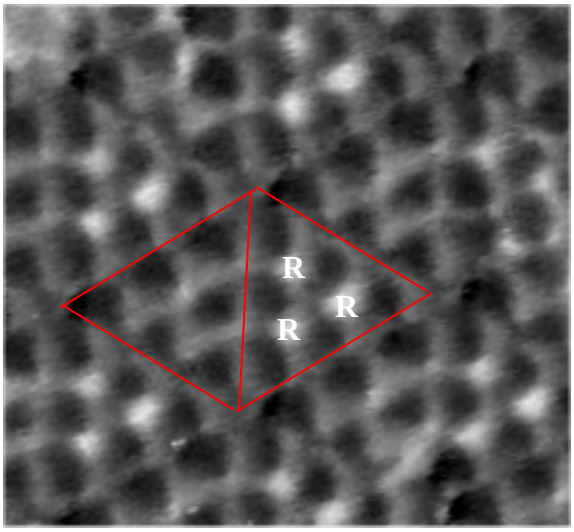

Figure 6-5 Conductance image of a Si(111)7x7 surface at -0.8V (occupied states)

The image in Figure 6-5 shows bright features on the rest atoms and dark features over the adatoms. This is because at -0.8 V, there are no DOS features from the adatoms and the rest atoms dominate this regime [23]. The adatoms are efficiently filtered out and the adatom sites are in fact the darkest features in the image. This clearly indicates that -0.8eV is well below the adatom DOS peaks located near +0.25 eV and -0.30 eV. The result of this filtering, or masking, is that the more subtle atomic-scale features of this complex surface can be seen and the rest atoms are now clearly visible.

The rest-atoms appear triangular in shape due to a masking effect from the adatoms. The signal producing this image still carries electrons from the adatoms in the topographic image and so near the adatoms, those electrons still saturate the signal. It is apparent from the conductance image that there is a difference between the rest atoms of the faulted and unfaulted halves. The rest atoms in the faulted half of the unit cell appear to be brighter than those in the unfaulted half.

From Figure 6-5, one can also discern a contribution at -0.8 V to the LDOS from the dimers, framing the unit cell. It is speculated that these dimer bonds must be quite highly strained in order to appear so strongly in this conductance image.

6.3.1 Rest Atom DOS from Spectroscopic Images

The greater brightness of the unfaulted RAs compared to the faulted RAs suggests that there may be a significant difference in the LDOS between these two types of RAs. However, a less provocative explanation is proposed.

When measuring the conductance image, it is important to remember that the tip height is controlled using the topography channel (something dominated by the adatoms). This means that the conductance measurement is made with the tip at a greater height, above the rest atom, in the faulted half-cell as compared to the unfaulted half-cell. Since the tunnel current depends exponentially on distance, this would mean that for a given dV value, the dI value would be larger over an unfaulted RA than over a faulted RA, all other things being equal. It is believed that this is the most likely explanation for the observed contrast.

Using spectroscopic imaging to observe the rest atom states gives STM the added ability to view surface features that would otherwise not be visible. One important measurement to make of the surface is the atom relaxations during reconstruction. This measurement is important to confirm molecular theories that help determine the behavior of the surface theoretically. One such measurement is the rest atom relaxation.

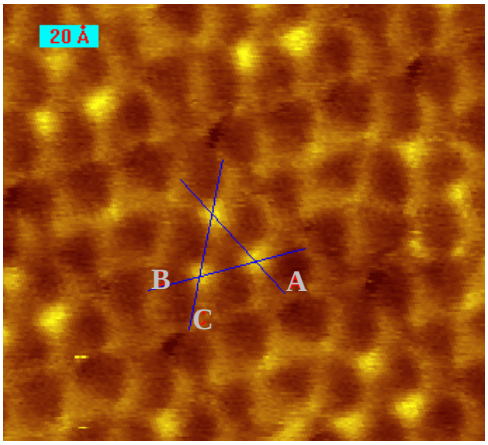

Figure 6-6 Measuring rest atom relaxations from spectroscopic images using scan lines

From Figure 6-6, the locations of the rest atoms can be approximately calculated. First, the image is calibrated for the lattice using features in the image. Then, scan lines are drawn and the peak separations are measured.

In an ideal diamond structure lattice, these atoms would have a separation of $a\sqrt{2}$, where *a* is the lattice constant. For silicon, *a* is 5.43 ångströms at room temperature. This means that the separation between rest atoms should be 7.68 ångströms. Using this method, the measured separations for the unfaulted half of the unit cell (bright RAs) is 7.34 +/- 0.12 ångströms. This is much smaller than the unrelaxed distance. For the faulted half, the measurement is 7.67 +/- 0.20 ångströms. The faulted half is much closer to the actual value. Unfortunately, the influence of the adatom relaxations in the masking of the rest atom states will alter the results slightly. To gain a better analysis from the spectroscopic data, a more in-depth electronic structure calculation must be done. Also, a more accurate method for peak finding and lattice calibration should be used.

From this early measurement, comparison of this experimental data to the theoretical results of other group's [79] energy minimization calculations are not in agreement.

Chapter 7
Bonding Structure of Benzene on Si(111) 7x7

7.1 The Benzene Molecule

At room temperature, benzene is found as a liquid and has a vapor pressure of approximately 80 torr. This makes it very easy to load into our gas line and dose into the UHV main STM chamber.

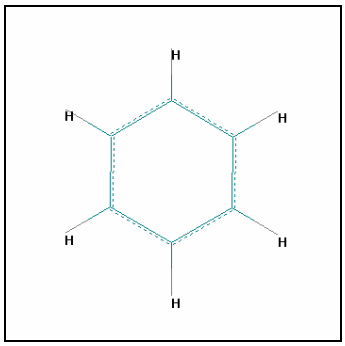

Figure 7-1 Drawing of a benzene molecule

The benzene molecule, shown in Figure 7-1, can be described as a ring of 6 carbons bonded with each other in a flat hexagon with one hydrogen atom bonded to each carbon. The benzene molecule is a member of a family of aromatic molecules. The term aromatic came about due to the sweet smell of the vapors. The bonds between carbons can be described using hybridized orbitals.

The carbons are sigma bonded by the overlap of two adjacent $sp^2 - sp^2$ hybrid orbitals and each carbon has an unhybridized $2p$ orbital with the orbits perpendicular to the molecular plane [80]. There are essentially 6 σ and 3 π bonds in the benzene carbon bonding. The bonding can sometimes be thought of as a resonance between a sigma and a pi bond.

The benzene molecule is highly symmetric, and uniquely stable because of the aromatic nature. It is resistant to various chemical reactions making it less reactive compared to the number of available π-electrons, however, it is still highly flammable. The high stability and nature of benzene makes it an excellent organic solvent and it has been used in the past as an organic solvent. However, it is highly carcinogenic.

7.2 Benzene on the Si(111) 7x7 Surface

There are three main types of adsorption onto surfaces. A molecule can dissociate into smaller components and chemically bond to the surface. That is, the original molecule finds it energetically favorable to sacrifice its structure and chemically bind to the surface as two different molecules or components. An example of dissociative bonding to the Si(111)7x7 surface is trichloroethylene [81, 82], in which a chlorine bond breaks causing two daughter products chemically binding to the surface. Dissociative bonding is generally very strong and not reversible.

A molecule can also non-dissociatively bond to the surface through some means. For example, the benzene molecule will attach with σ bonds to the surface and form a weak chemical bond [30]. This structure is shown in section 7.2.2. σ bonded molecules can often desorb back into their original state depending on the strength of the bond. Lastly, a molecule may physisorb onto a surface, such as benzene to Si(111)7x7 through a weaker chemical π bonding structure [36]. Physisorbed molecules are very weakly bound to the surface. A good analogy is a fingerprint on a surface for physisorbtion compared to a sticker for σ bonding. The print can be easily wiped off but the sticker needs significant energy input to remove it.

7.2.1 Adsorption and Desorption of Benzene to the Si(111) 7x7 Surface

Upon arrival at the silicon surface, from the gas phase, benzene is known to physisorb and become what is known as a mobile precursor [83]. In this state, the binding energy is 0.4 eV and at low temperatures (80K), benzene will stay on the surface in this precursor state and the resonance structure will remain intact. When physisorbed, the molecule readily diffuses across the surface. At room temperature, after a short stay in the precursor state, the molecule will either leave the surface and desorb, or "bite in" and form a chemical bond. When this chemical bond is formed, the molecule will lose its resonance structure. This means that the binding energy cannot be very high as only one π bond has been broken, but the C-C σ bonds are intact. The chemisorbed benzene has a relatively short residence time on the surface, about 20 minutes [16, 29].

The low residence time can be explained by thermally activated desorption. At room temperature, the binding energy of benzene is 0.94 ± 0.01 eV for the middle-faulted and 0.95 ± 0.01 eV for the corner-faulted adatoms by STM-TPD [84]. The molecules at room temperature have $\sim 1/40$ eV or 0.026 eV of thermal energy. The barrier to thermal desorption is roughly 50 times the thermal energy, which accounts for the short residence time.

The bonding of benzene molecules to Si(111) 7x7 has been studied theoretically [36-38, 85, 86] and experimentally [16, 29-31, 39, 84, 87]. All previous STM studies of benzene on Si(111)7x7 have been done observing unoccupied states. It is found from topographic STM imaging that at low coverages, the chemisorption results in the substantial dimming of single adatoms at unoccupied states.

Figure 7-2 shows consecutive scans of the same area of the surface. They clearly demonstrate how benzene molecules on a clean surface desorb over time. This desorption is caused by a combination of mostly thermal desorption and tip-induced desorption.

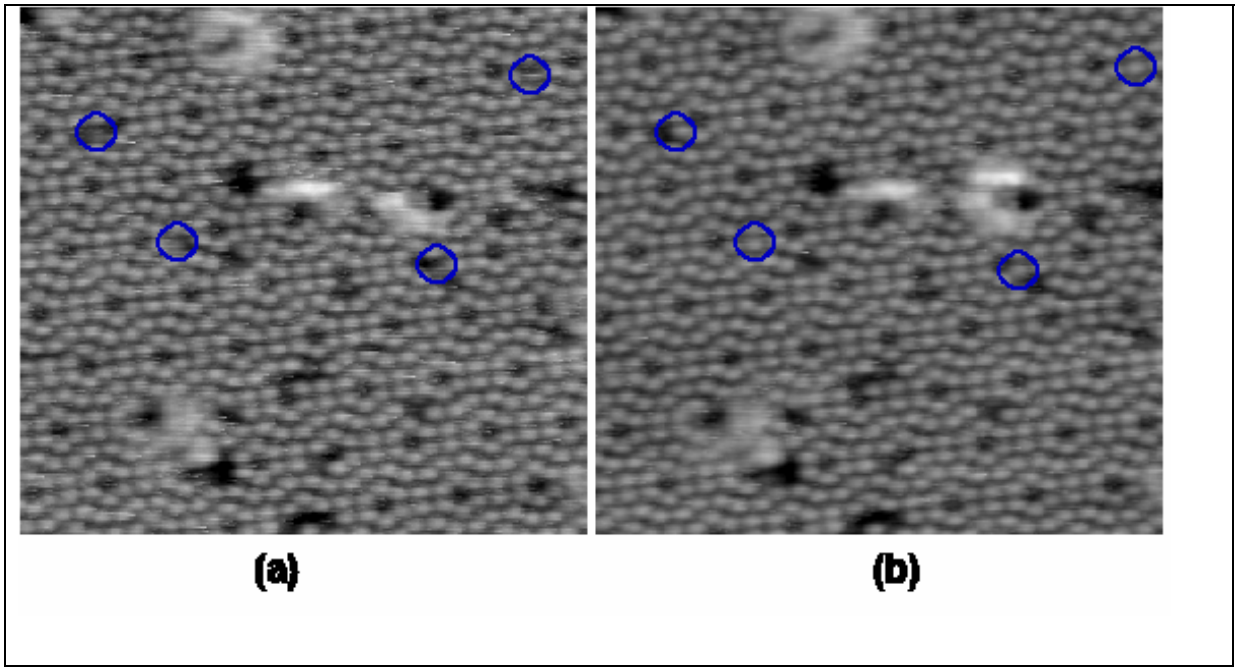

Figure 7-2 Si(111)7x7 surface dosed with 0.018L of benzene at room temperature, +2.0V topographic Images (a) 0 minutes after (b) 8.5 minutes after. The circles on the image indicate sights where a benzene molecule has desorbed.

Figure 7-2 is an example of desorption caused by the tunneling electrons themselves [72, 88]. This phenomenon has also been observed with the benzene on Si(100)2x1 system [14]. This tip induced desorption can be useful for the controlled removal of adsorbed molecules [17].

7.2.2 Binding Sites and Binding Configuration

At room temperature, it is generally believed that benzene binds to the Si(111) 7x7 surface in a 1-4 cyclohexadiene-like structure [31, 35, 89]. What happens is that the benzene molecule essentially sacrifices its symmetry and one resonating double bond is lost and the molecule forms a di-σ-bonded structure with one silicon adatom and one restatom. This structure is shown in Figure 7-3.

Figure 7-3 Model of benzene binding to a Si(111)7x7 surface

The molecule is no longer benzene, but more similar to 1,4-cyclohexadiene. The ring is now bent in a chair-like structure with the two double bonds parallel to each other and inclined from the surface. In STM images, the benzene appears dark in the image due to the fact that it has occupied the dangling bond from the adatom. There are multiple configurations for binding around a specific rest atom and it is sometimes difficult to notice the difference. This is specifically the case with benzene bound to a center adatom and a rest atom.

A similar molecule, toluene ($C_6H_5CH_3$), in which one of the hydrogens in the benzene is replaced with a methyl group, is thought to have the same binding configuration [38]. Preliminary data taken with near edge x-ray absorption fine structure (NEXAFS) experiments confirms that the molecule binds at a small angle to the surface, almost flat, at room temperature. See Appendix A for more information.

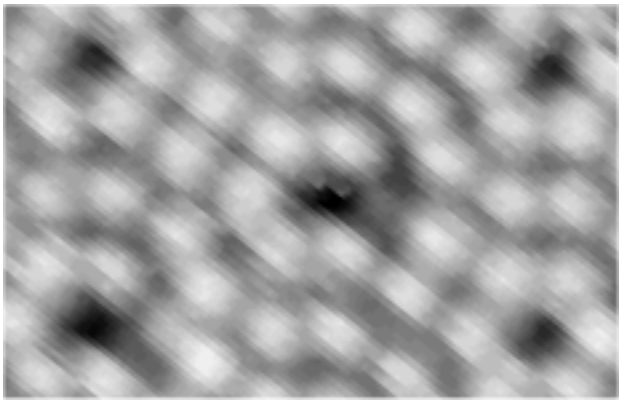

Figure 7-4 STM unoccupied states topographic image of one benzene molecule to the Si(111)7x7 surface

Figure 7-4 shows how the adatom is darkened once the benzene molecule adsorbs. In Figure 7-4, the grey spot to the immediate right of the corner hole in the middle of the image is a benzene molecule adsorbed onto the surface.

Unfortunately, STM topography does not tell us the precise binding configuration. As yet there is no definitive answer as to whether the 1-4-cyclohexadiene like bridge is or is not the binding configuration. For this reason, it was our goal to see if a definitive answer to this question could be found from using conductance imaging. If a neighboring rest atom is used to form the bridge bond, then one should see a dimming of that rest atom in conductance imaging near -0.8 eV.

For each unit cell on the 7x7 surface, there is room for six benzene molecules adsorbed in a 1,4-cyclohexadiene structure. This is because each unit cell contains only six rest atoms. The binding energy for each site is also different. There are four main types of binding sites on the unit cell: corner-faulted (CoF), corner-unfaulted (CoU), center-faulted (CeF), center-unfaulted (CeU).

Also, there are three corner configurations, and six center configurations for a benzene molecule for each half of the unit cell shown in Table 7-1.

Table 7-1 Benzene binding sites on half of the Si(111)7x7 unit cell

Corner	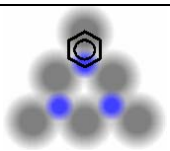	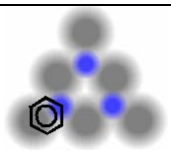	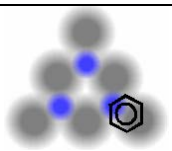			
Center	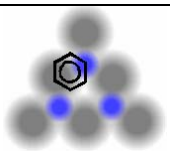	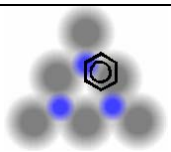	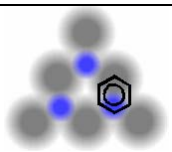	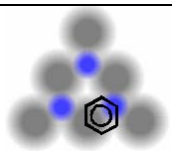	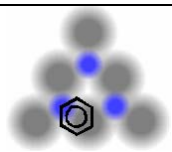	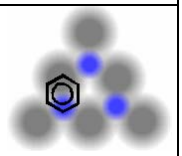

Any combination of these binding sites will be used by the benzene molecules until all three of the rest atoms are occupied.

STM images of benzene were taken at occupied states and unoccupied states and are shown in Figure 7-5.

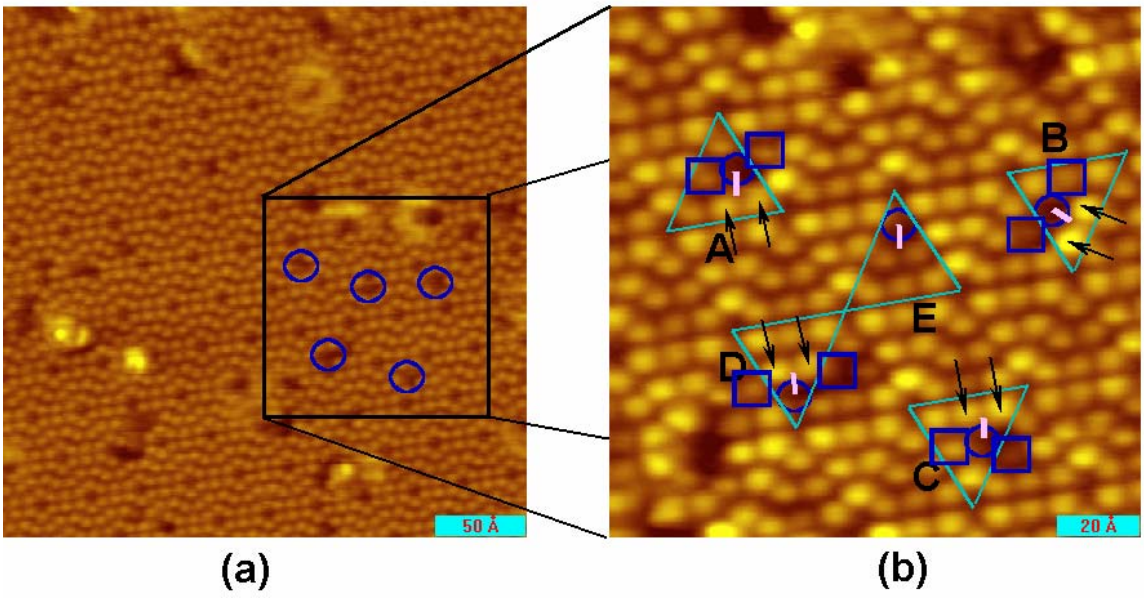

Figure 7-5 Benzene adsorbed onto Si(111)7x7 (a) unoccupied states +2.0V (b) occupied states at -0.7V

When benzene binds to the surface, the adatom binding site is observed easily in the unoccupied states images, but the rest atom site is unable to be observed. There are no discernable effects to the adjacent adatoms. In occupied states images at -0.7 V, the local electronic structure of the surface near the adsorption site is visibly affected. There is CT in the unit cell where the binding occurs, and even between neighboring unit cells. Three different types of CT processes were observed in these types of occupied states images. Type I: Figure 7-5 (b) half unit cells A, B, and C. Type II: Figure 7-5 (b) half unit cell D. Type III: Figure 7-5 (b) half unit cell E.

The type I configuration has the benzene molecule bound to a center adatom. A brightening of two nearest neighbor adatoms is observed as denoted by the arrows. In addition to the brightening, two adatom sites, shown surrounded by squares that are symmetrically opposite the occupied site,

dim. It is noteworthy that dimming occurs outside the unit cell with the bound molecule. The binding process clearly breaks the symmetry of the unit cell.

The type II configuration has the corner adatom site occupied and the two adjacent adatoms in the same unit cell brighten. The two adatom sites in the neighboring unit cells that are shown surrounded by squares, dim. In this case, the mirror symmetry across the long diagonal passing through the adatom binding site is not broken. In all of the observations made, the type II configuration has only been seen on faulted halves of the unit cell. The type III configuration is similar to the to the type II, but no brightening occurs. The type III configuration has only been observed on unfaulted halves of the unit cell.

This is the first time any of these observations have been made for benzene on Si(111)7x7 at occupied states. Type I configurations have been observed for chlorobenzene (C_6H_5Cl) by another group [17] also at occupied states. The Type II configuration has also been observed for chlorobenzene, but the Type III, where the two neighboring adatoms are dark has not been previously observed.

Spectroscopic *dI/dV* images of benzene at -0.7 V were taken in the hope of using the data to identify the rest atom that is involved in the binding to the surface. It was hypothesized that when the rest atom is bonded to, that the brightness of the DOS feature will diminish.

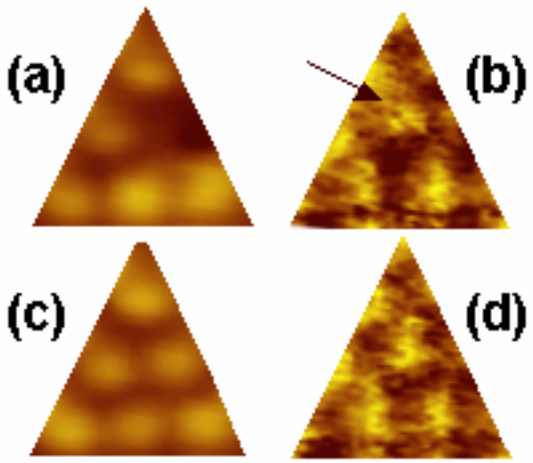

Figure 7-6 Topographic and conductance imaging of benzene on Si(111)7x7 at -0.7V (a) benzene topograpic image (b) benzene spectroscopic image (c) clean topographic image (d) clean spectroscopic image

In Figure 7-6, a type I binding to a CeU adatom in the unfaulted unit cell half is shown. What is observed in conductance imaging is very slight dimming of the rest atom site (Figure 7-6 (b)) across from the brightened adatoms. This suggests that the benzene might be bridging to the rest atom away from the bright adatom features. However, this dimming of the rest atom in dI/dV imaging suggests results that are opposite of those for chlorobenzene from reference [17]. The unoccupied states images of Sloan and Palmer at +3V show a bright feature near the brightened adatom sites. They attribute this brightening in unoccupied states to resonant tunneling through the π^* state of the molecule [17, 33]. It seems more investigation work is needed with conductance imaging is required before it can be used to identify the actual binding site.

Evidence has been obtained that strongly confirms which rest atom is indeed involved in the benzene binding structure. In one chance experiment, a unique tip was created with DOS features that at -1.5 V imaged rest atoms in the topography. A tip that images like this has been reported with

bismuth-covered tips [90]. When this tip was created for a short time, there was benzene adsorbed onto the surface and the rest atoms near the benzene disappeared.

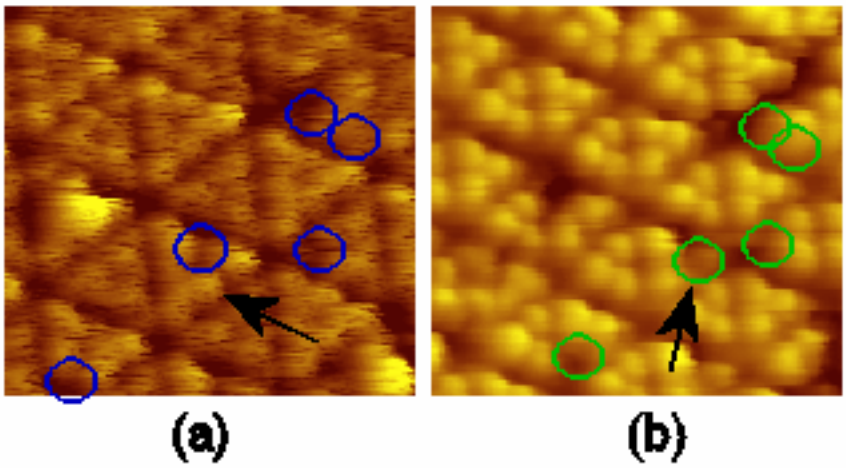

Figure 7-7 Benzene imaging with a rest atom imaging tip (a) normal tip at -1.3V (b) rest atom tip at -1.5 V

In Figure 7-7 (a), circles identify occupied adatom binding sites and an arrow points to an adatom. In Figure 7-7 (b), circles identify dimmed rest atoms and an arrow points to the particular dimmed rest atom adjacent to the bright feature in Figure 7-7 (a). The dimmed rest atom is adjacent the adatom brightening feature. This is compelling evidence that the benzene molecule is binding to the rest atom nearest the bright feature in topography. These results are consistent with chlorobenzene results from Sloan and Palmer [17] assuming the two molecules bind in the same manner. To our knowledge, this is the first solid evidence that i) the rest atom is involved in the binding of benzene to the Si(111)7x7 surface, and ii) the CeF type I configuration binds near the brightened adatom in the unit cell.

In addition to the undetermined binding sites, there is a remarkable transfer of charge between neighboring unit cells where the benzene adsorbs. This too, has been confirmed for

chlorobenzene by Sloan and Palmer [17]. They believe this charge transfer is either caused by charge transfer between the unit cells induced by the C-Cl bond dipole moment, or, more likely by the strain of the di-σ bonded molecule on the Si(111)7x7 surface. The strain would cause the physical height of atoms to change on the surface, causing darkening in topographic imaging and is the most likely explanation.

An additional explanation is proposed for the observed brightening and dimming of nearby adatoms at occupied states. For clean silicon, the charge transfer is towards the rest atom sites resulting in a fully filled rest atom dangling bond i.e. two electrons. This charge comes mainly from the adjacent adatoms. In order for the benzene molecule to form a σ bond to the rest atom, one of the electrons from the rest atom dangling bond must exit. It is natural to assume that most of this charge will transfer to the two nearest adatom dangling bonds. This would certainly cause brightening in occupied states imaging.

The dimming of the neighboring adatom sites beside the benzene molecule happens because in a clean surface, the adatom dangling bond has less than a full charge. To make the σ bond, charge is transferred to the binding adatom from the nearest neighboring adatom dangling bonds. See figure Figure 7-8.

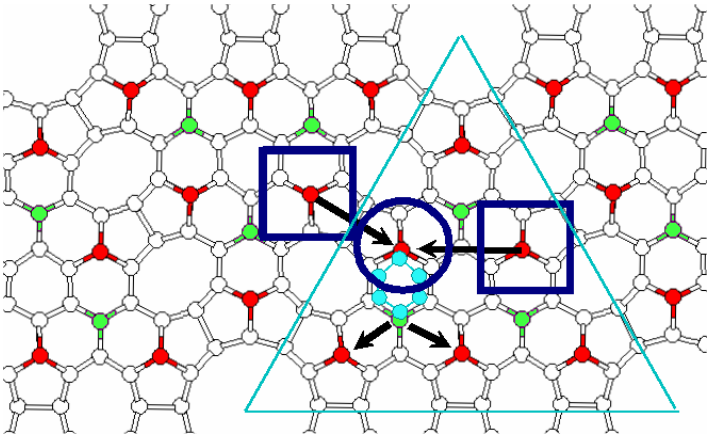

Figure 7-8 Diagram showing the proposed direction of charge transfer during the binding of benzene to Si(111)7x7 type I configuration

In Figure 7-8, the squares indicate the dimmed adatoms and the arrows show the direction of CT on the surface.

7.3 Chlorobenzene on Si(111) 7x7

Chlorobenzene (ClPh) is very similar to benzene except for one hydrogen which is replaced by a chlorine atom. The total symmetry of the molecule is reduced, but there still exists the aromatic ring from the carbon bonds. Chlorobenzene, although very similar to benzene, does behave slightly differently. The binding energy is slightly higher to the surface, 0.96 eV [84]. Also, at higher voltages such as -4 V tunneling bias, STM induced localized atomic reactions have been observed [71] in which the chlorine dissociates from the ring compound.

The ClPh molecule is believed to bind in a fashion similar to the benzene molecule, but the position of the chlorine is of some debate [35]. The 2,5-chlorocyclohexadiene-like binding structure is the most likely binding structure as suggested by HREELS and TDS experiments [91]. The location of the chlorine itself has not yet been able to be identified on the bound adsorbate through

imaging. However, a destructive STM experiment by Sloan and Palmer, which involves the dissociation of the chlorine, indicates its location when bound [32].

7.3.1 STM Images of Chlorobenzene on Si(111)7x7

STM images of ClPh on Si(111)7x7 were taken with conductance imaging (Figure 7-10). The result is that there is an observable difference in the appearance of the image compared to a clean surface. These spectroscopic images were taken at -1.5 V, which will not image the rest atom states any more, but the back-bonds instead [23]. For reference, the spectroscopic image of a clean surface is shown in Figure 7-9.

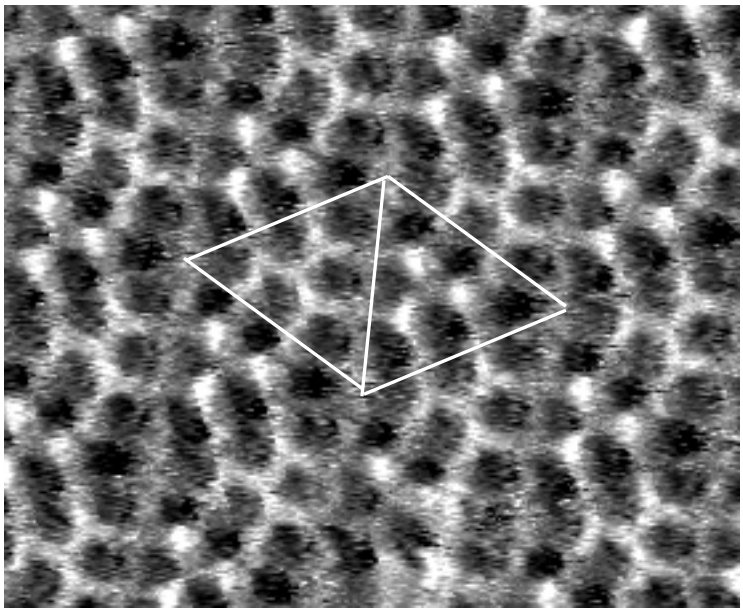

Figure 7-9 Conductance image of Si(111)7x7 at -1.5 V showing the back bonds

Figure 7-9 looks very similar to the -0.8 V image, but the shape of the bright spots is different. This is because one is imaging states with energies below the rest atom and adatom dangling bonds. The masking effect of the adatoms is still present.

In occupied states conductance images, there is a bright spot where the chlorobenzene adsorbs as shown in Figure 7-10 (b) in the lower right (unfaulted) half of the outlined unit cell.

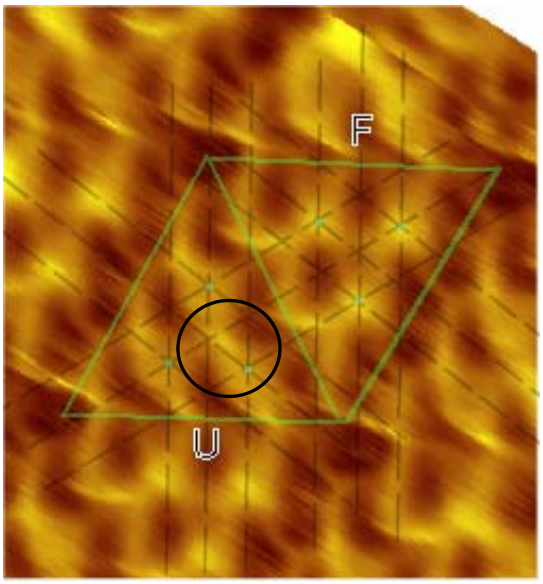

(a)

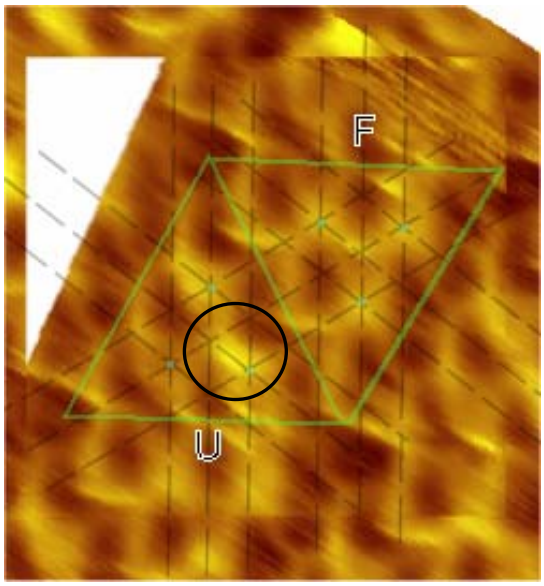

(b)

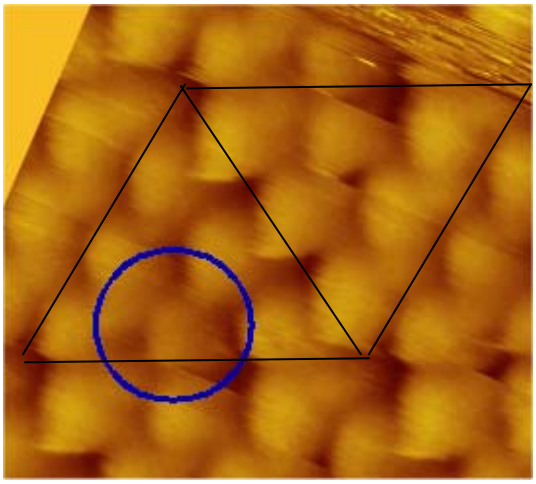

(c)

Figure 7-10 -1.5V dI/dV images of chlorobenzene on Si(111)7x7 (a) before adsorbing (b) after adsorbing (c) topography

The circle in Figure 7-10 (c) shows the adatom binding site in topography. The bright feature in the conductance image suggests a change in the LDOS in that area. It is interesting to note that the bright feature is located close to the center of the unit cell. This conductance image looks a little strange due to tip effects but the DOS features of the unit cell are still prominent.

Possible explanations for the bright spot are: i) the ClPh binding changes the charge distribution on the surface through charge transfer causing variations in the LDOS, ii) the binding of the ClPh strains the rest atom back-bond causing it to light up, iii) the bright feature is a double bond of the ClPh molecule, or iv) this is a tip effect and the location of the bright spot is misinterpreted.

Case iv) can be ruled out by observing that the clean unit cells in the image do not have this same bright feature. Case iii) is also unlikely because the double bond should not appear at this energy. The most likely explanation is that the back-bond is strained and that masking from the adatoms (and possibly rest atoms) causes the bright feature to appear differently.

Chapter 8
Summary, Conclusions, and Future Work

8.1 Summary and Conclusion

To study the binding structure of molecules on surfaces in an effort to better understand the nature of physics at the nano scale, many tools are needed. STM is an incredibly useful tool for investigating the nature of individual molecules; however, it is the supplementary capabilities of STM that make it truly powerful. In addition to studying surfaces from a topographic approach, the electronic structure can be studied.

To utilize the capabilities of STM as a tool to study adsorbates on surfaces with the goal of manipulation, an STM head was constructed that is capable of quiet operation at the University of Lethbridge with low drift. The microscope head was carefully designed and analysis shows that it functions as predicted. The coarse approach mechanism, vibrations characteristics, and thermal compensation all have excellent performance.

The STM head has very high resolution and low noise which justifies the construction of the new head. The new head is capable of thermal drift rates at room temperature of 0.5Å/minute, a notable achievement. The noise in the STM images depends on tip quality, but is capable of RMS noise less than 0.8 pm. FFT analysis of the head shows that the resonant frequencies are very high, meaning that there will be no noise from design flaws in the head, only from attenuated external vibrations.

The new head was used to carry out definitive experiments imaging benzene and chlorobenzene adsorbates on the silicon (111)7x7 surface. In addition to topographic imaging, the new head is capable of spectroscopic conductance imaging of the surface. The conductance imaging

shows promise as a tool that works in parallel with topographic imaging to help assign or confirm the binding structure of adsorbates.

The STM results from the imaging of benzene on Si(111)7x7 are promising, showing changes in the LDOS involved in the adsorbate binding to the surface. With high precision, CT effects that are associated with the bonding were observed. Using these observations, the binding configuration of the adsorbate can be inferred. We have for the first time, shown conclusively through imaging that the rest atom is involved in the binding of benzene to Si(111)7x7. To our knowledge, this is the first true STM evidence confirming the binding to the rest atom.

With conductance imaging of ClPh, we have also shown variations in the LDOS of the rest atom back bonds.

8.2 Future Plans

Now, with the knowledge of how to create an exceptional STM head for the University of Lethbridge, the next step is to advance this capability for new experiments.

8.2.1 Langmuir Adsorption Isotherm

There are many ways to measure the binding energy of molecules onto a surface. One of those is to measure the desorption of the molecule at various temperatures using a technique such as thermal desorption spectroscopy (TDS). An alternative, less used, method is to keep a constant temperature and measure the steady state coverage of a molecule on a surface. This method is only possible if there is desorption and adsorption happening simultaneously. This is the case with benzene on Si(111)7x7 at room temperature. This is a conceivably simple experiment to do with STM.

Of course, this experiment can be done without constant adsorption, but there is an intrinsic problem with STM that makes this difficult. In this experiment, a coverage of molecules is deposited onto the surface and is continuously scanned while the molecules desorb. The problem with this experiment is that the scanning tip over the molecules contributes a small amount of additional energy that will accelerate desorption. The benefit of adsorption and desorption at the same time will minimize the error in measurement from tip induced desorption.

One of the major difficulties in this experiment is to obtain an extremely clean surface on which to make measurements. The number of defects on the surface has to be sufficiently low. A point to our advantage is that with a large statistical base of measurements the errors from defects can be minimized.

8.2.2 Low Temperature STM

With the added capabilities of low temperature operation, there is a lot of new physics to explore. With semiconductors and the adsorption of organic molecules, physisorbtion can be explored. Recently, Lu et. al. published a paper outlining the use of chlorobenzene or toluene on Si(111)7x7 as a reversible molecular switch at low temperatures [20]. Such applications are an exciting prospect for the application of STM and are directly related to the work done for this thesis.

With the capability of low temperature STM, the vibrational spectroscopy of individual molecules on surfaces can be studied [25].

8.2.3 Chlorobenzene Imaging

Chlorobenzene on Si(111)7x7 is of interest because there is still some discussion on the location of the chlorine group in the bonded structure. The problem is that the chlorine is difficult to

observe using STM. It is for this purpose that spectroscopic imaging of the electronic structure of the bonded molecule is proposed.

8.2.4 Adaptive PID Sample Temperature Control

As discussed in Chapter 5, there is an intrinsic problem to controlling the temperature of a semiconductor like silicon. The solution to this non-linearity problem is an adaptive feedback in which the parameters are changed dynamically. The response of the system could be monitored and compared to theory in real-time giving a reference for corrections to the parameters. This is called model-referenced adaptive feedback control.

8.2.5 Manipulation of the Surface Using STM

It has been shown before that STM can manipulate semiconductor surfaces [10, 72, 73, 88, 92]. As an example of this, adatoms can be displaced from their position using strong fields caused by the STM tip. In Figure 8-1, I attempted to draw a circle using the STM tip on a silicon surface.

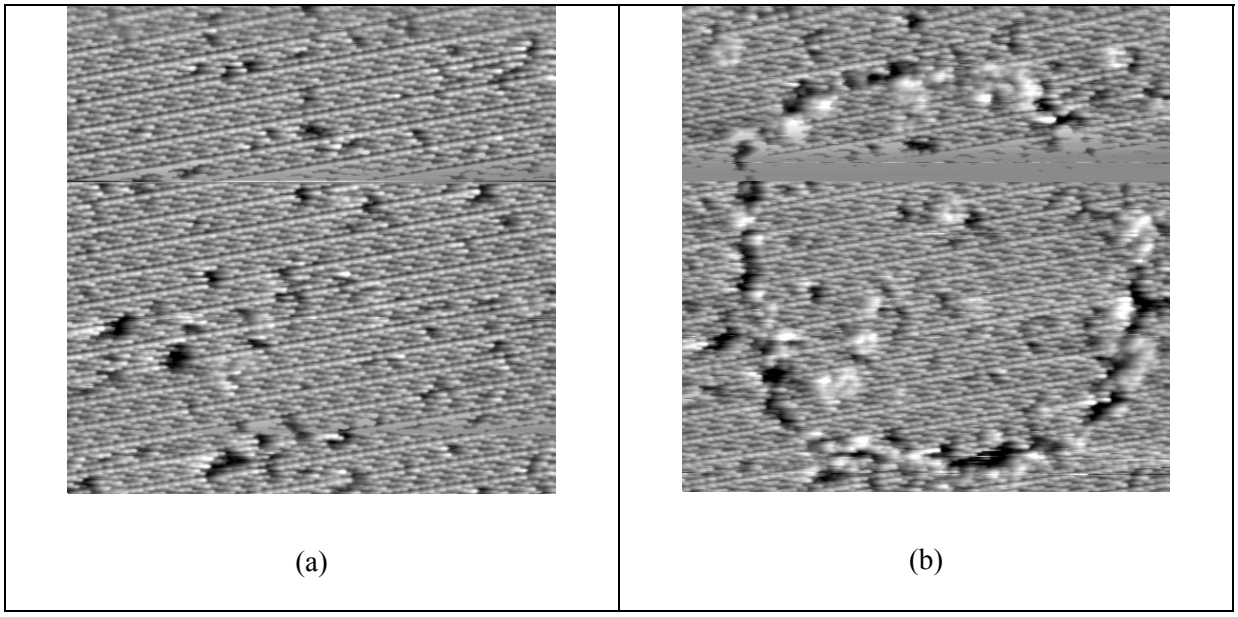

Figure 8-1 STM topograph of a Si(111)7x7 surface (a) before drawing (b) after drawing

The effect was that silicon atoms on the surface were displaced into the white blobs that are seen in Figure 8-1 (b). The diameter of the circle is 380Å or 38 nm. The most recent developments in integrated circuit technology are using interconnects as small as 50nm and are pushing down to 22nm.

Appendix A
NEXAFS of Toluene on Si(111) 7x7

Toluene is an aromatic molecule like benzene, one of the hydrogen's is replaced with a methyl group. The toluene molecule binds to the Si(111)7x7 in the same way as benzene, leaving two π bonds. Near Edge X-Ray Absorption Fine Structure measurements were done on Si(111)7x7 at BL8 at the Stanford Synchrotron Radiation Laboratory.

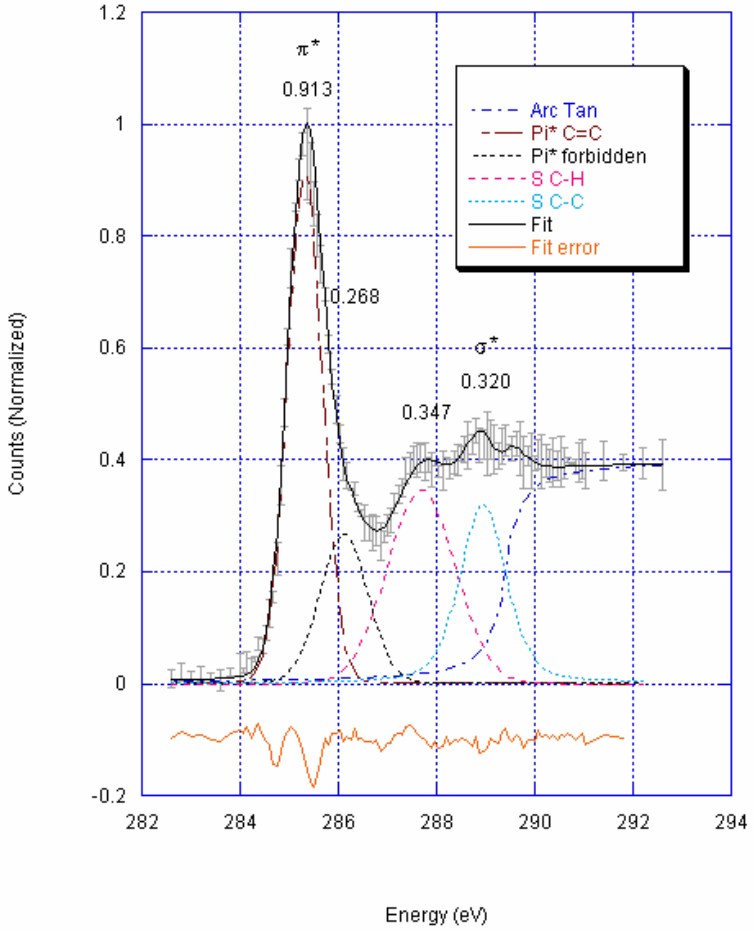

Figure A-1 NEXAFS fit of toluene on Si(111)7x7 data at 20°

The data in Figure A-1 shows the position of peaks in the NEXAFS data and the assignment of the important peaks. The height of the π^* peak with respect to angle indicates the orientation of the molecule on the surface. The π^* is from the two double bonds after adsorption. The height of the π^* peak changes at various angles showing that the molecule is highly oriented parallel to the surface.

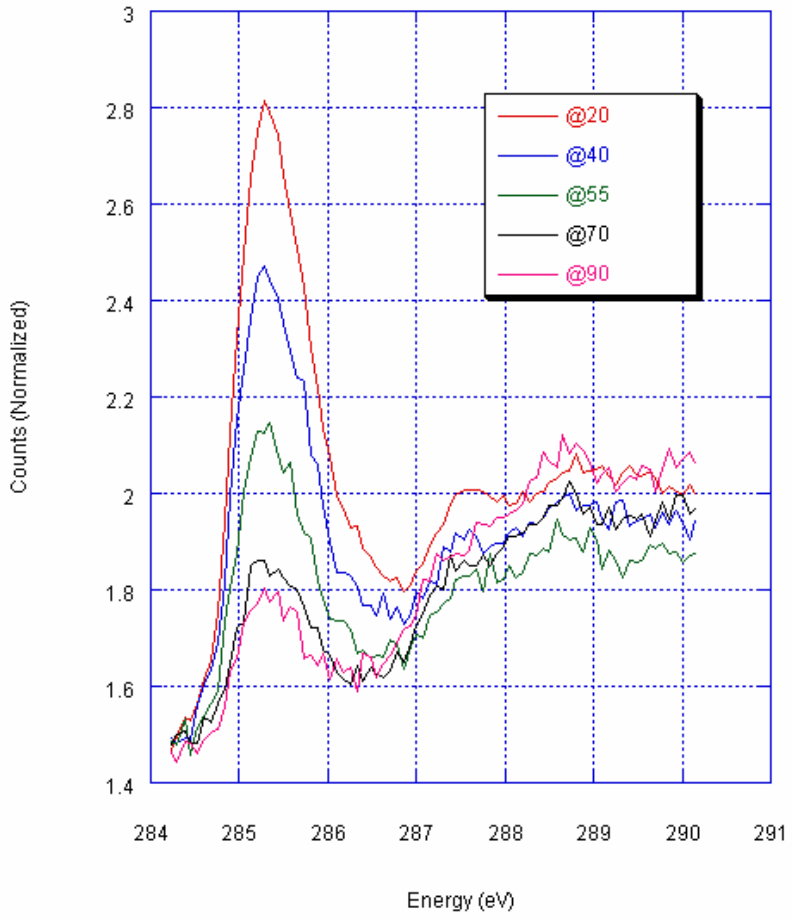

Figure A-2 NEXAFS of toluene on Si(111)7x7 at varying angles

At different angles, the π^* peak changes height showing that the molecule is lying very flat on the surface as expected. The actual angle can be approximately calculated to within estimated 5° accuracy [93]. For this molecule, an angle of roughly 27° is measured.

Appendix B
Solving the PID Equations

Before the actual PID equations can be used, one must understand the transient response of a thermal system.

Method 1: solution by separation of variables in t-space. By rearranging equation (5-12):

$$R \cdot C \frac{dT}{dt} = R \cdot P_{in} + T_0 - T , \qquad \text{(B-1)}$$

then placing all variables of T on left, t on right, one gets

$$R \cdot C \frac{dT}{R \cdot P_{in} + T_0 - T} = dt . \qquad \text{(B-2)}$$

Now, integrating both sides:

$$R \cdot C \cdot \ln\left(R \cdot P_{in} + T_0 - T\right) = t + t_0 . \qquad \text{(B-3)}$$

Note the introduction of a constant of integration. Solving this equation for *T* gives:

$$T(t) = e^{\frac{-Const}{RC}} \cdot e^{\frac{-t}{RC}} + T_0 + R \cdot P_{in} \qquad \text{(B-4)}$$

An initial condition is required to obtain the value of the constant of integration.

Method 2: solution by Laplace transform in s-space. An analysis done in s-space, by taking the Laplace transform of the differential equation (B-1), handles the initial conditions much easier. A solution is obtained by solving for *T* in s-space and returning to t-space through an inverse transform. Define the Laplace transform of a function $f(t)$ for $t \geq 0$ as

$$L\{f(t), s\} = \int_0^\infty e^{-st} f(t) dt \qquad \text{(B-5)}$$

The inverse Laplace transform is defined as

$$L^{-1}\{F(s),t\} = \int_{\gamma-i\infty}^{\gamma+i\infty} e^{st} F(s) ds \qquad \text{(B-6)}$$

which is a contour integral of *F(s)*. Most often, (B-6) does not need to be applied and a table of Laplace transforms is used to perform the inverse transform. This transform can be used to transform linear ordinary differential equations to an algebraic problem which can easily be solved. An inverse transform is then performed to return to the original variable space.

Starting with the differential equation describing the system (B-1) and then taking the Laplace transform of *t* on both sides of the equation, one does the following:

$$L\left\{\frac{dT}{dt}\right\}(s) = L\left\{\frac{P_{in}}{C} - \frac{T - T_0}{R \cdot C}\right\}(s). \qquad \text{(B-7)}$$

The result is

$$s \cdot \widetilde{T} - T(0) = \frac{P_{in}}{s \cdot C} - \frac{\widetilde{T}}{R \cdot C} + \frac{T_0}{s \cdot R \cdot C}, \qquad \text{(B-8)}$$

where $\widetilde{T}$ is the transformed variable $L\{T(t),s\} = \widetilde{T}(s)$. Solving for $\widetilde{T}$:

$$\widetilde{T} = \frac{\frac{P_{in}}{C} + \frac{T_0}{R \cdot C} + s \cdot T(0)}{s \cdot \left(s + \frac{1}{R \cdot C}\right)} \qquad \text{(B-9)}$$

which can be factored into:

$$\widetilde{T} = \frac{R \cdot P_{in} + T_0}{s} + \frac{T(0) - R \cdot P_{in} - T_0}{s + \frac{1}{RC}} \qquad \text{(B-10)}$$

taking the inverse transform gives the result

$$T(t) = R \cdot P_{in} + T_0 + \left(T(0) - R \cdot P_{in} - T_0\right) \cdot e^{\frac{-t}{RC}} \qquad \text{(B-11)}$$

The amount of error in the system e(t) is equal to the difference between where the state is and where one wants it to be:

$$e = T - T_s \qquad \text{(B-12)}$$

(B-12) is the input to (5-3), and the power to apply to the system is the output. Analysis of the PID performance will be done by letting T_s be equal to the step function at $t = 0$ starting at T_{s0} and going to T_{s1}. Taking a derivative of (5-3):

$$\frac{dP_{in}}{dt} = K_p \cdot \frac{de}{dt} + K_i \cdot e + K_d \cdot \frac{d^2 e}{dt^2} \qquad \text{(B-13)}$$

This is the equation that is used in discrete form to control the temperature of the sample in the control software. When one combines (B-12) with the derivative of (5-3), the new equation describing our system becomes

$$\frac{d^2 e(t)}{dt^2} + \frac{d^2 T_s}{dt^2} = \frac{1}{C} \cdot \left(K_p \frac{de(t)}{dt} + K_i \cdot e(t) + K_d \cdot \frac{d^2 e(t)}{dt^2} \right) - \frac{\frac{de(t)}{dt} + \frac{dT_s(t)}{dt}}{RC} \qquad \text{(B-14)}$$

The input function is

$$T_s(t) = (T_{s1} - T_{s0}) U(t - t_1) + T_{s0} \qquad \text{(B-15)}$$

where U is the Heaviside step function and t_1 is chosen to be 0. We proceed by transforming into s-space for ease of calculation. Taking the Laplace transform of both sides gives:

$$\begin{aligned} & s^2 \cdot E(s) - s \cdot e(0) - e'(0) + s \cdot (T_{s1} - T_{s0}) = \\ & \frac{1}{C} \cdot \left(K_p \cdot (s \cdot E(s) - e(0)) + K_i \cdot E(s) + K_d \left(s^2 \cdot E(s) - s \cdot e(0) - e'(0) \right) \right) \\ & - \frac{s \cdot E(s) - e(0) + T_{s1} - T_{s0}}{RC} \end{aligned} \qquad \text{(B-16)}$$

In the case of a step function, one takes $e(0) = 0$ and $e'(0) = 0$ because one is taking the system as static before the step function and holding at T_{s0}. Solving the above equation for $E(s)$ gives:

$$E(s) = \frac{s \cdot R \cdot C \cdot \left(T_{s1} - T_{s0}\right) + \left(T_{s1} - T_{s0}\right)}{s^2\left(K_d \cdot R - R \cdot C\right) + s\left(K_p \cdot R - 1\right) + K_i \cdot R} \qquad \text{(B-17)}$$

which is interesting because there is no longer a dependence on the ambient temperature for the behavior of the system. Next, one needs to do an inverse transform to return to t-space. One defines the following constants:

$$\begin{aligned} \tau &= R \cdot C \\ \kappa_p &= K_p \cdot R \\ \kappa_i &= K_i \cdot R^2 \cdot C \\ \kappa_d &= \frac{K_d}{C} \end{aligned} \qquad \text{(B-18)}$$

Where τ is the system time constant (seconds) and $\kappa_p, \kappa_i, \kappa_d$ are dimensionless. Now, equation (B-17) can be written as

$$E(s) = \tau \frac{s \cdot \tau + 1}{s^2 \cdot \tau^2 \cdot \left(\kappa_d - 1\right) + s \cdot \tau \cdot \left(\kappa_p - 1\right) + \kappa_i} \qquad \text{(B-19)}$$

In order to perform the inverse transform, a factorization is performed:

$$E(s) = \frac{c_+}{s - s_+} - \frac{c_-}{s - s_-} \qquad \text{(B-20)}$$

There are two roots s_+ & s_- they are

$$s_\pm = \left(\frac{1 - \kappa_p}{2 \cdot \tau \cdot \left(1 - \kappa_d\right)}\right) \cdot \left\{-1 \pm \sqrt{1 + \frac{4 \cdot \kappa_i \cdot \left(1 - \kappa_d\right)}{\left(1 - \kappa_p\right)^2}}\right\} \qquad \text{(B-21)}$$

Note that one of the roots is zero if there is zero integral feedback. From this, the Q value is then defined as:

$$Q^2 = \frac{-\kappa_i \cdot \left(1 - \kappa_d\right)}{\left(1 - \kappa_p\right)^2}. \qquad \text{(B-22)}$$

Bibliography

1. Binnig, G., et al., *Surface Studies by Scanning Tunneling Microscopy.* Physical Review Letters, 1982. **49**(1): p. 57-61.
2. Muller, E.W., *Resolution of the Atomic Structure of a Metal Surface by the Field Ion Microscope.* Journal of Applied Physics, 1956. **27**(5): p. 474-476.
3. Binnig, G., et al., *Tunneling through a Controllable Vacuum Gap.* Applied Physics Letters, 1982. **40**(2): p. 178-180.
4. Chen, C.J., *Introduction to Scanning Tunneling Microscopy*. Optical and Imaging Sciences, ed. M. Lapp, et al. 1993, New York: Oxford University Press.
5. Schlier, R.E. and H.E. Farnsworth, *Structure and Adsorption Characteristics of Clean Surfaces of Germanium and Silicon.* Journal of Chemical Physics, 1959. **30**(4): p. 917-926.
6. Takayanagi, K., et al., *Structure-Analysis of Si(111)-7x7 Reconstructed Surface by Transmission Electron-Diffraction.* Surface Science, 1985. **164**(2-3): p. 367-392.
7. Takayanagi, K., et al., *Structural-Analysis of Si(111)-7x7 by Uhv-Transmission Electron-Diffraction and Microscopy.* Journal of Vacuum Science & Technology a-Vacuum Surfaces and Films, 1985. **3**(3): p. 1502-1506.
8. Joyce, B.A., *Some Aspects of Surface Behavior of Silicon.* Surface Science, 1973. **35**(1): p. 1-7.
9. Abraham, D.W., et al., *Surface modification with the scanning tunneling microscope.* IBM J. Res. Develop., 1986. **30**(5): p. 492-499.
10. Lyo, I.W. and P. Avouris, *Field-Induced Nanometer-Scale to Atomic-Scale Manipulation of Silicon Surfaces with the Stm.* Science, 1991. **253**(5016): p. 173-176.
11. Bouju, X., C. Joachim, and C. Girard, *Single-atom motion during a lateral STM manipulation.* Physical Review B, 1999. **59**(12): p. 7845-7848.
12. Meyer, G., et al., *Controlled Manipulation of Atoms and Small Molecules with a Low Temperature Scanning Tunneling Microscope.* Single Mol., 2000. **1**(1): p. 79-86.
13. Bennewitz, R., et al., *Atomic scale memory at a silicon surface.* Nanotechnology, 2002. **13**: p. 499-502.
14. Alavi, S., et al., *Inducing desorption of organic molecules with a scanning tunneling microscope: Theory and experiments.* Physical Review Letters, 2000. **85**(25): p. 5372-5375.
15. Patitsas, S.N., et al., *Current-Induced Organic Molecule-Silicon Bond Breaking: Consequences for Molecular Devices.* Surface Science Letters, 2000. **457**: p. L425-L431.
16. Kawasaki, T., et al., *Adsorption and desorption of benzene on Si(111)-7 X 7 studied by scanning tunnelling microscopy.* Surface and Interface Analysis, 2001. **31**(2): p. 126-130.
17. Sloan, P.A. and R.E. Palmer, *Manipulation of polyatomic molecules with the scanning tunnelling microscope at room temperature: chlorobenzene adsorption and desorption from Si(111)-(7x7).* Journal of Physics-Condensed Matter, 2006. **18**(33): p. S1873-S1885.
18. Dujardin, G., R.E. Walkup, and P. Avouris, *Dissociation of Individual Molecules with Electrons from the Tip of a Scanning Tunneling Microscope.* Science, 1992. **255**(5049): p. 1232-1235.
19. Himpsel, F.J., et al., *Self-assembly of one-dimensional nanostructures at silicon surfaces.* Solid State Communications, 2001. **117**(3): p. 149-157.
20. Lu, X.K., J.C. Polanyi, and J. Yang, *A reversible molecular switch based on pattern-change in chlorobenzene and toluene on a Si(111)-(7 x 7) surface.* Nano Letters, 2006. **6**(4): p. 809-814.

21. Piva, P.G., et al., *Field regulation of single-molecule conductivity by a charged surface atom.* Nature, 2005. **435**: p. 658-661.
22. Feenstra, R.M., J.A. Stroscio, and A.P. Fein, *Tunneling Spectroscopy of the Si(111)2x1 Surface.* Surface Science, 1986. **181**: p. 295-306.
23. Hamers, R.J., R.M. Tromp, and J.E. Demuth, *Surface Electronic-Structure of Si(111)-(7 X 7) Resolved in Real Space.* Physical Review Letters, 1986. **56**(18): p. 1972-1975.
24. Hamers, R.J., R.M. Tromp, and J.E. Demuth, *Electronic and Geometric Structure of Si(111)-(7x7) and Si(001) Surfaces.* Surface Science, 1987. **181**(1-2): p. 346-355.
25. Stipe, B.C., M.A. Rezaei, and W. Ho, *A variable-temperature scanning tunneling microscope capable of single-molecule vibrational spectroscopy.* Review of Scientific Instruments, 1999. **70**(1): p. 137-143.
26. Lauhon, L.J. and W. Ho, *Effects of temperature and other experimental variables on single molecule vibrational spectroscopy with the scanning tunneling microscope.* Review of Scientific Instruments, 2001. **72**(1): p. 216-223.
27. Stipe, B.C., M.A. Rezaei, and W. Ho, *Single-molecule vibrational spectroscopy and microscopy.* Science, 1998. **280**(5370): p. 1732-1735.
28. Ho, W., *Single-molecule chemistry.* Journal of Chemical Physics, 2002. **117**(24): p. 11033-11061.
29. Wolkow, R.A. and D.J. Moffatt, *The frustrated motion of benzene on the surface of Si(111).* Journal of Chemical Physics, 1995. **103**(24): p. 10696-10700.
30. Taguchi, Y., M. Fujisawa, and M. Nishijima, *Adsorbed State of Benzene on the Si(111)(7x7) Surface.* Chemical Physics Letters, 1991. **178**(4): p. 363-368.
31. Carbone, M., et al., *A low symmetry adsorption state of benzene on Si(111)7x7 studied by photoemission and photodesorption.* Surface Science, 1998. **407**(1-3): p. 275-281.
32. Sloan, P.A. and R.E. Palmer, *Two-electron dissociation of single molecules by atomic manipulation at room temperature.* Nature, 2005. **434**(7031): p. 367-371.
33. Sloan, P.A. and R.E. Palmer, *Tip-state control of rates and branching ratios in atomic manipulation.* Nano Letters, 2005. **5**(5): p. 835-839.
34. Becker, R.S., et al., *Real-Space Observation of Surface-States on Si(111)7x7 with the Tunneling Microscope.* Physical Review Letters, 1985. **55**(19): p. 2032-2034.
35. Li, Y.C., et al., *Theoretical study of the chemisorption of benzene on Si(111)-7x7 surface.* Acta Chimica Sinica, 2002. **60**(4): p. 653-659.
36. Petsalakis, I.D., J.C. Polanyi, and G. Theodorakopoulos, *Theoretical study of the induced attachment of benzene to Si(111) 7 x 7.* Surface Science, 2003. **544**(2-3): p. 162-169.
37. Petsalakis, I.D., J.C. Polanyi, and G. Theodorakopoulos, *Theoretical study of benzene, toluene, and dibromobenzene at a Si(111)7x7 surface.* Israel Journal of Chemistry, 2005. **45**(1-2): p. 111-126.
38. Tomimoto, H., et al., *Study of adsorption structure of benzene and toluene on Si(111)7x7 surfaces.* Surface Science, 2004. **566**: p. 664-670.
39. Tomimoto, H., et al., *Study of benzene and toluene on Si(111)7 x 7 surface by scanning tunneling microscopy.* Surface Science, 2003. **526**(3): p. 341-350.
40. Liu, W., *Scanning Tunneling Microscopy and Spectroscopy Simulations of the Silicon (111) - (7x7) Surface*, in *Physics*. 2006, University of Lethbridge: Lethbridge, Alberta, Canada.
41. Ju, L., D.G. Blair, and C. Zhao, *Detection of gravitational waves.* Rep. Prog. Phys, 2000. **63**: p. 1317-1427.
42. Besocke, K., *An Easily Operable Scanning Tunneling Microscope.* Surface Science, 1987. **181**(1-2): p. 145-153.

43. Binnig, G. and D.P.E. Smith, *Single-Tube 3-Dimensional Scanner for Scanning Tunneling Microscopy.* Review of Scientific Instruments, 1986. **57**(8): p. 1688-1689.
44. Chen, C.J., *Insitu Testing and Calibration of Tube Piezoelectric Scanners.* Ultramicroscopy, 1992. **42**: p. 1653-1658.
45. *Micropositioning, Nanopositioning, Nano Automation Catalogue*. 2001, PI (Physik Instrumente) GmbH. p. 4-42.
46. Chen, C.J., *Electromechanical Deflections of Piezoelectric Tubes with Quartered Electrodes.* Applied Physics Letters, 1992. **60**(1): p. 132-134.
47. Kinsler, L.E., et al., *Fundamentals Of Acoustics*. Third ed. 1982: John Wiley & Sons.
48. EBL Products Inc. 91 Prestige Park Circle, E.H., CT, USA www.eblproducts.com.
49. Wiretronic Inc. Pine Grove, C., USA. www.wiretron.com.
50. EPOXY Technology, F.D., Billerica, MA, USA, www.epotek.com.
51. MDC Vacuum Products Inc. 23842 Cabot Boulevard, H., CA, USA www.mdc-vacuum.com.
52. Stroscio, J.A. and W.J. Kaiser, *Scanning Tunneling Microscopy*. Vol. 27. 1993: Academic Press, INC.
53. French, A.P., *Vibrations and Waves*. The M.I.T. Introductory Physics Series. 1971, New York, NY: W. W. Norton & Company, Inc.
54. Oliva, A.I., M. Anguilar, and V. Sosa, *Low and high frequency vibration isolation for scanning probe microscopy.* Meas. Sci. Technol., 1998. **9**: p. 383-390.
55. Minus K Technology Inc. 420 S. Hindry Ave, U.E., Inglewood, CA, USA www.minusk.com.
56. RHK Technology, E.M.R., Troy, MI, USA www.rhk-tech.com.
57. Roth, A., *Vacuum Technology*. Third, updated and enlarged edition ed. 1990, Amsterdam: Elsevier Science B.V.
58. Strausser, Y.E. *The effect of surface treatment on the outgassing rates of 304 stainless steel*. in *Fourth international vacuum congress*. 1968. Manchester, UK: Institute of Physics and Physical Society.
59. Mikron Infrared Inc. 16 Thorton Road, O., New Jersey, USA www.mikroninfrared.com.
60. Smith, J.N. and W.L. Fite, *Reflection and Dissociation of H2 on Tungsten.* Journal of Chemical Physics, 1962. **37**(4): p. 898-&.
61. Reif, F., *Fundamentals of Statistical and Thermal Physics*. 1965: McGraw-Hill, Inc.
62. Schroeder, D.V., *An Introduction to Thermal Physics*. 2000: Addison Wesley Longman.
63. Kern, W. and D.A. Puotien, *Cleaning Solutions Based on Hydrogen Peroxide for use in Silicon Semiconductor Technology.* RCA Review, 1970(31): p. 187-206.
64. Miyake, K., et al., *Stability and nuclear formation of Si(111)-7 x 7 structure as determined from charge redistribution in surface layers.* Surface Science, 1999. **429**(1-3): p. 260-273.
65. Shimada, W., et al., *Transformations of faulted halves of the DAS structure on quenched Si(111).* Surface Science, 1999. **423**(2-3): p. L291-L298.
66. White, G.K. and P.J. Meeson, *Experimental Techniques in Low-Temperature Physics*. 2002, Oxford: Clarendon Press.
67. Lim, H., et al., *Ab initio study of hydrogen adsorption on the Si(111)-(7x7) surface (vol 52, pg 17231, 1995).* Physical Review B, 1996. **54**(7): p. 5179-5179.
68. Kubby, J.A. and J.J. Boland, *Scanning tunneling microscopy of semiconductor surfaces.* Surface Science Reports, 1996. **26**(3-6): p. 61-204.
69. Jurczyszyn, L., N. Mingo, and F. Flores, *Influence of the atomic and electronic structure of the tip on STM images and STS spectra.* Surface Science, 1998. **404**(1-3): p. 459-463.
70. Tersoff, J. and D.R. Hamann, *Theory of the Scanning Tunneling Microscope.* Physical Review B, 1985. **31**(2): p. 805-813.

71. Lu, P.H., J.C. Polanyi, and D. Rogers, *Electron-induced "localized atomic reaction" (LAR): Chlorobenzene adsorbed on Si(111) 7x7.* Journal of Chemical Physics, 1999. **111**(22): p. 9905-9907.
72. Sloan, P.A., et al., *Mechanisms of molecular manipulation with the scanning tunneling microscope at room temperature: Chlorobenzene/Si(111)-(7x7).* Physical Review Letters, 2003. **91**(11).
73. Stipe, B.C., M.A. Rezaei, and W. Ho, *Site-specific displacement of Si adatoms on Si(111)-(7x7).* Physical Review Letters, 1997. **79**(22): p. 4397-4400.
74. Avouris, P. and R. Wolkow, *Atom-Resolved Surface-Chemistry Studied by Scanning Tunneling Microscopy and Spectroscopy.* Physical Review B, 1989. **39**(8): p. 5091-5100.
75. Brommer, K.D., et al., *Theory of Adsorption of Atoms and Molecules on Si(111)-(7x7).* Surface Science, 1994. **314**(1): p. 57-70.
76. Brommer, K.D., et al., *Modeling Large Surface Reconstructions on the Connection Machine.* Japanese Journal of Applied Physics Part 1-Regular Papers Short Notes & Review Papers, 1993. **32**(3B): p. 1360-1367.
77. Wolkow, R. and P. Avouris, *Atom-Resolved Surface-Chemistry Using Scanning Tunneling Microscopy.* Physical Review Letters, 1988. **60**(11): p. 1049-1052.
78. Zhang, Z., M.A. Kulakov, and B. Bullemer, *Charge transfer and rest-atom imaging in dimer-adatom-stacking-fault structure evolution observed by scanning tunnelling microscopy on the Si(111) surface.* Surface Science, 1997. **375**(2-3): p. 195-202.
79. Qian, G.X. and D.J. Chadi, *Si(111)-7x7 Surface - Energy-Minimization Calculation for the Dimer Adatom Stacking-Fault Model.* Physical Review B, 1987. **35**(3): p. 1288-1993.
80. Brown, W.H., *Organic Chemistry*. 1995: Harcourt Brace College Publishers.
81. He, Z.H. and K.T. Leung, *Room-temperature chemisorption and thermal evolution of perchloroethylene and trichloroethylene on Si(111)7x7: Formation of chlorinated vinylene and vinylidene and acetylide adspecies, and thermal etching reactions.* Surface Science, 2005. **583**(2-3): p. 179-190.
82. Maraghechi, P., S.A. Horn, and S.N. Patitsas, *Site selective atomic chlorine adsorption on the Si(111)7x7 surface.* Surface Science, 2006(In Press).
83. Brown, D.E., D.J. Moffatt, and R.A. Wolkow, *Isolation of an intrinsic precursor to molecular chemisorption.* Science, 1998. **279**(5350): p. 542-544.
84. Jiang, G.P., J.C. Polanyi, and D. Rogers, *Electron and photon irradiation of benzene and chlorobenzene on Si(111) 7 x 7.* Surface Science, 2003. **544**(2-3): p. 147-161.
85. Hofer, W.A., et al., *Benzene on silicon: combining STM experiments with first principles studies.* Surface Science, 2001. **482**: p. 1181-1185.
86. Li, Z.H., et al., *A density functional theory study on the adsorption of chlorobenzene on the Si(111)-7x7 surface.* Journal of Physical Chemistry B, 2004. **108**(37): p. 14049-14055.
87. Macpherson, C.D., D.Q. Hu, and K.T. Leung, *Room-Temperature Adsorption of Benzene on Si(111)7x7 by Thermal-Desorption Spectrometry.* Solid State Communications, 1991. **80**(3): p. 217-220.
88. Alavi, S., R. Rousseau, and T. Seideman, *Toward control of surface reactions with a scanning tunneling microscope. Structure and dynamics of benzene desorption from a silicon surface.* Journal of Chemical Physics, 2000. **113**(10): p. 4412-4423.
89. Wang, Z.H., Y. Cao, and G.Q. Xu, *The binding of benzene on Si(111)-(7 x 7): a theoretical modelling approach.* Chemical Physics Letters, 2001. **338**(1): p. 7-13.
90. Bulavenko, S.Y., P.V. Melnik, and M.G. Nakhodkin, *Scanning tunneling microscopy images of the atoms in the corner holes on the Si(111)-(7 x 7) surface with bismuth-covered tips.* Surface Science, 2000. **469**(2-3): p. 127-132.

91. Cao, Y., J.F. Deng, and G.Q. Xu, *Stereo-selective binding of chlorobenzene on Si(111)-7x7.* Journal of Chemical Physics, 2000. **112**(10): p. 4759-4767.
92. Alavi, S., et al., *Controlling organic reactions on silicon surfaces with a scanning tunneling microscope: Theoretical and experimental studies of resonance-mediated desorption.* Faraday Discussions, 2000(117): p. 213-229.
93. Willey, T.M., *Characterization of Functinalized Self-Assembled Monolayers and Surface-Attached Interlocking Molecules Using Near-Edge X-ray Absorption Fine Structure Spectroscopy*, in *Physics*. 2004, University of California, Davis: Davis, California. p. 27 of 155.